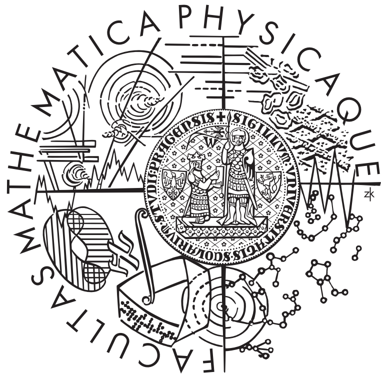

FACULTY
OF MATHEMATICS
AND PHYSICS
Charles University

DOCTORAL THESIS

Lukáš Šedivý

Structural defects in II-VI semiconductors

Institute of Physics of Charles University

Supervisor of the doctoral thesis: Doc. Ing. Eduard Belas, CSc.
Study programme: Physics
Study branch: Quantum optics and Optoelectronics

Prague 2022

I declare that I carried out this doctoral thesis independently, and only with the cited sources, literature and other professional sources. It has not been used to obtain another or the same degree.

I understand that my work relates to the rights and obligations under the Act No. 121/2000 Sb., the Copyright Act, as amended, in particular the fact that the Charles University has the right to conclude a license agreement on the use of this work as a school work pursuant to Section 60 subsection 1 of the Copyright Act.

In .... date ....

Author's signature

At this place, I would like to thank the following people, without whom I would not have been able to perform my research, without whom it would have been challenging to finish my doctorate studies and without whom would have been significantly less complex and of lower quality.

First, many thanks are dedicated to my supervisor, Eduard Belas, for his guidance during the whole period of my studies. I appreciate especially sharing his deep experimental experience, essential discussions on interpretation reached results, and lessons he gave me, sometimes even unintentionally, about life in general.

Besides my supervisor, I would like to acknowledge my advisor Roman Grill, who guided me thru the theoretical interpretation of experimental data and a broader physical context. He taught me what is critically important in any written scientific output and patiently corrected my formulation even when we almost heard the clock beating.

I am grateful to Jan Franc, who introduced me to the social activities in physics and built a friendly and supporting environment at the Institute of Physics.

The work would be harrowing and hardly possible without many colleagues from all the laboratories: namely, not only Pavel Moravec, Pavel Hlídek, Pavel Höschl, Jan Ulrych, Roman Šilha and Martin Veis.

I want to thank my former schoolmate, Lukáš Nádvorník, the most intelligent man from my generation, who constantly inspired me not only at physics but at ethics and philosophy as well.

For their friendship and assistance, I also thank my colleagues Jakub Zázvorka and Jakub Pekárek and Václav Dědič.

I valued finishing my scientific work as natural consequence of my life path; therefore, besides everyone mentioned above, I do not want to omit being grateful my faculty and high school teachers.

I am grateful to my ex-girlfriend, Anička Čámská, who broke up with me in the summer of 2019 and I converted the then destructive energy to writing the main part of this thesis. Many thanks to her that we bacome friends afterwards and now she emotionally supports me during tight thesis finishing.

Thanks are dedicated to my second ex-girlfriend, Jít'a Ludvíková, who taught me about the value of people's emotions. She encouraged me to figure out who I am, to find my strengths and challenge my demos, which were crucial obstacles on my way to finishing this thesis.

Thanks to my close friends, mainly from high school and scouts world, who unconditionally share with me the pleasant and harsh sides of life and make it bearable.

Many thanks to Klárka Spáčilová, who patiently read this thesis and corrected any grammar and who is going to be rewarded by super tasty diner.

Finally, I am deeply grateful to my family, who supported me during my whole school period. They motivated me when I was down and suffered my enthusiasm when the experiment was working.

Title: Structural defects in II-VI semiconductors

Author: Lukáš Šedivý

Department: Institute of Physics of Charles University

Supervisor: Doc. Ing. Eduard Belas, CSc., Institute of Physics, Faculty of Mathematics and Physics, Charles University

Abstract: The single crystalline $CdTe$ doped by chlorine is an excellent material for manufacturing x-ray and gamma-ray room-temperature semiconductor detectors thanks to the large linear attenuation coefficient, the possibility to make it high-resistive at the room temperature, and good electron mobility and the lifetime. This thesis aimed to examine the effect of annealing in well-defined ambient component pressure, Cd or Te, on the crystal's defect structure. The first experimental is devoted to eliminating the second phase defects - inclusions - present in $CdTe:Cl$, which significantly decay the crystal quality and detection performance. The following experimental parts are focused on the detailed investigation of the point defect structure of $CdTe:Cl$. The annealing interval bisection method for reaching high resistivity material is introduced. The equilibrium defect structure is investigated using the *in-situ* high-temperature Hall effect measurements. The results are interpreted through an advanced model of the defect structure considering also dissociation of neutral defect complex affecting the defect self-compensation. Two independent experimental methods, *in-situ* high temperature Hall effect measurements and Positron annihilation spectroscopy, prove the existence of this neutral defect. The dynamic of point defect structure and the chemical diffusion coefficient are studied measuring the temporal evolution of the conductivity after the step-like change of Cd pressure. The validity of the classical Meyer-Neldel rule is critically discussed and its extension to a triangle-shaped Meyer-Neldel rule is introduced.

Keywords: CdTe Inclusions Point defects Annealing Defect dynamic

Název práce: Strukturní defekty v II-VI polovodičích

Autor: Lukáš Šedivý

Department: Fyzikální ústav Univerzity Karlovy

Školitel: Doc. Ing. Eduard Belas, CSc., Fyzikální ústav Univerzity Karlovy, Matematicko-fyzikální fakulta, Univerzita Karlova

Abstrakt : Chlórem dopovaný mono-krystal Teluridu kademnatého CdTe je perspektivní materiál pro výrobu nechlazených detektorů vysokoenergetického záření především pro jeho vysoký absorpční koeficient, vysoký odpor za pokojové teploty, dobrou elektron/děrovou pohyblivost a příznivý $\mu\tau$ produkt. Cílem této práce je zmapovat vliv systematického žíhání v parách Cd a Te na výslednou defektní strukturu krystalu. Přičemž první experimentální kapitola je věnována metodice odstranění inkluzí běžně přítomných v $CdTe : Cl$, které významně limitují detekční schopnosti materiálu. Následující experimentální kapitoly jsou zasvěceny výzkumu bodových defektu v $CdTe : Cl$. V práci je představena metoda půlení intervalu, která umožňuje nastolit/znovunastolit vysokoodporový stav krystalu. Vliv bodových defektu v termodynamické rovnováze na galvanomagnetické charakteristiky krystalu je studován pomocí *in-situ* měření Hallova jevu za vysokých teplot. Změřená experimentální data jsou interpretována za použití pokročilého teoretického modelu struktury bodových defektů v $CdTe$, který je obohacen o disociací elektricky neutrálního komplexu bodových defektů. Dvě nezávislé metody, *in-situ* měření Hallova jevu za vysokých teplot a pozitronová anihilační spektroskopie, experimentálně potvrdily existenci tohoto defektu. Dynamika struktury bodových defektů a koeficient chemické difuze jsou pozorován jako relaxace elektrické vodivosti vzorku po skokové změně parciálního tlaku Cd obklopujícího vzorek. Práce též diskutuje limitace standardního Meyer-Neldel pravidla a představuje jeho rozšíření na Meyer-Neldel pravidlo trojúhelníkovitého tvaru.

Klíčová slova: CdTe Inkluze Bodové defekty Žíhání Dynamika defektů

Contents

Introduction **4**

1 Introduction to CdTe and CdZnTe **7**
1.0.1 Band structure . . . 8

2 Crystal defects **9**
2.1 Introduction . . . 9
2.2 Thermodynamic theory of Cd(Zn)Te growth . . . 9
2.3 Bulk defects . . . 12
2.4 Plane defects . . . 13
2.5 Line defects . . . 13
2.6 Point defects . . . 14
2.6.1 Defects statistic . . . 16
2.6.2 Reaching of high resistivity - Defects compensation . . . 18

3 Inclusion elimination **21**
3.1 Introduction . . . 21
3.2 Experimental techniques . . . 22
3.2.1 Sample preparation . . . 22
3.2.2 Annealing . . . 22
3.2.3 Infrared microscopy . . . 23
3.2.4 Room temperature Hall effect . . . 24
3.3 Results and Discussion . . . 26
3.3.1 Samples . . . 26
3.3.2 Cd Inclusion annealing . . . 28
3.3.3 Te Inclusion annealing . . . 31
3.4 Conclusion . . . 32

4 High resistivity restoration **33**
4.1 Introduction . . . 33
4.2 Experiment . . . 33
4.2.1 Samples for resistivity restoration study . . . 34
4.3 Results and Discussion . . . 35
4.4 Conclusion . . . 39

5 *In-Situ* galvanomagnetic measurement **40**
5.1 Introduction . . . 40
5.2 Experimental technique . . . 40
5.3 Results and Discussion . . . 43
5.4 Conclusion . . . 48

6 Chemical diffusion coefficient 49
6.1 Introduction . . . 49
6.2 Experimental . . . 51
6.3 Results and Discussion . . . 51
6.3.1 Determination of Chemical diffusion coefficient . . . 51
6.3.2 Chemical diffusion coefficient simulations . . . 56
6.3.3 Discussion of Meyer-Neldel rule in CdTe : Cl . . . 57
6.4 Conclusions . . . 65

7 Positron annihilation spectroscopy 66
7.1 Introduction . . . 66
7.2 Samples . . . 66
7.3 Experimental technique . . . 67
7.3.1 Physical principles of positron annihilation spectroscopy . . . 67
7.3.2 Positron lifetime spectroscopy (LT) . . . 68
7.3.3 Coincidence Doppler broadening spectroscopy (CDB) . . . 69
7.3.4 Positron back diffusion measurement . . . 70
7.3.5 Glow Discharge Mass Spectrometry (GDMS) . . . 70
7.4 Theory . . . 72
7.5 Results and Discussion . . . 74
7.5.1 Galvanomagnetic measurements . . . 74
7.5.2 Calculated positron lifetimes . . . 75
7.5.3 Lifetime spectroscopy . . . 80
7.5.4 CDB spectroscopy . . . 91
7.6 Conclusions . . . 95

Conclusion 97

Author's publications 100

List of Figures 115

List of Tables 119

Appendices 120

A Laboratory cook book 121
A.1 Ampoule preparation . . . 121
A.2 $CdTe$ sample preparation . . . 121
A.2.1 Cutting . . . 121
A.2.2 Polishing . . . 122
A.2.3 Chemo-mechanical polishing . . . 122
A.2.4 Etching . . . 122
A.2.5 Cleaning . . . 122

A.3 Contacts preparation 122
A.3.1 Chemical solution deposition 122
A.3.2 Physical vapour deposition 123
A.4 Coating 123
A.5 Contacts welding 124

Introduction

The understanding of semiconductors begins with experiments focused on the electrical properties of materials in the early 19th century. The first observation of semiconductor properties was done by T. J. Seebeck in 1821.[1] Decrease of silver sulfide resistivity caused by heating was observed by M. Faraday in 1833.[2] In 1839, A. E. Becquerel reported observation of a photovoltaic effect[3] and W. Smith discovered photo-resistivity in 1873.[4] The rectification of semiconductors was independently described by K. F. Braun and M.A. Rosenschold.[5,6] Adams and Day observed the photovoltaic effect in selenium in 1876.[7]

In 1879 E. H. Hall discovered the Hall effect.[8] The discovery of the electron by J.J. Thomson in 1897[9] brought the electron-based conduction theory in solids. The positively charged carriers, later known as holes, were first observed in copper iodide thin films by K. Baedeker, the first scientist who developed the pointed semiconductor doping.[10] The theory of solid-state physics dates back to the 1950s. F. Bloch published a theory of the movement of electrons through atomic lattices in 1928.[11] His work was later expanded by B. Gudden, A. H. Wilson, W. H. Schottky and N. F. Mott.[6,12–14] By 1938, B. Davydov had developed a theory of the copper-oxide rectifier, identifying the effect of the p–n junction and the importance of minority carriers and surface states.[6]

A match between theoretical predictions and experimental results was sometimes poor because semiconductor properties are extremely sensitive to tiny amounts of impurities.[6] Commercially available semiconductor materials of the 1920s contained various impurities at huge concentration. Devices using semiconductors were at first constructed based on empirical knowledge before pure materials were developed, and semiconductor theory has provided a guide to the construction of more capable and reliable devices, such as transistors or photodetectors.

A huge development of materials with semiconducting properties in the early 1950s led to a wide expansion of semiconductor technology based mainly on Si and Ge. Later on, also alternative semiconducting III-V or II-VI compound materials, such as Gallium arsenide (GaAs) or Cadmium telluride (CdTe), were explored and investigated.

Nowadays, Cadmium telluride (CdTe) and Cadmium zinc telluride (CdZnTe) are important materials for multiple applications in solar cells[15–17], X-ray and gamma-ray room-temperature detectors[18,19], electro-optic modulators[20], and substrates for CdHgTe infra-red detector epitaxy[21].

In case of room-temperature, semiconductor detectors CdTe an CdZnTe overcome convention materials (Si,Ge,GaAs) by reaching and optimal conjunction of principal parameters[22]:

1. High atomic number, Z, for efficient absorption of radiation.

2. Large enough band-gap energy, $E_g > 1.5\,\mathrm{eV}$, for high resistivity ($> 1 \times 10^9\,\Omega\mathrm{cm}$) and suppression of leakage current at room temperature.

3. Small enough band-gap, $E_g < 5\,\mathrm{eV}$, resulting in the number of generated electron–hole pairs, which is reasonably large and therefore the statistical variation is small and thus ensuring higher signal-to-noise ratio.

4. Large mobility-lifetime product, $\mu\tau$, is desired to ensure that carriers generated by radiation in the whole detector volume can be collected by electrodes.

5. Homogeneous, defect-free material with acceptable cross-sectional area and thickness. For high sensitivity and efficiency, large single-crystal volumes are required to ensure that as many incident photons as possible have the opportunity to interact in the detector volume. The homogeneity requirement and low defect density ensure good charge transport properties and low leakage current.

6. Possible fabrication of chemical contacts which produce no defects, impurities or barriers to the charge collection process and that can be used effectively to apply a uniform electric field across the device.

7. Surfaces with sufficiently high electrical resistivity will ensure that noise caused by surface conduction is low.

8. On the other hand, low mobility of holes resulting in a highly suboptimal collection of positive charges represents the main disadvantage of CdTe.

The first comprehensive study of CdTe material was already published in 1959 by de Nobel[23], in which basic structural, electrical and optical properties of this material were described. Despite the high interest and expectation on CdTe/CdZnTe-detectors, they have not been widely commercialized until now due to the high costs of fabrication of high-quality crystals.

In the presented work, the reader gets acquainted with CdTe/CdZnTe crystals general properties at Chapter 1). Following Chapter 2 is dedicated to a classification of crystal defects types commonly presented at CdTe/CdZnTe, because crystal quality, important for final X-ray and gamma-ray room-temperature detectors properties, is closely connected to its defects structure.

For successful industrialization of CdTe/CdZnTe-detectors production, it is crucial to crystallize a large volume of homogeneous crystals in one batch to suppress production costs. In advance, it could be revealed that large volume crystals homogeneity is affected mainly by bulk, planar, and line defects. If present in crystals, each of these defects significantly reduces high-quality crystal production yields.

The first experimental part, Chapter 3, of this work is dedicated to experimental research of such types of defects. This chapter is focused mainly on the primary bulk defect presented in CdTe/CdZnTe, called inclusion. The successful approach to inclusion elimination by annealing at well-defined Cd- or Te-overpressure is presented in this chapter.

However, it was pointed out that overpressure annealing, introduced in Chapter 3, leads to a generation of point defects at crystal lattice. Point defect structure affects not only

the high resistivity of crystals required above but also mobility-lifetime product, $\mu\tau$ and other detection ability of CdTe/CdZnTe.

Therefore the following part, Chapter 4, of this work, presents experimental results of high resistivity restoration for CdTe doped by chlorine, $CdTe:Cl$. Post grown two-step annealing in the two-zone furnace is considered as an effective approach for point defects structure modulation. Simultaneously, based on experimental results, the connection between high resistivity state, original chlorine dopping and Te-pressure is assumed and discussed more in-depth in the same chapter.

Two-step annealing mentioned above appears to be very time-consuming. Additionally, the annealing conditions had to be set very preciously and were usually very sensitive to the initial chlorine concentration at each sample. The duration of each annealing step was unclear as well.

Hence, a precious *"in-situ"* high-temperature Hall effect measurement needs to be done for a deeper understanding of chemical diffusion, which seems to be an important parameter for setting a proper annealing condition. Chapters 5 and 6 are dedicated to the detailed study of such an effect and studies of diffusion characteristics represent thus a core of this thesis.

The *"in-situ"* high-temperature Hall effect measurements proved a hidden temperature-activated source of chlorine. Its detailed study represents a second key part of this thesis. Chapter 7 is dedicated to positron annihilation experiments, which allow us to, at least, partially find and prove a secret chlorine source, which is temperature-activated.

Finally, all findings from previous chapters are joined at Conclusion, which holistically summarizes the entire experimental investigation .

1. Introduction to CdTe and CdZnTe

Cadmium telluride (CdTe) crystallizes in a cubic zinc-blende structure[24]. It is formed by a pair of interpenetrating, face-centered, cubic sublattices (one contains only Cd atoms and the other Te atoms). These sublattices are offset from each other by one-quarter of a unit cell body diagonal, see Fig. 1.1.

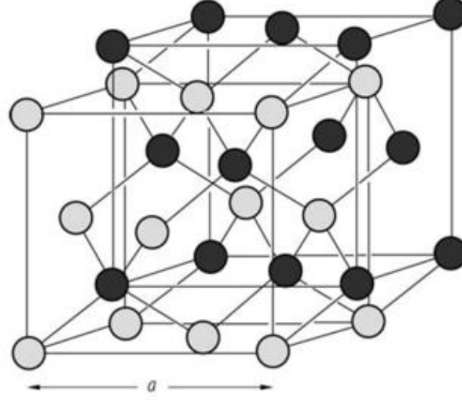

Figure 1.1: Zinc-blende crystal structure[25]

Fundamental physical parameters of CdTe are presented in Table 1.1.

Table 1.1: Overview of physical parameters CdTe at 300 K and pressure 1 atm.[25,26]

Parameter	Value
Density ρ ($\mathrm{g\,m^{-3}}$)	5.85
Weight of one molecule M ($\mathrm{g\,mol^{-1}}$)	240.01
Lattice constant a $\left(\mathrm{\AA}\right)$	6.482
Melting point t_m (°C)	1092
Boiling point t_b (°C)	1130
Relative permittivity ε_r	10.2
Electron mobility μ_e ($\mathrm{cm^2\,V^{-1}\,s^{-1}}$)	1050
Hole mobility μ_h ($\mathrm{cm^2\,V^{-1}\,s^{-1}}$)	100

1.0.1 Band structure

CdTe is a direct semiconductor with a relatively large band-gap ($\sim 1.56\,\text{eV}$ at $300\,\text{K}$). The real band-gap was calculated and experimentally proved several times[25]. The graphical visualization of the band-gap can bee seen in Fig. 1.2.

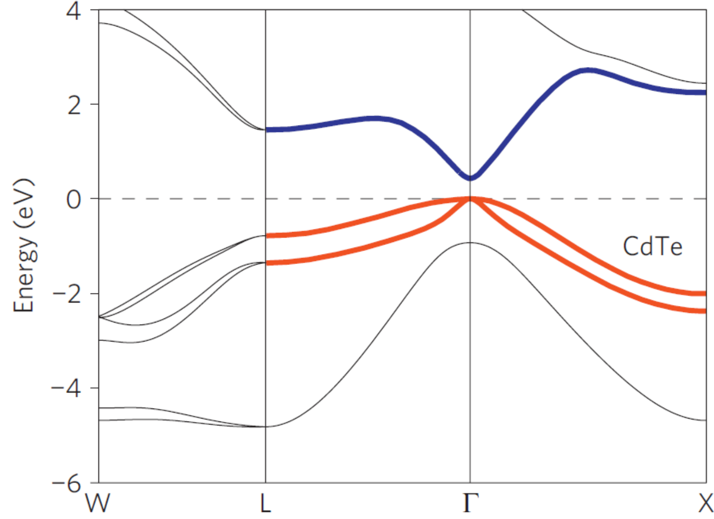

Figure 1.2: band-gap structure CdTe[27]

The temperature dependency of the band-gap of CdTe at temperature range $300 - 1000\,\text{K}$ was described by Grill[28]:

$$E_g(T) \quad = \quad 1.622 - 3.5 \times 10^{-4} T - 1.1 \times 10^{-7} T^2 \,(\text{eV}). \tag{1.1}$$

Point defects form energy levels in the band-gap and affect thereby the resistivity and the mobility lifetime product[29]. CdTe can be alloyed with Zn forming CdZnTe ternary compound. Alloying of CdTe with Zn strengthens the lattice and increases the band-gap and thereby also the maximal achievable resistivity[30].

2. Crystal defects

2.1 Introduction

Microscopic crystal defects play a crucial role in the electrical properties of semiconductors and these properties can be controlled by a crystal growth condition, intentional doping and post-grown annealing.

2.2 Thermodynamic theory of Cd(Zn)Te growth

The thermodynamic system contains φ phases and consists of c components, whereas the number of degrees of freedom Φ is described by the Gibbs phase rule[31]

$$\Phi = c - \varphi + 2 \tag{2.1}$$

During CdTe solidification, there are two phases (liquid and solid, $\varphi = 2$) and because CdTe is a binary compound, two components Cd and Te ($c = 2$) are present. The number of degrees of freedom is thus equal to 2. Therefore, for a defined compound composition, the equilibrium can be achieved by ensuring a certain interval of intensive quantities – temperature and pressure of the system. It leads to a three-dimensional system given by the composition x, temperature T and partial pressure P. This 3-dimensional $P - T - x$ phase diagram (solid and liquid lines) is shown for CdTe[32] in Fig. 2.1. Cd pressure maximum is represented by VLS (vapour-liquid-solid CdTe) equilibrium and Cd pressure minimum is represented by SLV (solid CdTe-liquid-vapour) equilibrium. VLS and SLV curves are based on liquid-vapor equilibrium for pure cadmium or tellurium, respectively. S = V line represent equilibrium between solid CdTe and vapor pressure and it is a so-called sublimation line. The stable CdTe can not exist out of the area, which is bordered by curves in Fig. 2.1.

The projection of Fig. 2.1 to defined pressure is plotted at Fig. 2.2, where individual areas ①, ②, ④, correspond to liquid, mix of liquid and solid and purely solid CdTe. Line ③ is an ideal solidification line. The point 1092 °C is called *Congruent melting point (CMP)* and corresponds to the same Cd and Te composition of solid and liquid. Due to this fact, it is an ideal starting point for solidification.

Pressure P_{Tot} in a closed system is given by *Dalton's law* as a sum of partial pressure of individual compounds. It is defined, for CdTe, by partials tellurium and cadmium pressure, P_{Te_2}, P_{Cd}, respectively.

$$P_{Tot} = P_{Te_2} + P_{Cd}. \tag{2.2}$$

Two partial pressures of independent compound are connected[34], with an assumption of low concentrate gas at dynamics equilibrium, using *Law of mass action* by *equilibrium constant* K_{CdTe}:

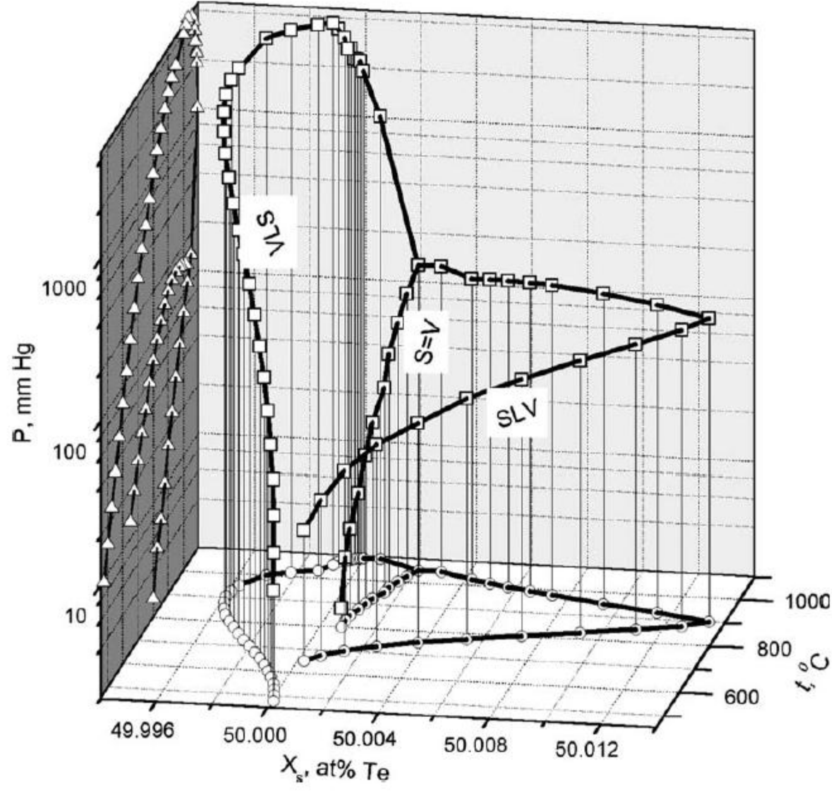

Figure 2.1: 3-dimensional $P-T-x$ phase diagram (solid and liquid lines) for CdTe. Value $x = 0.5$ corresponds to CdTe containing exactly 50% Cd atoms and 50% Te atoms. VLS curve corresponds to vapour-liquid-solid CdTe equilibrium for pure Cd. SLV correspond to solid CdTe-liquid-vapour equilibrium of pure Te. $S{=}V$ curve is called sublimation line and represents an equilibrium between solid CdTe and vapour pressure.

$$P_{Cd}P_{Te_2}^{\frac{1}{2}} \quad = \quad K_{CdTe}(T), \tag{2.3}$$

where T is temperature.

The projection of Fig. 2.1 to defined pressure is plotted at Fig. 2.3.

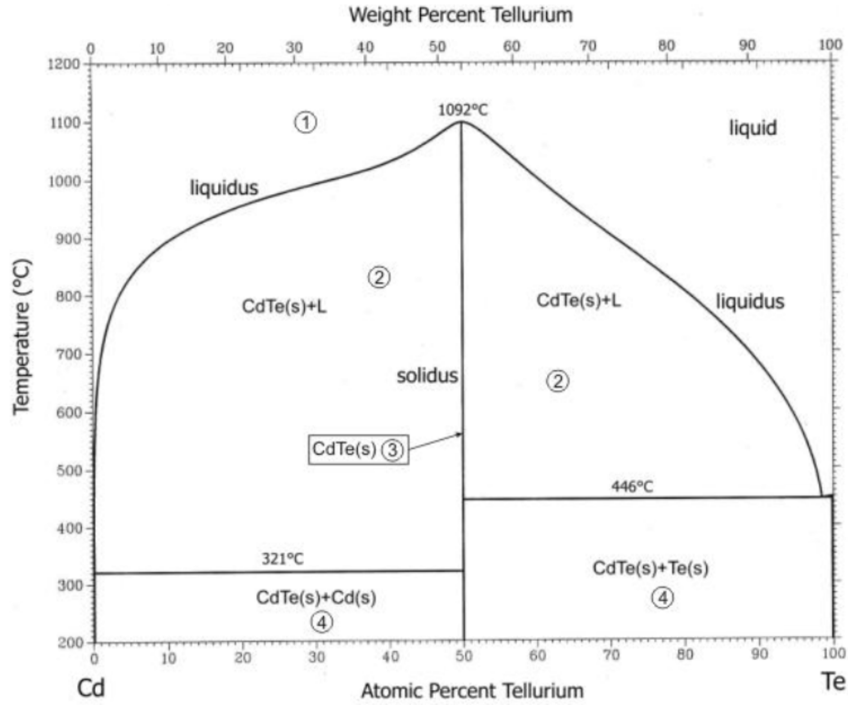

Figure 2.2: Equilibrium $T - x$ diagram of CdTe[33]. Areas ①, ②, ④, correspond to liquid, mix of liquid and solid and purely solid CdTe. Line ③ is an ideal solidification line. The point 1092 °C is *Congruent melting point*.

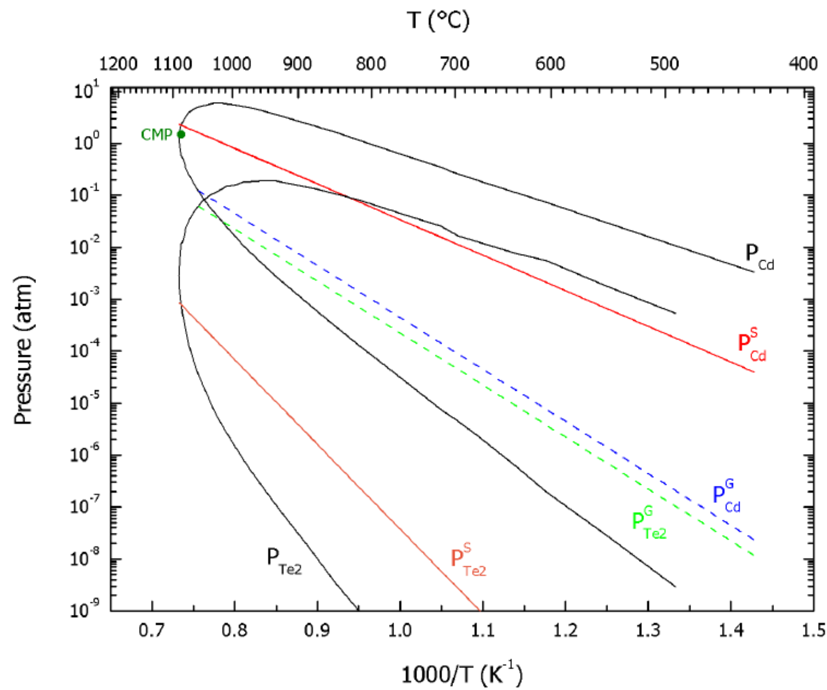

Figure 2.3: Curves P_{Cd} and P_{Te_2} are borders between liquid, vapor and solid. Lines P^S_{Cd}, $P^S_{Te_2}$ are stoichiometric lines (coefficient $x = 0.5$). Line P^G_{Cd}, $P^G_{Te_2}$ are sublimation lines according to partial pressure (Cd, Te_2).[35]

Ideal crystal growth is based on solidifying the melt with a stoichiometric composition using starting materials that are as pure as possible ($6N - 7N$). During the solidification, the system state proceeds through the CMP, where melt and occurring solid states have the same composition. As the melt is solidified, the system state should follow the s line in the $T - x$ diagram and simultaneously the stoichiometric line in the $P - T$ diagram by controlling the crystal growth temperature and P_{Cd} of the system[36]. However, as can be seen in Fig. 2.3, the CMP is slightly shifted to the composition with tellurium excess. This shifting is caused by a different solubility of Cd and Te at liquid and solids CdTe. It yields to a necessary shift of the system state towards the stoichiometric line after the solidification of the melt.

However, the described situation represents only an ideal case of solidification. During the real crystal growth, deviations from the presented situation can occur, leading to generation of various defects having different sizes and distribution.

2.3 Bulk defects

The complexity of the crystal growth process makes it very difficult to follow the ideal crystallization conditions precisely and maintain the stoichiometry in the entire crystal volume. Therefore, nonstoichiometry growth is commonly present.

The detailed view on the stoichiometric line from Fig. 2.2 is presented at Fig. 2.4. Because of the different solubility of Cd and Te at liquid and solid mentioned above, the change of nonstoichiometric system condition back to the stoichiometric line after crystallization initialization has time-dependent dynamics. It leads to mass defects formation:

Inclusions are formed during the solidification of the melt due to thermal fluctuations on the crystallization interface, which leads to capturing of melt droplets[37,38]. Depending on the excess component in a droplet, either star-shaped Cd-inclusions or triangular and hexagonal Te-inclusions may be formed. Because of their size of up to tens of micrometers and strong IR absorption, inclusions are easily investigated by means of IR microscopy.

Precipitates are formed during cooling of the solidified crystal due to retrograde solubility, see Fig. 2.4, of excessed component from the solid to the liquid[37]. It has sizes up to tens to hundreds of nanometers. Precipitates may be formed randomly within the whole volume of the crystal (homogeneous precipitation); however, precipitation takes place much easier on the crystal imperfections, e.g. along dislocations, twin or grain boundaries (heterogeneous precipitation)[38].

Voids are small regions containing no atoms and can be thought of as clusters of vacancies. However, their origin is still unresolved.

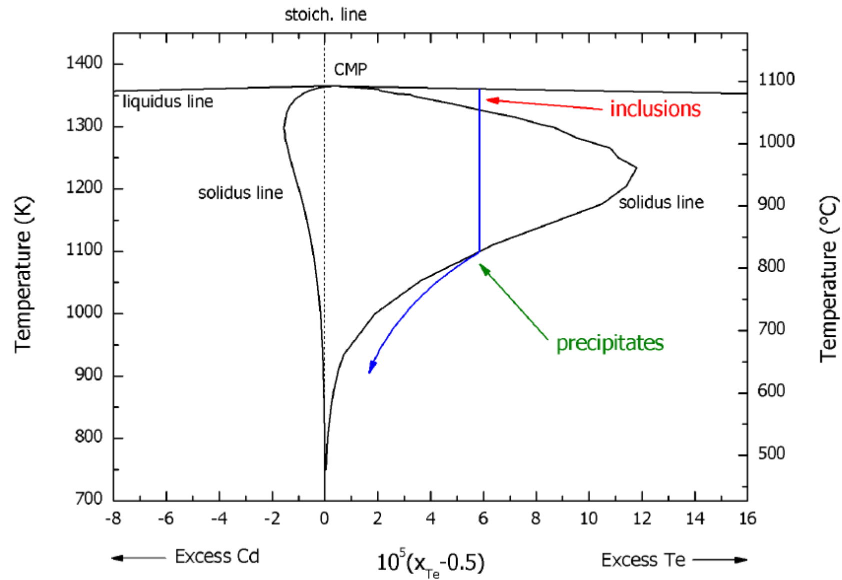

Figure 2.4: Detailed view on the stability region of CdTe defined by the solid lines[35].

2.4 Plane defects

Bulk CdTe usually contains following types of plane defects:

Grain boundaries are the most common type of planar defects. They are created during the solidification of the melt when grains growing from different nucleation centers meet with lattice orientations. The size and number of grain boundaries depend on growth conditions, supercooling of the melt, purity of the material and crucible, vibrations, ...

Twin boundaries happens when crystals on either side of a plane are mirror images of each other. The boundary between these twinned crystals will be either single- or multiple-plane of atoms. There is no region of disorder and boundary atoms can be perceived as belonging to the crystal structures of both twins.

Plane defects are easily observable by a visual inspection on roughly polished wafers, in IR transmittance images, or by X-ray diffraction topography.

2.5 Line defects

These crystal defects are oriented along a particular line. Typically, dislocations are formed during crystal growth to release the stress-induced within the material due to solidification of the melt in a crucible, which sustains the melt in a fixed volume, disabling a free

expansion to an empty space[38,39]. However, external mechanical stress added after growing could also generate a dislocation.

Edge dislocations are formed during solidification, where external stress is relaxed using bypassing of a part of an atomistic layer. It leads to a deformation of surrounding crystal's lattice. The edge dislocations are visualized in Fig. 2.5a

Screw dislocations compensate external stress by atomic layer shifting. See Fig. 2.5b.

Mixed dislocations combine both previously described dislocations simultaneously.

Dislocation density, the total length of dislocations in a unit volume of a material, can be revealed by measuring the etch pits density[39].

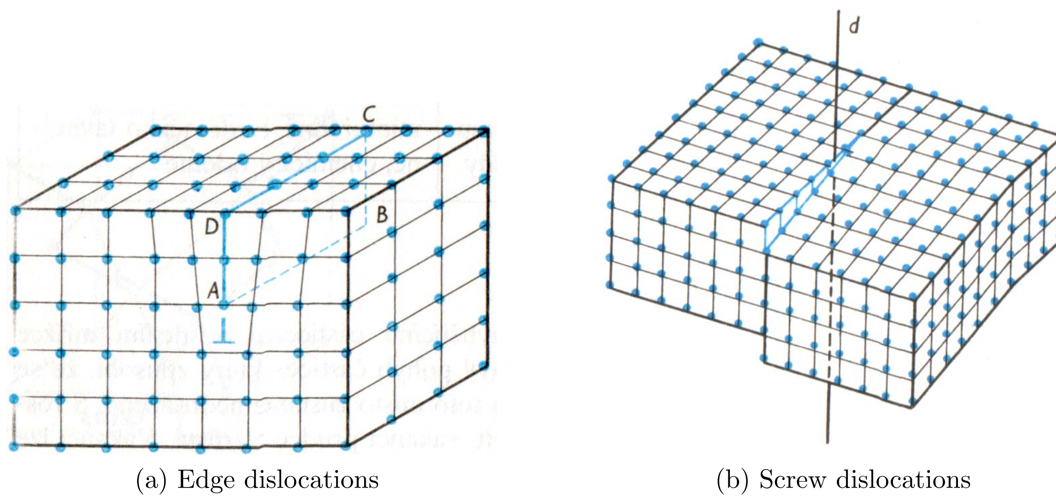

(a) Edge dislocations

(b) Screw dislocations

Figure 2.5: Visualization of dislocation

2.6 Point defects

The totally defect-free material, described below, can be considered only at absolute zero temperature, $T = 0\,\mathrm{K}$. At non-zero temperatures, deviations from an ideal distribution of atoms occur and various point defects are formed.

Thermodynamic calculations of defect equilibria established under specific external conditions (temperature, pressure of the gas phase of one component of compound in case of binary compound) can be treated in a quasi-chemical formalism, based on the knowledge of the formation energies and structure of defect's energy levels in the bandgap, see Fig. 2.6. Point defects form energy levels in the bandgap and affect thereby the resistivity and the mobility lifetime product[29].

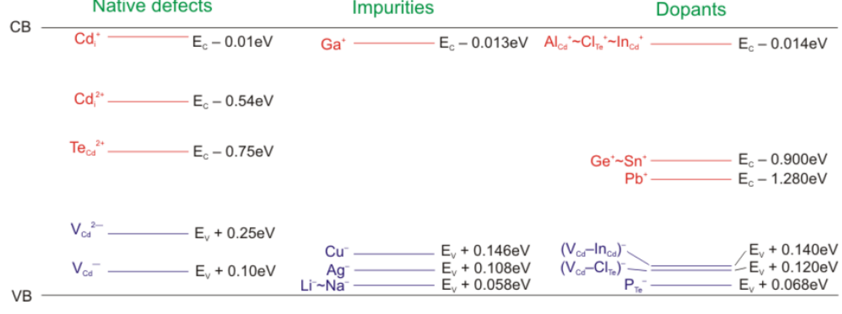

Figure 2.6: Scheme of energy levels of the most common native defects, impurities and dopants in CdTe[25,36]. Red lines represent donor levels, blue lines denote acceptor levels.

Various indirect methods can be used for investigation of both shallows, the defects near valance or conductive band, and deep, near the middle of bandgap, levels in the bandgap, including photoluminescence (PL), photo-induced current transient spectroscopy (PICTS), deep-level transient spectroscopy (DLTS), thermoelectric emission spectroscopy (TEES), Hall effect measurements, etc. However, identification of observed energy levels with particular defects is not necessarily an easy task.

Native defects, which are formed in a binary compound CdTe are:

vacancies V_{Cd} **,** V_{Te}, missing atoms at periodical structure of crystal lattice.

interstitials Cd_I **,** Te_I**,** native atoms beyond periodic crystal lattice.

antisite defects Cd_{Te} **,** Te_{Cd}, native atoms in the possition of the second sublattice.

their **complexes**, like Frenkel defects $V_{Cd} - Cd_I$, $V_{Te} - Te_I$, complex of $Cd_{Te} - V_{Cd}$, etc.

Dominant donor-like native defects in CdTe crystals grown at Cd-rich atmosphere are singly- and doubly-ionized interstitials, Cd_I^+ and Cd_I^{2+}, and doubly-ionized antisites, Te_{Cd}^{2+}. The main acceptor-like native defects are singly- and doubly-ionized vacancies, V_{Cd}^- and V_{Cd}^{2-}[18,25,40].

Extrinsic defects are undesirable impurities present in the crystal. The concentration of impurities should be reduced to reach a level below native point defects, therefore under approximately $1 \times 10^{15}\,\mathrm{cm}^{-3}$ at room temperature. However, extrinsic defects are also induced by dopants intentionally introduced into the material to control any modifications of its properties.

Complex defects are mainly combination of native and extrinsic defects to complex structures. One of the most important defect complexes is an acceptor-like

complex of Cd vacancy and substitutional atom, called **A-centers**: $\left(V_{Cd}^{2-} - Cl_{Te}^{+}\right)^{-}$ in the case of Cl and $\left(V_{Cd}^{2-} - In_{Cd}^{+}\right)^{-}$ in the case of In.

Determining properties of native point defects and their complexes is particularly important to understand their role in crystal growth and extrinsic defects compensation.[18] Despite extensive investigations, defects attached to distinct levels have not been completely identified in most cases.

High purity CdTe/CdZnTe crystals are usually grown under Te-rich conditions because Cd pressure required for Cd-rich conditions is as high as several atmospheres[41]. The CdTe/CdZnTe crystals grown under Te-rich conditions are typically characterized by a low resistivity and p-type conductivity[18] due to Cd vacancies (V_{Cd}) which are divalent acceptors with two ionization levels $(0/-)$ and $(-/2-)$ located below the mid-gap level.[18,40] Achieving high resistivity V_{Cd} acceptors and residual impurities must be electrically compensated, usually by doping using group III (Al, In, Ga) or group VIII (Cl) donors.[18,40]

2.6.1 Defects statistic

Theoretical background for defects statistic was set by Kröger[42] in 1973. The following subsection summarizes his results.

Vacancies (V_{Cd})

Thermodynamic equilibrium between solid CdTe in non-stoichiometry state surrounded by gas Cd (Cd_{Gas}) are described as

$$CdTe \rightleftarrows V_{Cd}Te + Cd_{Gas}. \tag{2.4a}$$

The concentration of non-ionized vacancies $[V_{Cd}^{0}]$ can be written as

$$[V_{Cd}^{0}] = \frac{K_{V_{Cd}^{0}}}{p_{Cd}}, \tag{2.4b}$$

where p_{Cd} is a partial pressure of Cd_{Gas} and $K_{V_{Cd}^{0}}$ is an equilibrium constant defined by

$$K_{V_{Cd}^{0}} = n_0 (k_b T)^{\frac{5}{2}} \left(\frac{m_{Cd}}{2\pi\hbar^2}\right)^{\frac{3}{2}} \exp\left(\frac{S_{V_{Cd}^{0}}}{k_b}\right) \exp\left(-\frac{H_{V_{Cd}^{0}}}{k_b T}\right), \tag{2.4c}$$

where m_{Cd} is Cd mass, $n_0 = 1.48 \times 10^{22}\,\mathrm{cm}^{-3}$ is the Cd or Te atom density, $\hbar = \frac{h}{2\pi}$ is *reduced Planck constant*, k_b *Boltzmann constant*, $H_{V_A^0}$ enthalpy and $S_{V_A^0}$ entropy.

Concentration of singly charged vacancies $\left[V_{Cd}^{-}\right]$ and doubly charged vacancies $\left[V_{Cd}^{2-}\right]$ are described using approximation to Boltzman statistic as

$$\left[V_{Cd}^{-}\right] = \frac{g_{V_{Cd}^{-}}}{g_{V_{Cd}^{0}}} \exp\left(\frac{E_F - E_{A_1}}{k_b T}\right) \left[V_{Cd}^{0}\right], \tag{2.4d}$$

$$\left[V_{Cd}^{2-}\right] = \frac{g_{V_{Cd}^{2-}}}{g_{V_{Cd}^{-}}} \exp\left(\frac{E_F - E_{A_2}}{k_b T}\right) \left[V_{Cd}^{-}\right], \tag{2.4e}$$

where g stands for a degeneracy factor incident to each ionize level. E_F is *Fermi level*, which depends on temperature and equilibrium concentration of free charge carriers, acceptors and donors. The E_{A_1}, E_{A_2}, where $E_{A_1} < E_{A_2}$, correspond to the activation energy of singly and doubly charged V_{Cd} levels.

Interstitials (Cd_I)

Similar approach is used also for Cd interstitials:

$$Cd_{Gas} \rightleftarrows Cd_I \tag{2.5a}$$

$$\left[Cd_I^0\right] = K_{Cd_I^0} p_{Cd}, \tag{2.5b}$$

$$K_{Cd_I^0} = n_0 (k_b T)^{-\frac{5}{2}} \left(\frac{m_{Cd}}{2\pi\hbar^2}\right)^{-\frac{3}{2}} \exp\left(\frac{S_{Cd_I^0}}{k_b}\right) \exp\left(-\frac{H_{Cd_I^0}}{k_b T}\right), \tag{2.5c}$$

$$\left[Cd_I^{+}\right] = \frac{g_{Cd_I^{+}}}{g_{Cd_I^{0}}} \exp\left(-\frac{E_F - E_{A_1}}{k_b T}\right) \left[Cd_I^{0}\right], \tag{2.5d}$$

$$\left[Cd_I^{2+}\right] = \frac{g_{Cd_I^{2+}}}{g_{Cd_I^{+}}} \exp\left(-\frac{E_F - E_{A_2}}{k_b T}\right) \left[Cd_I^{+}\right]. \tag{2.5e}$$

The E_{A_1}, E_{A_2} , where $E_{A_2} < E_{A_1}$, correspond to the activation energy of singly and doubly charged Cd_I levels.

Antisite defects Te_{Cd}

Similar approach is used also for Antisite:

$$2CdTe \rightleftarrows Te_{Cd}Te + 2Cd_{Gas} \tag{2.6a}$$

$$[Te^0_{Cd}] = \frac{K_{Te^0_{Cd}}}{p^2_{Cd}}, \tag{2.6b}$$

$$K_{Te^0_{Cd}} = n_0(k_bT)^5 \left(\frac{m_{Cd}}{2\pi\hbar^2}\right)^3 \exp\left(\frac{S_{Te^0_{Cd}}}{k_b}\right) \exp\left(-\frac{H_{Te^0_{Cd}}}{k_bT}\right), \tag{2.6c}$$

$$\left[Te^+_{Cd}\right] = \frac{g_{Te^+_{Cd}}}{g_{Te^0_{Cd}}} \exp\left(-\frac{E_F - E_{A_1}}{k_bT}\right)\left[Te^0_{Cd}\right], \tag{2.6d}$$

$$\left[Te^{2+}_{Cd}\right] = \frac{g_{Te^{2+}_{Cd}}}{g_{Te^+_{Cd}}} \exp\left(-\frac{E_F - E_{A_2}}{k_bT}\right)\left[Te^+_{Cd}\right]. \tag{2.6e}$$

.

2.6.2 Reaching of high resistivity - Defects compensation

Point defects compensation is crucial for reaching a high-resistive state with resistivity higher than $1 \times 10^9\,\Omega\,\text{cm}$, which is necessary for CdTe radiation detectors to minimize dark current at room temperature. There are several possibilities how to achieve an optimal point defects compensation:

Shallow defect One way how to successfully accomplish a high resistivity is to precisely compensate shallow charged defects while pinning the Fermi level on a deep level in the midgap. It is realized usually by doping using elements from group I, III (Al, In, Ga) or group VII (Cl)[18,40,43]. Group I elements on Cd sites act as acceptors, while they act as donors on interstitial sites[44]. Group III elements on Cd sites and group VII elements on Te sites form donor levels. Doping by these elements compensates impurities and native defects in undoped materials[35,36,45–47]. Nowadays, the most important shallow dopants of CdTe are In and Cl.

The concentration of individual point defects is connected with free carriers n/p concentration through the equation of electrical neutrality:

$$n + \left[V_{Cd}^{-}\right] + 2\left[V_{Cd}^{2-}\right] + \left[A^{-}\right] + \left[A_{C}^{-}\right] = \dots \tag{2.7a}$$

$$\dots = p + \left[Cd_{I}^{+}\right] + 2\left[Cd_{I}^{2+}\right] + \left[D^{+}\right]$$

$$\left(V_{Cd}^{2-} + In_{Cd}^{+}\right)^{-} = A_{C_{In}}^{-} \tag{2.7b}$$

$$\left(V_{Cd}^{2-} + Cl_{Te}^{+}\right)^{-} = A_{C_{Cl}}^{-} \tag{2.7c}$$

$$In_{Cd}^{+},\, Cl_{Te}^{+},\, D^{+} = D^{+} \tag{2.7d}$$

$$Ag_{Cd}^{-}, P_{Te}^{-}, \dots = A^{-} \tag{2.7e}$$

where n a p stand for a concentration of free electrons or holes. D^{+} and A^{-} are unknown donors and acceptors and square brackets represent their concentration. A_{C}^{-} represents a complexed defect, resp. a combination of vacancies and dopants.

In and Cl dopants interact with $CdTe$ by creating various type of defects. Total $[In]$ or $[Cl]$ concentration may by described by following equations:

$$[In] = \left[In_{Cd}^{0}\right] + \left[In_{Cd}^{+}\right] + \left[\left(V_{Cd}^{2-} + In_{Cd}^{+}\right)^{-}\right] + \left[In_{I}^{-}\right], \tag{2.8a}$$

$$[Cl] = \left[Cl_{Te}^{0}\right] + \left[Cl_{Te}^{+}\right] + \left[\left(V_{Cd}^{2-} + Cl_{Te}^{+}\right)^{-}\right] + \left[Cl_{I}^{-}\right]. \tag{2.8b}$$

The concentration of chlorine **A-centres** is defined as

$$\left[\left(V_{Cd}^{2-} - Cl_{Te}^{+}\right)^{-}\right] = \left[A_{C_{Cl}}^{-}\right] = \frac{g_{V_{Cd}^{2-}}}{g_{V_{Cd}^{-}}}\left[A^{0}\right]\exp\left(\frac{E_F - E_a}{k_b T}\right), \tag{2.9a}$$

$$\left[A_{C_{Cl}}^{0}\right] = \frac{g_A}{n_0}\left[V_{Cd}^{-}\right]\left[Cl_{Te}^{+}\right]\exp\left(-\frac{E_A}{k_b T}\right), \tag{2.9b}$$

where $n_0 = 1.48 \times 10^{22}\,\mathrm{cm}^{-3}$ is the Cd or Te atom density, k_b *Boltzmann constant* and T temperature in K. The g_x is a degeneracy factors incident to each ionize level. E_F is *Fermi level*, which depends on a temperature and an equilibrium concentration of free charge carriers, acceptors and donors. The E_a correspond to ionization energy level of A-centre and E_A correspond to its formation energy (negative).

Deep defect Dopants of transition metals occupy the *Cd* site and form near midgap donor levels[48]. High resistivity states can be reached by doping with vanadium or copper. Although copper doping increases material resistivity, it reduces carrier's lifetimes[49]. Another alternative is to use dopping by elements from IV group (*Ge*, *Sn*)[50].

Disorder tuning CdTe can be alloyed with *Zn* forming *CdZnTe* ternary compound. Alloying of CdTe with *Zn* strengthens the lattice and increases the bandgap and thereby also the maximal achievable resistivity[30].

A detailed overview of the impact of dopants on detector material properties can be found in [51]. For the determination of the properties of native point defects and their complexes, see Fig. 2.7. It is essential to understand their role in crystal growth and the compensation of extrinsic defects.[18]

Despite extensive investigations, the defects attached to distinct levels have not been completely identified in most cases, therefore significant parts of this thesis focus primarily on these scenarios.

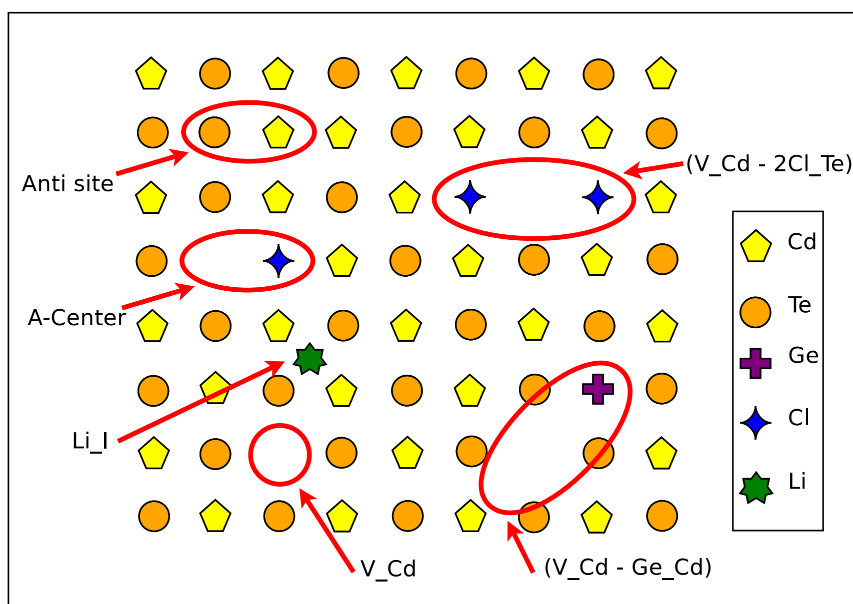

Figure 2.7: Illustration of several points defects at CdTe and its complexes

3. Inclusion elimination

3.1 Introduction

Based on the details of growth conditions, see Chapter 2.3, CdTe crystals contain several types of bulk defects. Inclusions, one of the most crucial bulk defects (mainly with a triangle, hexagonal or star shape) are commonly observed in CdTe-based X-ray and gamma-ray bulk detectors. They play a crucial role in crystal quality since they are strongly affecting their detection ability[18]. Inclusions, which size is usually a few tens of microns, do not affect much the quality of large detectors $(1\times1\times1)$ cm^3 with two planar electrodes on opposite surfaces. However, in the case of detectors, in which pixel pitch $(\sim 250\times250)$ µm^2 is comparable to inclusion size, the inclusion plays a role as a trapping center for electrons and significantly decreases the collection of charge generated by absorption of high-energetic photons under affected pixels considering an extensive dislocation network around the inclusion.

Hence, it is necessary to develop a technology enabling to suppress the formation of inclusions during the crystal growth or, if inclusions are already present in existing crystals, to find an effective procedure for their post-growth elimination.

One possibility of eliminating existing inclusions represents annealing in one of the native component vapors, Cd or Te. Few contradictory works described a chemical composition of inclusions and suggested a suitable annealing treatment reducing the size of inclusions.

Identification of a triangle, hexagonal and star-shaped inclusion was unresolved for a long time. For example, Rudolph[41,52] reported six-pointed star-shaped Te inclusions, on the contrary to Brion[53] and Sen[21], whose star-shaped inclusions contained much more Cd than Te. Fortunately, triangle-shaped inclusions are usually described as Te-rich inclusions[21,54–56].

After the first annealing experiments, the situation became even more complicated. Initial experiments were focused only on improving the IR transmittance of $CdZnTe$ by annealing under Cd overpressure without any detailed inclusion investigation[57,58]. Further investigations were more precious however, their results were sometimes contradictory. At that time, Shen[59] and Ayoub[60,61] published some works with annealing CdTe at different annealing conditions. In addition, a few experiments were focused on the elimination of triangle-shaped inclusions by their thermomigration in a temperature gradient[62–64].

Nowadays, the situation around inclusion and annealing has become stable. The star-like inclusion was identified as a Cd inclusion and triangle or hexagonal inclusion contains mostly Te[25,37].

However, the situation around annealing still stays unclear. A few works are focused on a process of annealing at Cd or Te overpressure, which usually successfully reduces inclusion's density and size. However, crystals reannealed in such a way are usually not useful from the detector's point of view because of their low resistivity. Bugár studied IR

transmission of CdTe doped by In ($CdTe : In$)[65] and managed to prove and explain the connection between annealing conditions and IR transmission. Fochuk[66] has introduced the influence of high-temperature annealing to precipitates' elimination. Belas[67] studied $CdTe : In$, proved the inclusion elimination and preciously explained the influence of annealing conditions, especially on the cooling rate to high resistivity crystals production. In addition, Belas at his later work[47] introduced a two-step annealing of $CdTe : In$. This technique was based on annealing at Cd overpressure for inclusion elimination followed by annealing at Te overpressure, which restore high resistivity of the sample. Bugár[68] and Franc[69] have expanded his work to measurement of CdTe doped by chlorine ($CdTe : Cl$).

Following Sections summarise an experimental research focused to inclusion reduction at as grown CdTe : Cl with similar growing condition, where each of them contained different inclusion type by a two-step annealing. The experiments were performed to effectively eliminate both types of inclusions by a one-day annealing and compared the behavior of both crystals. The detailed experimental technique is described in detail and reached results are discussed. The results presented in this chapter were successfully published in **Franc, J., Šedivý, L., Belas, E., Bugár, M., Zázvorka, J., Pekárek, J., Uxa, Š., Höschl, P. & Fesh, R. Melt growth and post-grown annealing of semiinsulating (CdZn)Te by vertical gradient freeze method. *Crystal Research and Technology* 48, 214–220. ISSN: 02321300 (2013)**.

3.2 Experimental techniques

3.2.1 Sample preparation

Single CdTe crystals were grown by the vertical gradient freeze method[70] (using 6N purity source elements). Crystal ingots were cut to (5×5) mm^2, which were subsequently polished and etched in 3% bromine-methanol. For more details, see Appendix A.2.

3.2.2 Annealing

A sample was placed to one end of a cleaned, see appendix A.1, quartz ampoule, Cd or Te were placed to another end. The filled ampoule was evacuated to vacuum about 5×10^{-6} mbar, sealed and placed into a two-zone furnace. The two-zone temperatures were regulated independently by a three-looped thermoregulator EUROTHERM 2704 and controlled by using a corresponding PC software. Afterward, the sample was placed to the part of the ampoule containing higher temperature (T_S), whereas the metal source was placed to the coldest part of the ampoule (T_P) to enable pressure controls. Temperature of both the sample as well as the metal source was checked by two thermocouples of type S (Pt; $Pt - Rh$) placed close to the ampoule. Scheme of this experimental setup is presented at Fig. 3.1

In case of Cd overpressure annealing, partial Cd pressure P_P^{Cd} is connected with T_P^{Cd} by equation[45]

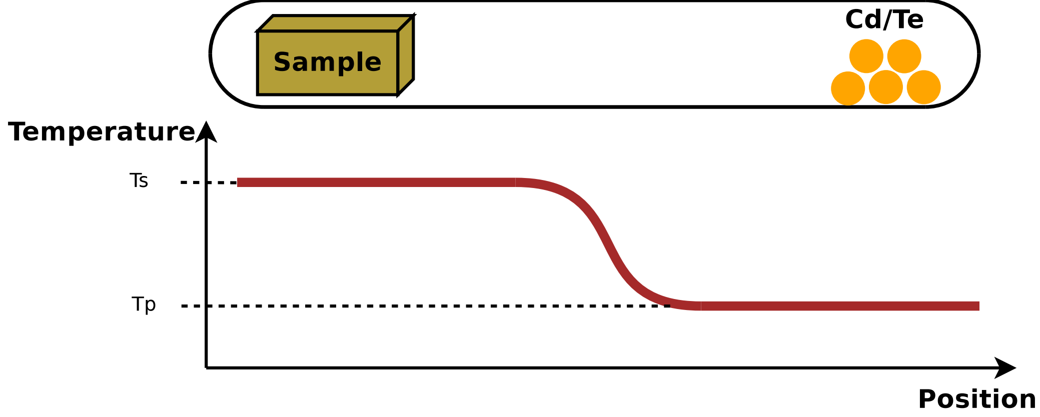

Figure 3.1: Scheme of annealing in a two-zone furnace. T_S, T_P correspond to sample and metal temperature, respectively.

$$\log P_P^{Cd} = \left(-\frac{5317}{T_P^{Cd}(\mathrm{K})} + 5.119\right)(atm). \tag{3.1}$$

In case of Te overpressure annealing, the connection between P_P^{Te} and T_P^{Te} depends on temperature range[45]:

$$\text{for } \mathrm{T_{Te}} < 800\,\mathrm{K} \quad : \quad \log P_P^{Te} = \left(5.069 - \frac{6258.6}{T_P^{Te}(\mathrm{K})}\right)(atm). \tag{3.2a}$$

$$\text{for } \mathrm{T_{Te}} \in (800, 921)\,\mathrm{K} \quad : \quad \log P_P^{Te} = \left(4.870 - \frac{6099.23}{T_P^{Te}(\mathrm{K})}\right)(atm). \tag{3.2b}$$

$$\text{for } \mathrm{T_{Te}} > 921\,\mathrm{K} \quad : \quad \log P_P^{Te} = \left(4.719 - \frac{5960.2}{T_P^{Te}(\mathrm{K})}\right)(atm). \tag{3.2c}$$

3.2.3 Infrared microscopy

An optical inverted microscope OLYMPUS IX70 was used for inclusion observation. A halogen lamp was used as a source of the continuous emission spectrum, which was filtered by an infra-red edge filter. Radiation penetrating through CdTe crystal with IR transmission $> 60\%$ was detected by an infra-red sensitive CCD camera. For defects' magnification, three objectives OLPYMPUS RMS $4x$, $10x$ and $20x$ were used.

Cd/Te-based inclusion present in CdTe has absorbed the near-infrared radiation and has formed dark objects in IR microscope images. Hence, IR microscopy is a useful technique for characterization of inclusions with the size above 1 µm[36]. IR microscope images were taken using the NIS ELEMENTS software.

3.2.4 Room temperature Hall effect

The electrical conductivity/resistivity (σ/ρ), concentration (n/p) and mobility (μ) of major free carriers of CdTe were measured by two different experimental techniques.

Classical Hall bar configuration

Silver wires with a diameter 50 µm were soldered by In to Au contacts prepared by chemical deposition with 10% aquaeous solution of $AuCl_3$, see Appendix A, at classical Hall bar configuration, see Fig. 3.2.

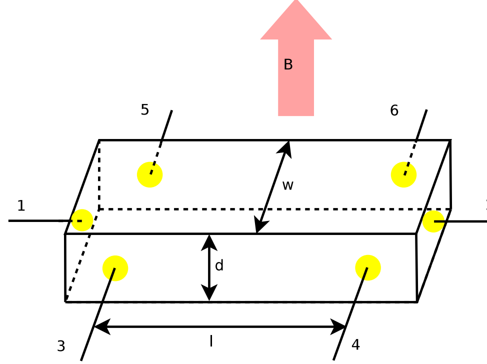

Figure 3.2: Scheme of Hall bar coated at classical 6 wires configuration. Yellow spots are Au contacted places, l, d and w correspond to sample dimension and B represents the oriented intensity of the magnetic field.

The galvanomagnetic properties were calculated using[71]:

$$\sigma \equiv \frac{1}{\rho} = \frac{l}{dw}\frac{I_{1,2}}{U_{3,4}} \quad \text{or} \quad \sigma \equiv \frac{1}{\rho} = \frac{l}{dw}\frac{I_{1,2}}{U_{5,6}} \tag{3.3}$$

$$R_H = r_H \frac{d}{B}\frac{U^0_{5,3} - U^H_{5,3}}{I_{1,2}} \quad \text{or} \quad R_H = r_H \frac{d}{B}\frac{U^0_{6,4} - U^H_{6,4}}{I_{1,2}}, \tag{3.4}$$

where l is a distance between contacts, $I_{i,j}$ is corresponding current between contacts ij, r_H scattering factor depending on temperature, where $r_H \cong 1$ stands for high degeneration, $U_{m,n}$ represents a corresponding voltage between contacts m, n. $U^0_{m,n}$ is a voltage measured without applied magnetic field. $U^H_{m,n}$ represents Hall voltage between contacts m, n measured with an applied magnetic field.

Van der Pauw configuration

Geometric transformation of the previous method[72] can be done assuming planar samples without any regular shape, see Fig. 3.3. Defining $R_1 = \frac{U_{43}}{I_{12}}$ and $R_2 = \frac{U_{14}}{I_{23}}$, together with theorem 3.5, which assume a direct relation between R_1 and R_2.

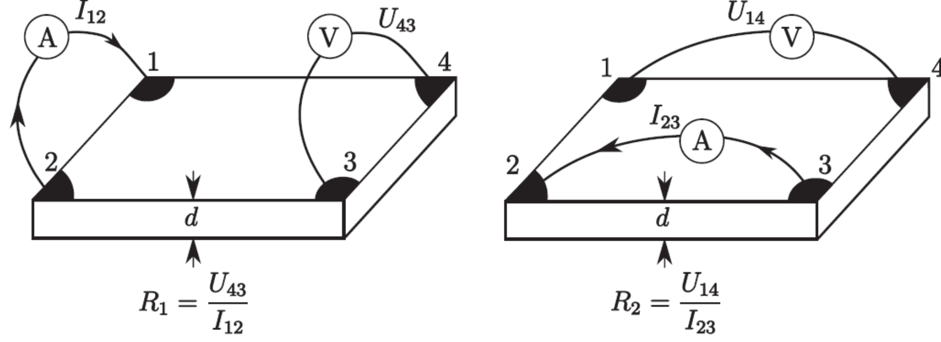

Figure 3.3: Definition of coefficients R_1, R_2 at Van der Pauw measurement for planar samples

$$\exp(-\pi d\sigma R_1) + \exp(-\pi d\sigma R_2) \equiv 1, \tag{3.5}$$

where d is a sample thickness, σ is electrical conductivity. Classical Hall bar conductivity equation 3.3 can be expressed for planar samples as

$$\frac{1}{\sigma} = \frac{\pi d}{\ln 2}\left(\frac{R_1 + R_2}{2}\right) f, \tag{3.6}$$

where f is a correction function to non-symmetric samples defined as

$$\cosh\left(\frac{\exp\left(\frac{\ln 2}{f}\right)}{\ln 2}\right) = f \cdot \frac{\left(\frac{R_1}{R_2}\right) + 1}{\left(\frac{R_1}{R_2}\right) - 1}. \tag{3.7}$$

Classical Hall constant equation 3.4 can be then expressed as

$$R_H = \frac{d}{B_Z}\left(\frac{U_{24}^0 - U_{24}^H}{I_{13}}\right), \tag{3.8}$$

where B_Z is an intensity of magnetic field perpendicular to sample surface, U^0, U^H are voltages measured without and with the magnetic field, respectively. See Fig. 3.4.

Free carriers concentration and mobility

The concentration of free carriers n/p, n for electron and p for holes as major carriers, respectively, can be calculated using

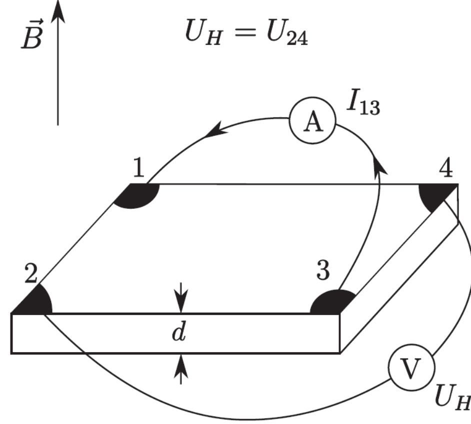

Figure 3.4: Hall constant measurement at Van der Pauw configuration for planar samples

$$n/p = \frac{r_H}{e\,|R_H|}, \tag{3.9}$$

where e is an elementary charge of an electron and r_H is a scattering factor, usually $r_H \approx 1$. The mobility of major free carriers, $\mu_{n/p}$, is given by

$$\mu_{n/p} = \frac{1}{r_H}\left|R_{H_{n/p}}\sigma_{n/p}\right|. \tag{3.10}$$

Technical realization of experimental setup

Hall switching card KEITHLEY 7065 enables switching of various combinations of input current and measured voltage on sample's contact, however, the maximal voltage applied on the switching card was limited to 10 V. KEITHLEY 220 was used as a current source; the input current was controlled by a picoammeter KEITHLEY 485. The output voltage from the sample was measured by a multimeter KEITHLEY 2000. Standard bus GPIB was used for communication among measuring devices and PC. The connection among the switching card, sample and measurement devices were realized by shielded cables with triaxial connectors. The switching electromagnet was used as a magnetic source. The scheme of this experimental setup is presented at Fig. 3.5

3.3 Results and Discussion

3.3.1 Samples

Two CdTe single crystals doped by chlorine ($CdTe : Cl$), coded by **S56** and **S57**, were grown by Vertical Gradient Freeze (VGF)[36,73] method, where the concentration of added chlorine was $[Cl]_{Added} \sim 1 \times 10^{18}\,\mathrm{cm}^{-3}$.

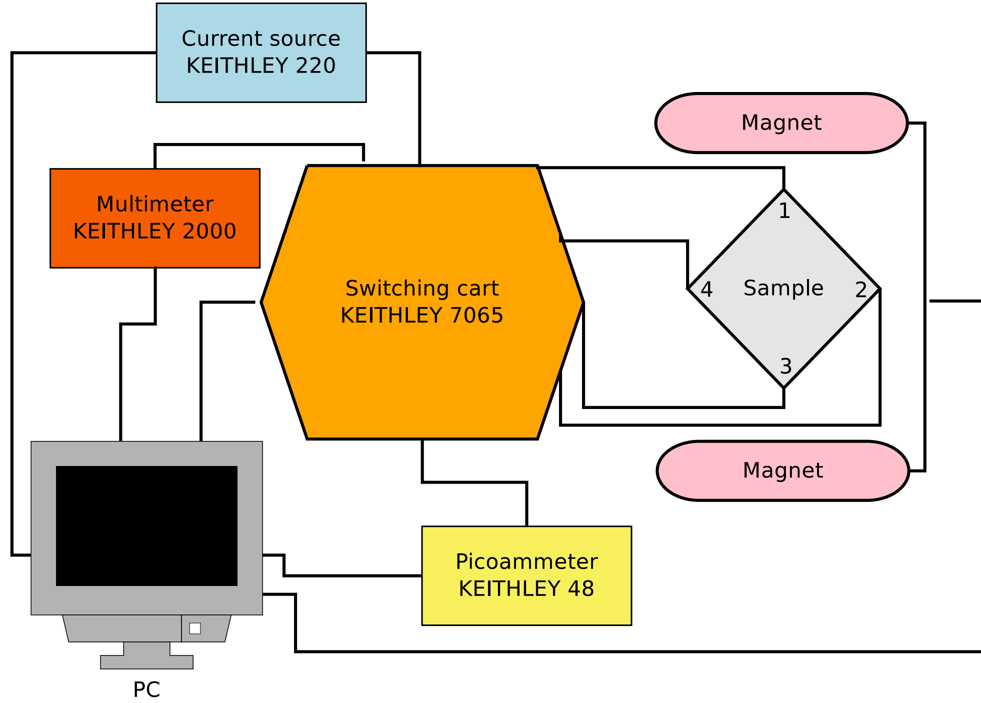

Figure 3.5: Scheme of experimental setup for Hall measurement – Van der Pauw configuration

Although both crystals, **S56**, **S57** were grown with the same chlorine dopping and the furnace was set to the same condition, samples from both crystals contain a different concentration of electrically active chlorine and different types of inclusion.

All samples were characterized by Van der Pauw Hall measurement. Samples were cut from the single crystalline part of the ingot, polished and etched (see sample preparation section A.2 at appendix) to final dimensions $5 \times 5 \times 2$ mm^3. As grown **S56** exhibits high resistivity $\rho \sim 1 \times 10^8\,\Omega\,$cm and p-type of conductivity. On the other side as grown **S57** exhibit low resistivity $\rho \sim 1 \times 10^{-1}\,\Omega\,$cm and n-type of conductivity. The overview of electrical properties is presented at Tab. 3.1. Tab. 3.1 occasionally exhibits free carrier mobility higher than theoretical electron/hole mobility in ideal crystal mentioned at Tab. 1.1. However, it is well known, that Van der Pauw Hall measurements reveals significant inaccuracy for unsymmetrical or non-homogeneous samples at carrier mobility evaluation. The aim of this chapter is focused on inclusion elimination, which is not related to precise mobility establishing. Therefore mentioned mobilities are only indicative.

Concentration of electrically active chlorine was experimentally determined by Van der Pauw Hall effect measurement after annealing at Cd overpressure[67,74]. Chlorine concentration of individual samples cut from **S56** crystal was $[Cl]_{S56} \in (3 \times 10^{16} - 2 \times 10^{17}\,\text{cm}^{-3})$ and $[Cl]_{S57} \in (3.1 \times 10^{16} - 3.7 \times 10^{16}\,\text{cm}^{-3})$ was set for **S57** crystal, respectively.

Using IR microscope we found that as-grown crystal **S56** consists of a Te inclusions and as-grown crystal **S57** Cd inclusions, respectively.

Table 3.1: The overview of electrical properties of $CdTe : Cl$ ($S56$ and $S57$) in depending on Cd- and Te-annealing

Sample	Annealing condition	ρ (Ω cm)	n/p (cm^{-3})	Type	μ (cm^2 V^{-1} s^{-1})
S57.I	As grown	1.36×10^{-1}	3.3×10^{16}	N	1390
S57.II	**I.1.** 691/Cd 603(24	1.34×10^{-1}	3.7×10^{16}	N	1242
S57.III	**I.1.** 691/Cd 603(24) **II.1.** 700/Te 600(24)	1.76	3.3×10^{16}	P	106
S56.I	As grown	1.10×10^{8}	7.5×10^{9}	P	68
S56.II	**I.1.** 699/Cd 603(24)	4.70×10^{-2}	9.5×10^{16}	N	1372

3.3.2 Cd Inclusion annealing

Various Cd-annealing configurations are indicated as **I.* Sample Temperature/Cd temperature(delay in hours)** in Tab. 3.1. Samples were annealed at 700 °C for 24 hours below saturated Cd-pressure $P_P^{Cd} \approx 10^{-0.97}$ atm, which corresponds to temperature of Cd, 600 °C. The ampoule was heated by 2 °C min^{-1} rate and cooled slowly by 1 °C min^{-1} rate. The same heating and cooling rates were used at all annealing experiments. The illustration of Cd-annealing profile can be seen in Fig. 3.6.

After Cd-annealing, all samples were polished again, chemo-mechanically polished and etched to remove the thin surface layer damaged by annealing. Consequently, the samples were again electrically and optically characterized as mentioned above. Unfortunately, it was technically complicated to find repeatedly exactly the same position after each annealing step. Therefore, only typical images were used for the evaluation of annealing impact.

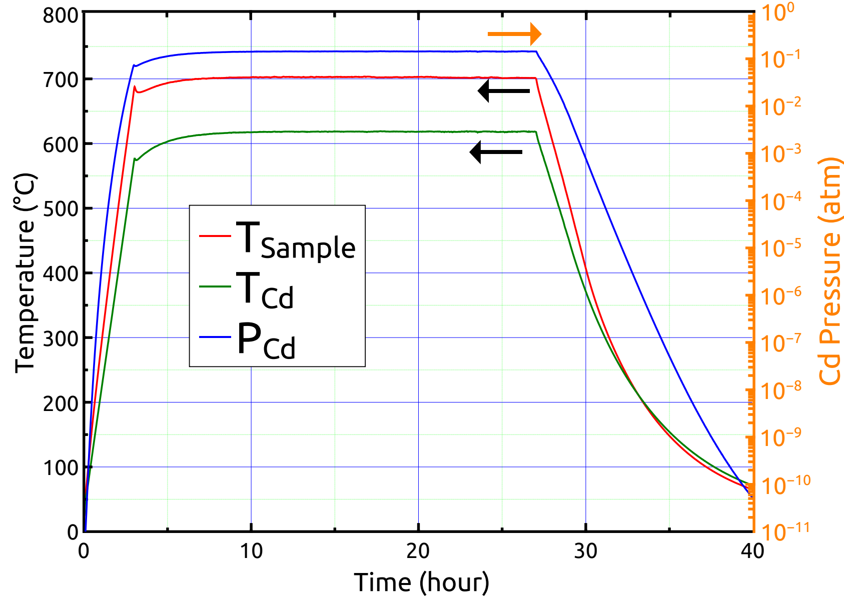

Figure 3.6: Ilustration of Cd-annealing profile. Red and green lines correspond to sample and Cd temperature, respectively. The blue line corresponds to Cd-pressure.

As-grown samples from crystal **S57** contain six-pointed star-like inclusion with approximately 25 µm diameter, see Fig. 3.7a and Fig. 3.7b, respectively. Similar defects were observed by Brion[53], who proved the dependency of defects‘ size and intensity of illumination. Later on, they were identified as a Cd inclusion[25,37].

Cd-inclusion density and size significantly decreased after Cd-annealing however the inclusion was not destroyed completely and some seeds remained, see Fig. 3.7c, Fig. 3.7d, respectively.

Although Cd inclusions are made from Cd atoms only and should stay stable at Cd-annealing, applied Cd-pressure, $P_P^{Cd} \approx 10^{-0.97}$ atm ($T_{Cd} = 600\,°\text{C}$), is significantly lower than saturated Cd-pressure, see Fig. 2.3 and chemical diffusion of Cd is at 700 °C high enough, so Cd from inclusion could sublimate. This assumption is supported by presence of residual voids, which are visible after Cd-annealing. These residual voids correspond to lattice stress around of former Cd inclusion. We found that the low value of the resistivity and the n-type conductivity, see Tab. 3.1, were not practically changed after Cd-annealing. We can explain this fact by the existence of dominant Cd_I donors in as-grown and Cd-rich annealed samples.

Sub-sequential Te-annealing condition are indicated as **II.* Sample Temperature/Te temperature(delay in hours)** in Tab. 3.1. During second step, the samples were annealed at 700 °C for 24 hours at saturated Te-overpressure, which correspond to temperature $T_{Te} = 600\,°\text{C}$. After Te-annealing, the size and concentration of seeds slightly decreased again, see Fig. 3.7e and Fig. 3.7f, which corresponds to a small reconstruction of crystal lattice. Sample resistivity increased a little bit $\rho \sim 1\,\Omega\,\text{cm}$, and the type of conductivity was changed to p-type.

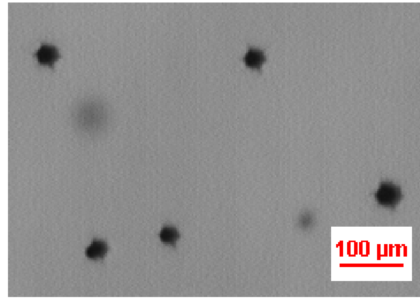

(a) before annealing (4× magnitude)

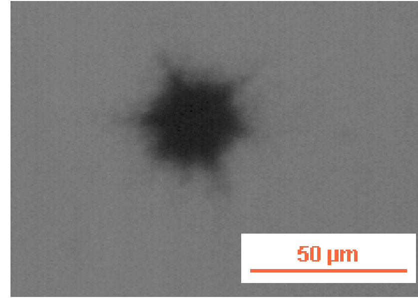

(b) before annealing (20× magnitude)

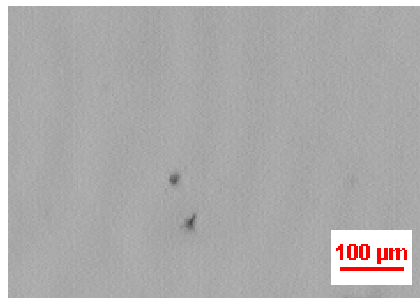

(c) after annealing at Cd overpressure (4× magnitude)

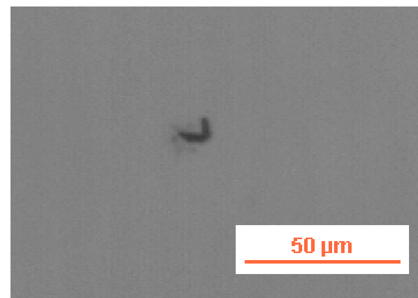

(d) after annealing at Cd overpressure (20× magnitude)

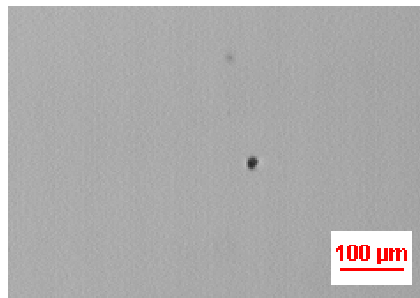

(e) after annealing at Cd overpressure followed by annealing at Te overpressure (4× magnitude)

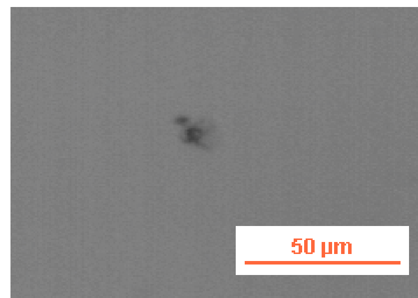

(f) after annealing at Cd overpressure followed by annealing at Te overpressure (20× magnitude)

Figure 3.7: Infrared image of Cd inclusions at samples from crystal **S57** before and after annealing at Cd-pressure followed by annealing at Te-pressure.

3.3.3 Te Inclusion annealing

Samples from **S56** crystal contain triangle and hexagonal inclusions with approximately 25 µm diameter, see Fig. 3.8a and Fig. 3.8b, respectively. They were identified as Te inclusions[25,37].

Samples were annealed at 700 °C at saturated Cd-overpressure for 24 hours, which corresponds to temperature $T_{Cd} = 600$ °C and in Tab. 3.1, it is indicated as Cd 700/600(24). The ampoule was heated by 2 °C min^{-1} rate and cooled slowly by 1 °C min^{-1} rate.

After Cd-annealing, inclusion density and size significantly decreased, see Fig. 3.8c and Fig. 3.8d, respectively.

The resistivity of the sample significantly decreased, $\rho \sim 1 \times 10^{-2}\,\Omega\,\text{cm}$, and the type of conductivity was changed.

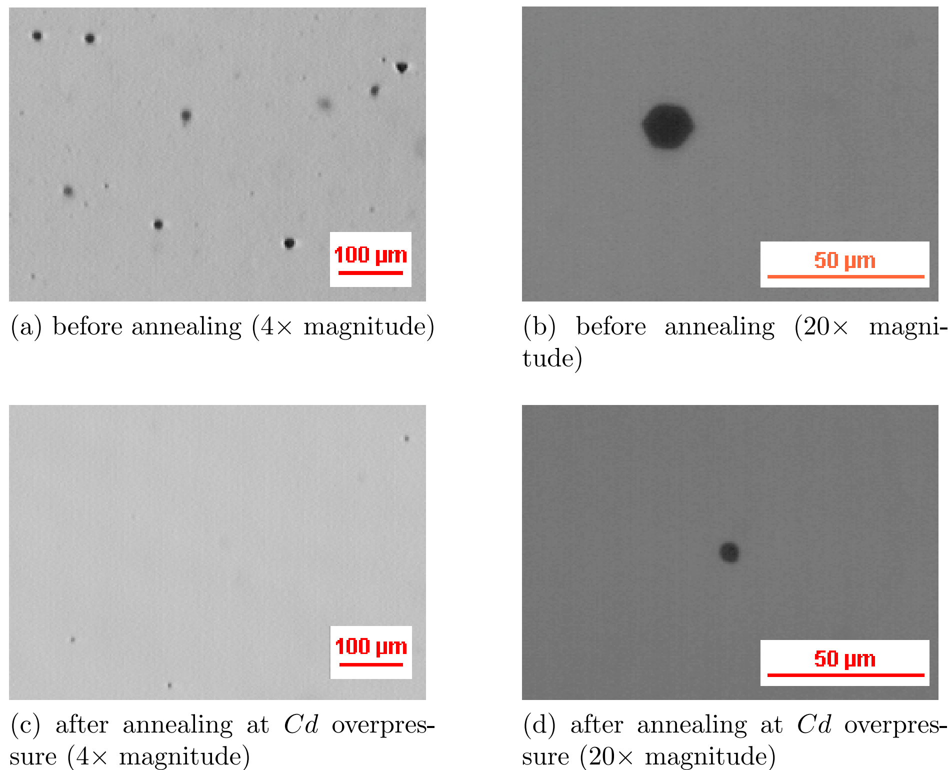

(a) before annealing (4× magnitude)

(b) before annealing (20× magnitude)

(c) after annealing at Cd overpressure (4× magnitude)

(d) after annealing at Cd overpressure (20× magnitude)

Figure 3.8: Infrared image of Te inclusions at **S56** $CdTe:Cl$ after annealing at Cd overpressure.

3.4 Conclusion

In this chapter, we presented a successful technique for the elimination of both tellurium and cadmium inclusions. We have shown that this technique cannot be used to produce high resistive material. Because we used the annealing at saturated overpressures, where the important concentration of Cd_I or V_{Cd} is created. To prepare the high resistive material, we have to use annealing conditions causing self-compensation of all native defects. The defect compensation will be investigated in the following chapter 4.

4. High resistivity restoration

4.1 Introduction

The successful method for inclusion elimination was introduced in the previous chapter 3. However, such a thermal treatment leads to a significant decrease of the material resistivity and to the loss of its detection ability. It proves that finding effective methods for reaching high resistivity after inclusion elimination is highly desired. As discussed in section 4.3, a semiconductor's resistivity is directly determined by the point defect structures. Several possible approaches to reaching high resistivity were discussed in the subsection 2.6.2.

In the case of $CdTe : Cl$ introducing additional deep defects for preserving high resistivity seems to be inappropriate because deep defects are simultaneously trapping centers, which significantly decrease the crystal's detection ability.[75] Hence, shallow defect tuning by post grow annealing seems to be only one reasonable option.

The Te-annealing of $CdTe : In$ with a focus on high resistivity restoration was studied by Belas[47], where the effect of In concentration was investigated. Study of dependence $CdTe : Cl$ electrical properties on chlorine doping was conducted by Ohmori[76]. First detailed study of $CdTe : Cl$ annealing was presented by Ayoub[77,78], who focused on an annealing at vacuum, argon and $CdCl_2$. Detailed discussion for annealing of $CdTe : Cl$ at Te-overpressure were lead by Franc[69] and mainly by Bugár[79]. However, Franc used two commercial Acrorad (Japan) samples, where the original chlorine concentration was unknown. Bugár was focused only on samples with high Cl concentration. They revealed a high resistivity caused by using a consequent Te-annealing with two temperature levels, thus pressure plateau, which has led to shallow point defects compensation. This chapter will analyze the phenomenon of shallow defects compensation in detail.

The Cd- and Te-annealing conditions with multiple temperature and pressure steps resulting in the preparation of the high resistivity $CdTe : Cl$ with low chlorine doping are investigated after elimination of inclusions and precipitates. Multiple-step annealing aims to homogenize the sample's defect structure in the first step before reaching the high-resistivity annealing conditions afterward. The dominant role of the Cl doping concentration for the preparation of high resistive material relative to other crystal properties is manifested.

4.2 Experiment

Similarly to chapter 3, we used two-step annealing for the high resistivity restoration experiments and the Hall effect measurement for characterization of electrical properties of as-grown and annealed samples. The doping level of Cl was established by measuring the carrier concentration of samples annealed in Cd saturated vapor pressure, in which the donor was the dominant point defect[67,74].

On the contrary to the chapter 3, annealing under Cd overpressure with various steps,

step durations and Cd pressures, which were defined by the temperature of Cd, were introduced to the annealing procedure. Annealing conditions are indicated for each step (*) individually as **I.* Sample Temperature/Cd temperature(delay in hours)** in Tab. 4.1–4.2.

The sub-sequential two-step annealing under Te overpressure with various step durations and Te pressures, which were defined by temperature of Te, were introduced to annealing procedure after Cd-annealing. Similar to Cd-annealing, various annealing conditions are indicated in Tab. 4.1–4.2 as **II.* Sample Temperature/Te temperature(delay in hours)** for each temperature step separately, see illustration of two-step Te annealing profile at Fig. 4.1.

The ampoule was heated by 2 °C min^{-1} rate and usually cooled slowly by 1 °C min^{-1} rate to a defined temperate step or to a room temperature.

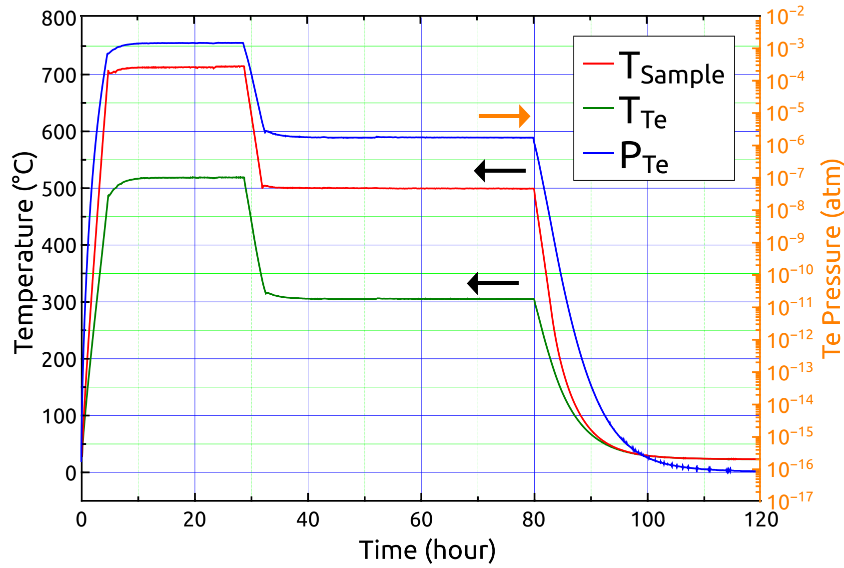

Figure 4.1: Ilustration of Te-annealing two steps profile. Red and green lines correspond to sample and Te temperature, respectively. The blue line corresponds to Te-pressure.

4.2.1 Samples for resistivity restoration study

The 2 crystals of $CdTe$ doped by chlorine ($CdTe : Cl$), **S56** and **S57**, were grown by Vertical Gradient Freeze (VGF)[36,73] method, where the concentration of added chlorine was $[Cl]_{Added} \sim 1 \times 10^{18}\,\mathrm{cm}^{-3}$.

Samples were cut from the single crystalline part of the ingot, polished and etched, see sample preparation section A.2 at the appendix, to final dimensions $5 \times 5 \times 2$ mm^3.

Although both crystals, **S56**, **S57** were grown with the exact chlorine dopping and the furnace was set to the same setting, the actual growing condition was slightly different.

Therefore, both crystal series contain a different concentration of electrically active chlorine and a different type of inclusion.

Chlorine concentration for each individual **S56** and **S57** sample was established as $[Cl]_{S57}/[Cl]_{S56} \in (3.1 \times 10^{16} - 9.7 \times 10^{16}\,\mathrm{cm}^{-3})$. Both crystal series were characterized by Van der Pauw hall measurement. Once grown, **S56** exhibits a high resistivity $\rho \sim 1 \times 10^{8}\,\Omega\,\mathrm{cm}$, P-type of conductivity. On the other side, once grown, **S57** exhibits a low resistivity $\rho \sim 0.1\,\Omega\,\mathrm{cm}$ and N-type of conductivity. The overview of electrical properties is presented in the Tab. 4.1.

4.3 Results and Discussion

Annealing experiments were performed on a large set of $CdTe : Cl$ samples. In total, 50 annealing experiments were performed, 14 samples were annealed repetitively to get information on the same sample. Tab. 4.1 and Tab. 4.2 contains sub-set of multiple-step annealing with various temperature and Cd or Te pressure steps for **S57** and **S56** crystals only with known chlorine concentration, respectively. Corresponding initial chlorine concentration together with sample galvanometric properties after whole annealing treatment are indicated in that tables. Similarly, as it was discussed in section 3.3.1, Tabs. 4.1–4.2 present free carrier mobility higher than theoretical electron/hole mobility of ideal crystal. However, this chapter focuses on high resistivity restoration, which is not related to precise mobility establishment; therefore, mentioned mobilities are only indicative.

Crystal point defect's theory presented in the chapter assume, that native defect concentration is given by thermodynamic equilibrium between solid CdTe in non-stoichiometric ambient gas Cd/Te. Hence, the resulting sample's resistivity should be given only by the last annealing step if the sample reaches the thermodynamic equilibrium. This assumption is directly supported by two independent measurements of S57.VIII for which only the last step of the annealing scheme was changed, see Tab. 4.1. This change results in not only different sample's resistivity but also in change of n-type to p-type of conductivity. Therefore, a high resistivity mode was reachable by the setting of $Te-$annealing condition, where the most critical parameter was the temperature of the second Te-annealing step.

Crystals were annealed at high Te pressure and if they have shown signs of conductivity type changes, usually from n-type to p-type, we expect that high resistivity mode is in the middle between the low and high Te pressure. We name this approach the Interval bisection method in the following text. Although it was a very lengthy process, the high resistivity configuration was reached many times.

Annealing conditions resulting in high-resistivity samples were very sample-sensitive, as can be seen, for example, when comparing the $S57.III$ and $S56.IV$ or $S57.VIII$ and $S56.VI$, which had been treated under similar annealing conditions but have shown significantly different resistivity; or comparing $S57.V$ with $S56.III$, which were annealed differently but exhibited similar resistivity.

Table 4.1: The overview of electrical properties of $CdTe : Cl$ samples from crystal $S57$ before and after Cd- and Te-annealing

$[Cl]$ (cm^{-3})	Sample	Annealing condition	ρ_{Hall} (Ω cm)	n/p (cm^{-3})	Type	μ ($cm^2 V^{-1} s^{-1}$)
	S57.I	As grown	1.36×10^{-1}	3.3×10^{16}	N	1390
	S57.II	**I.1.** 691/Cd 603(24)	1.34×10^{-1}	3.7×10^{16}	N	1242
3.1×10^{16}	S57.III	**I.1.** 698/Cd 419(24) **I.2.** 502/Te 420(24) **II.1.** 723/Te 527(24) **II.2.** 499/Te 312(120)	3.22×10^{7}	3.0×10^{8}	N	673
3.4×10^{16}	S57.IV	**I.1.** 804/Cd 744(15) **I.2.** 502/Cd 454(48) **II.1.** 697/Te 504(24) **II.2.** 496/Te 306(48)	1.16×10^{2}	6.3×10^{13}	N	884
3.4×10^{16}	S57.V	**I.1.** 698/Cd 419(24) **I.2.** 502/Cd 420(24) **II.1.** 723/Te 527(24) **II.2.** 499/Te 312(120)	3.25×10^{8}	2.7×10^{7}	N	745
3.4×10^{16}	S57.IV	**I.1.** 804/Cd 744(15) **I.2.** 502/Cd 454(48) **II.1.** 695/Te 509(24) **II.2.** 495/Te 343(48)	4.61×10^{5}	–	P/N	–
3.4×10^{16}	S57.VI	**I.1.** 691/Cd 603 (24) **II.1.** 699/Te 612(24) **II.2.** 503/Te 345(48)	8.45×10^{4}	2.8×10^{12}	P	130
3.4×10^{16}	S57.VII	**I.1.** 691/Cd 603 (24) **II.1.** 692/Te 536(24) **II.2.** 483/Te 345(48)	3.02×10^{2}	1.6×10^{14}	P	130
3.4×10^{16}	S57.VII	**I.1.** 691/Cd 603 (24) **II.1.** 699/Te 612(24) **II.2.** 503/Te 345(48)	4.81×10^{3}	1.5×10^{13}	P	100
3.6×10^{16}	S57.VIII	**I.1.** 804/Cd 744(15) **I.2.** 502/Cd 454(48) **II.1.** 697/Te 504(24) **II.2.** 496/Te 306(48)	2.63×10^{1}	2.1×10^{14}	N	1109
3.6×10^{16}	S57.IX	**I.1.** 691/Cd 603 (24) **II.1.** 700/Te 600(24) **II.2.** 500/Te 330(48)	5.61×10^{7}	1.5×10^{8}	N	1051
3.6×10^{16}	S57.VIII	**I.1.** 804/Cd 744(15) **I.2.** 502/Cd 454(48) **II.1.** 695/Te 509(24) **II.2.** 495/Te 343(48)	1.43×10^{3}	4.3×10^{13}	P	101
4.3×10^{16}	S57.X	**I.1.** 795/Cd 749(24) **I.2.** 502/Cd 462(48) **II.1.** 699/Te 504(24) **II.2.** 503/Te 327(96)	1.98×10^{8}	–	P/N	–
5.1×10^{16}	S57.XI	**I.1.** 795/Cd 749(24) **I.2.** 502/Cd 462(48) **II.1.** 699/Te 504(24) **II.2.** 503/Te 327(96)	4.03×10^{7}	–	P/N	–
6.3×10^{16}	S57.XII	**I.1.** 795/Cd 749(24) **I.2.** 502/Cd 462(48) **II.1.** 699/Te 504(24) **II.2.** 503/Te 327(96)	5.88×10^{6}	–	P/N	–

Table 4.2: The overview of electrical properties of $CdTe : Cl$ samples from crystal $S56$ before and after Cd- and Te-annealing

$[Cl]$ (cm^{-3})	Sample	Annealing condition	ρ_{Hall} (Ω cm)	n/p (cm^{-3})	Type	μ (cm^{2} V^{-1} s^{-1})
	S56.I	As grown	1.1×10^{8}	7.5×10^{9}	P	68
	S56.II	**I.1.** 699/Cd 603(24)	4.7×10^{-2}	9.5×10^{16}	N	1372
9.7×10^{16}	S56.III	**I.1.** 804/Cd 744(15) **I.2.** 502/Cd 454(48) **II.1.** 697/Te 504(24) **II.2.** 496/Te 306(48)	8.43	6.0×10^{14}	N	1233
9.7×10^{16}	S56.IV	**I.1.** 689/Cd 599 (48) **II.1.** 699/Te 507(24) **II.2.** 499/Te 315(48)	9.77	5.5×10^{13}	N	1063
9.7×10^{16}	S56.IV	**I.1.** 689/Cd 599 (48) **II.1.** 700/Te 500(24) **II.2.** 502/Te 330(48)	4.70×10^{1}	1.1×10^{14}	N	1060
9.7×10^{16}	S56.V	**I.1.** 689/Cd 599 (48) **II.1.** 700/Te 500(24) **II.2.** 500/Te 330(48)	1.75×10^{2}	6.4×10^{13}	N	630
9.7×10^{16}	S56.VI	**I.1.** 804/Cd 744(15) **I.2.** 502/Cd 454(48) **II.1.** 695/Te 509(24) **II.2.** 495/Te 343(48)	2.68×10^{7}	–	P/N	–
9.7×10^{16}	S56.III	**I.1.** 804/Cd 744(15) **I.2.** 502/Cd 454(48) **II.1.** 695/Te 509(24) **II.2.** 495/Te 343(48)	2.45×10^{8}	–	P/N	–

The dependence of sample resistivity on Te-pressure defined by the last annealing steps is plotted to Fig. 4.2 together with conductivity type indication marked as N or P. In the case of high resistivity samples, the conductivity type is unresolved, therefore they are marked as P/N. The original chlorine concentration was measured with high precision before Te-annealing and based on it, the dataset is sorted out into several groups.

The detailed analysis of Fig. 4.2 leads to several important conclusions:

1. Comparing the annealing parameter, the Te pressure of the second step at subsequential Te-annealing was a predominant parameter for reaching a high resistivity. It corresponds to the theoretical subsection 2.6.2, which was published by Grill[45,46,80], where the final conductivity state is set only by an actual point defects structure. Individual defects are compensated through equation of electrical neutrality 2.7a. The major donor represented by Cl_{Te}^{+} is compensated by native acceptors, Cd vacancies either separately V_{Cd}^{2-} or as a part of A-centres $\left(V_{Cd}^{2-} + Cl_{Te}^{+}\right)^{-}$.

2. Previous assumption is evidently valid only for the stationary state, where the sample temperature is high enough, time-delay is long enough, and cooling rate is slow enough to point defects reach a state defined by Te-overpressure and preserved during cooling. This type of experiment cannot decide what long and slow enough mean;

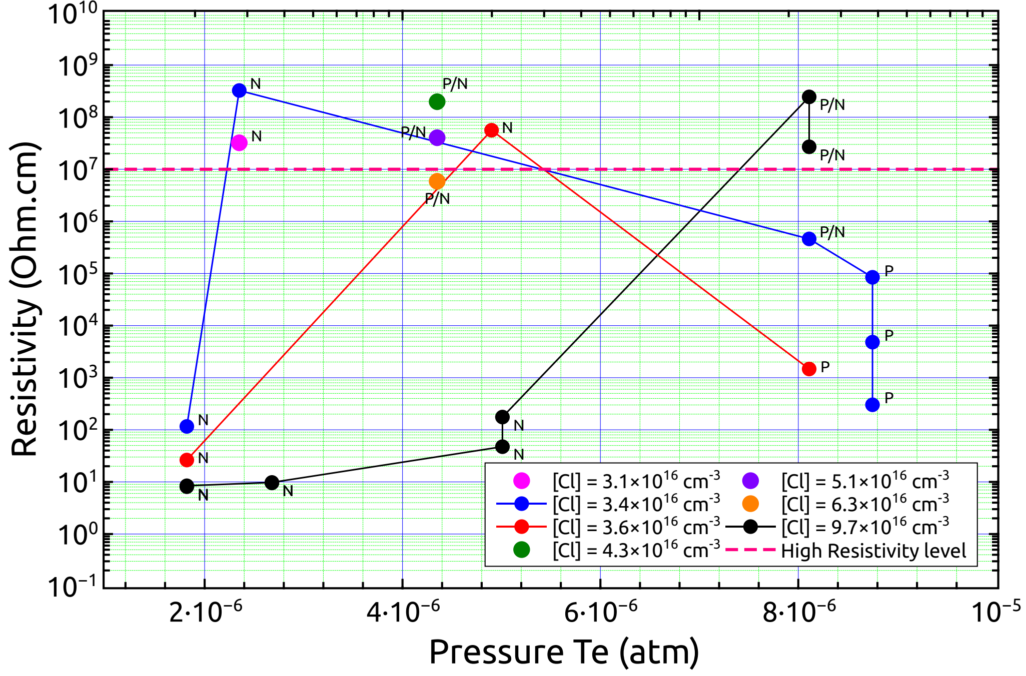

Figure 4.2: Dependence of the sample resistivity on Te-pressure of the second step during the sub-sequential Te-annealing. Conductivity type is marked as N or P. In the case of high resistivity samples, the conductivity type is unresolved; therefore, they are marked as P/N. Based on the original chlorine concentration dataset is sorted out into several groups.

new "in-situ" high-temperature Hall effect measurements would need to be done for a deeper understanding of chemical diffusion.

3. Inspecting results of annealing done on sample sets with known $[Cl]$, we see that low resistivity n-types/p-types are obtained at the lower/larger P_{Te}, which is consistent with the model of considered defect structure. High resistivity annealing condition could be found by interval bisection method.

4. Increased $[Cl]$ yields in increased P_{Te}, at which the high resistivity is obtained. In addition, the necessity to set Te-pressure precisely decreases with increasing chlorine doping, so the region of possible annealing conditions leading to high resistivity increases.

   This is caused due to an increasing influence of an electrically neutral reservoir of Cl, mentioned at point 5, with chlorine concentration.

5. The dependency of sample resistivity on Te-pressure and Cl doping were proved, which is contradictory to Bugár observation[79], who reported weak resistivity sensitivity to Te pressure. His measurement was performed on samples with a little bit higher chlorine dopping, $[Cl]_{Bugar} \approx (3.4 \times 10^{16}, 2.4 \times 10^{17})\,\mathrm{cm}^{-3}$ at significantly

higher Te-pressure and finally only one Te-annealing step was used for his experiment.

Bugár introduced two possible explanations for his unexpected results. (a) Due to unstable conditions during annealing, the pressure of Te and Cd gas around his sample is not precisely defined and some flux of both components has occurred, which complicates the situation even more. (b) During the cooling procedure, the chemical diffusion is high enough to reset point defects structure dynamically and dynamical compensate chlorine donors by native acceptors. However, Bugár could not decide which theory was valid.

Bugár's first theory (a) is declined by my measurement, where the dependency of resistivity on Te-overpressure occurred and no sublimation was observed. In addition, the mentioned *in-situ* high-temperature Hall effect measurements were carried out for $CdTe : Cl$; its resulting dependency on Cd-pressure is discussed in detail in chapters 5 and 6.

The second Bugár's theory (b) seems to be more reliable. Our result supported it because using the second Te-annealing step at a lower temperature, 700 °C, should slow down the dynamics of such a compensation process due to low chemical diffusion and dependency of high resistivity on Te-pressure should occur, which exactly correspond with our experimental results.

Therefore, if this theory is valid, crystals have to contain an electrically neutral source of point defects, possibly V_{Cd}, which dynamically contribute to electrical compensation during cooling. The existence of this neutral reservoir was proved by *in-situ* high-temperature Hall effect measurements, which are discussed in detail in the following chapters 5 and 6.

All conclusions mentioned above explain why the dependency of sample resistivity on Te-pressure and Cl doping were observed.

6. Since the annealing conditions are very sensitive to the minimal change of Cl doping, the detailed characterization of chlorine concentration is necessary before the annealing procedure can start.

4.4 Conclusion

The usable interval bisection method for reaching a high resistivity state using post-grown annealing was presented in this chapter. The connection between high resistivity state, chlorine dopping and Te-pressure was proved and a deeper analysis of this observation was presented. The two steps Te-annealing profile was successfully used to suppress the influence of an electrically neutral temperature-activated reservoir of donors.

However, precise "in-situ" high-temperature Hall effect measurements need to be done for reaching a deeper understanding of chemical diffusion, which seems to be an essential parameter for setting proper annealing conditions.

5. *In-Situ* galvanomagnetic measurement

5.1 Introduction

The successful method for high resistivity restoration was introduced in the previous chapter 4, where the second step of sub-sequential $Te-$annealing was revealed as a practical approach for the precious definition of point defects structure after inclusion elimination by $Cd-$annealing.

However, many questions remain unanswered. A very crucial one is whether there is and if yes, then what is the unidentified temperature activating reservoir of electrical neutral chlorine, which consequently releases chlorine during cooling and dynamically contributes $\mathrm{Cl}_{\mathrm{Te}}^{+}$ to electrical compensation.

In order to answer this question, the *in-situ* galvanomagnetic measurement technique was used. This method enables measurement of galvanomagnetic properties such as electrical conductivity, free carriers concentration and its mobility during annealing process. This technique was used by Zanio[81] and Grill[82] for undoped CdTe, Rud[83,84] presented measurement for CdTe doped by Cu and In, Bugár[79] for $CdTe:Cl$ with middle chlorine concentration,$[Cl]_{Bugar} \approx (3.4 \times 10^{16}, 2.4 \times 10^{17}\,\mathrm{cm}^{-3})$, and Grill[85] for $CdTe:Cl$ with high chlorine concentration, $[Cl]_{Grill} \approx 5 \times 10^{18}\,\mathrm{cm}^{-3}$.

In this chapter, detailed *in-situ* measurement of galvanomagnetic properties in dependence on Cd overpressure will be discussed for $CdTe:Cl$ samples with low chlorine dopping, $[Cl] \approx 4.3 \times 10^{16}\,\mathrm{cm}^{-3}$

5.2 Experimental technique

The high-temperature *in-situ* measurement of the electrical conductivity was performed using a classical six probe Hall bar configuration, see section 3.2.4.

The Cl-doped CdTe (CdTe : Cl) single crystal grown by the vertical gradient freeze method[70], **S57**, with $[\mathrm{Cl}] \approx 4.3 \times 10^{16}\ \mathrm{cm}^{-3}$ was used for measurement. Samples dimensions were $3.7 \times 2.9 \times 6.8\ \mathrm{mm}^3$. The chlorine concentration in the samples was established as a concentration of free carriers evaluated by Hall effect measurement on the samples after Cd-rich annealing, where most of Cl atoms are assumed to form substitutional shallow donors[67,74]. The tungsten wires were welded into the sample whereas no sample holder was needed since tungsten wires fixed the sample inside the ampoule[85].

Thanks to this configuration, we can anneal sample and parallelly "in situ" measure galwanomagnetic properties of the sample. The sample was placed with the cadmium source in a cleaned quartz ampoule and sealed. The detailed description of the sample and ampoule preparation is presented in appendix A.1 and A.5.

Measurement was performed in a two-zone furnace, where one zone controlled the sample temperature and the other one the Cd partial pressure P_{Cd}. The schema of an experimental setup can be seen in Fig. 5.1.

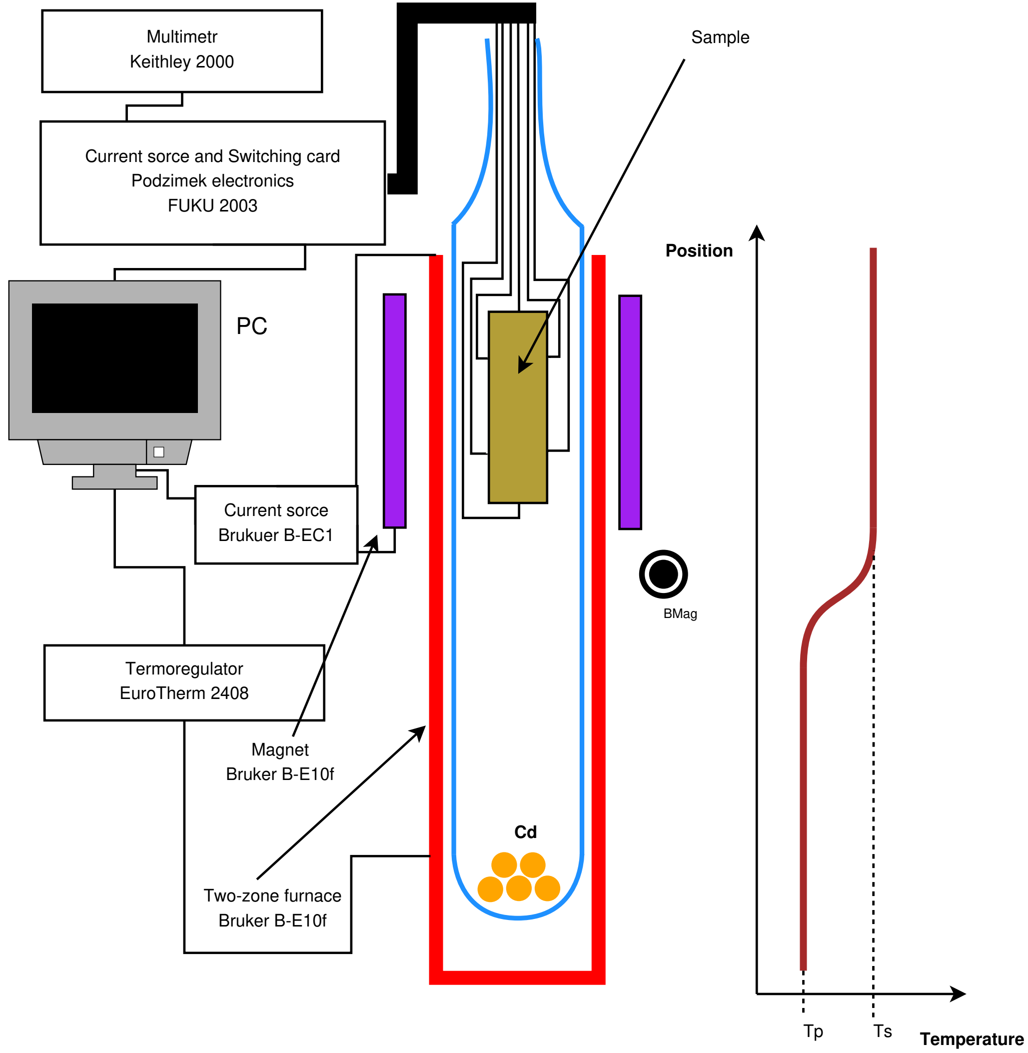

Figure 5.1: Scheme of experimental setup for "in situ" Hall effect measurement simultaneously with annealing.

Sample width was 3.7 mm. The infrared image of the sample with welded tungsten wire was achieved using an infra-red microscopy, see Fig. 5.2. The grey area is the sample, the white area is a sample's surroundings and the opaque area corresponds to the area with a highly corrupted crystal lattice. The depth of both highly corrupted crystal lattice areas was measured as 0.555 mm.

However, the reduction of sample width occurred due to welded wires, the experimentally measured Hall voltage U_H^{Exp} has to be corrected to U_H^{Real} as

$$U_H^{Real} = kU_H^{Exp}, \tag{5.1}$$

where k is a correction factor, which depends on proportion of sample width t, to visible

depth d, of wires welding as

$$k = \frac{t}{f \cdot d}, \qquad (5.2)$$

where f is a multiplication factor which represents a conductivity difference between an unaffected sample and a conductive channel created by welded wires.

Unfortunately, the infra-red microscopy can measure only highly damaged crystal lattice, while k-factor is sensitive to depth $(f \cdot d)$ of the conductive channel, which is under welded wires and its conductive difference with the unaffected sample. Its depth is undoubtedly higher than this visible area. As a first approximation, the depth of these conductive channels was estimated as a double $f = 2$ of highly damaged area under contacts. The correction factor $k \approx 1.71$ was established for each temperature region using this approximation.

The influence of conductive channels, f, decreases with an increasing sample temperature analogically as the conductivity decreases between the conductive channel and the rest of the sample.

The electrical conductivity σ measurement has not been corrected. The σ is calculated as a ratio of voltage measured along samples and applied as current, therefore assuming similar damage of current and voltage contact; the affection of calculated value is insignificant. Additionally, sample length was 6.8 mm, which is significantly higher than the volume of wires welded; therefore the effect of voltage correction is insignificant as well.

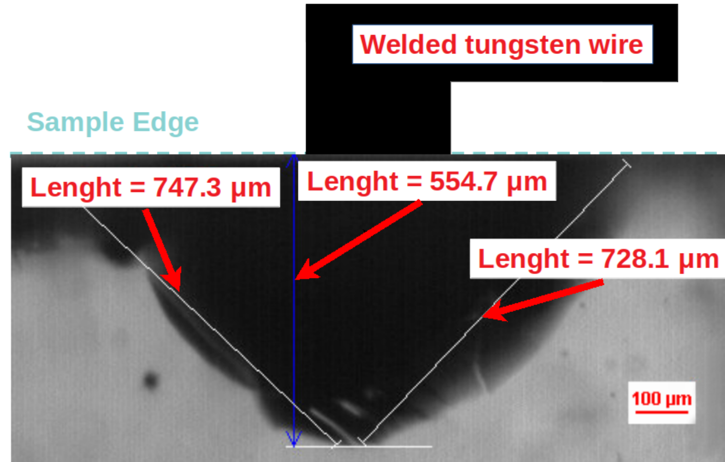

Figure 5.2: Infrared microscopy detail image of one tungsten wire welded into the sample. The area destroyed by welding is opaque for infrared light.

The measurement was performed at defined sample temperature T_S simultaneously with multiple different step-like changes of Cd temperature, which directly define Cd partial pressure P_{Cd}. The typical raw data of electrical conductivity are presented in Fig. 5.3. The σ_0 represents conductivity before step-change of P_{Cd} and σ_∞ represents an ideal

equilibrium value after infinity time after change. For example the Cd-temperature was changed from $T_{Cd}^{Original} = 480\,°C$ to $T_{Cd}^{New} = 520\,°C$ corresponding to step-like change of $\Delta P_{Cd} \approx 15 \times 10^{-3}$ atm at time 351 h. One can see the relaxation of conductivity with reach equilibrium value σ_∞.

Free carrier's concentration and mobility measurement raw data look similar.

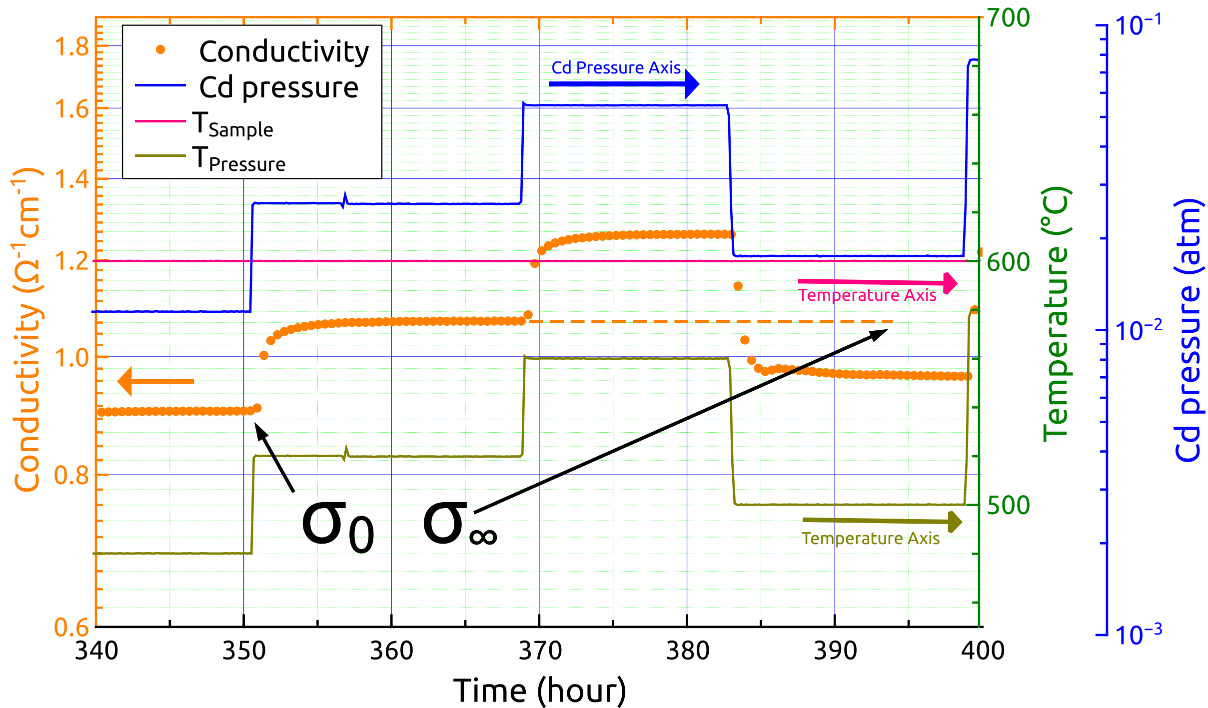

Figure 5.3: Typical electrical conductivity profile after step-like P_{Cd} changes. Pink, olive and blue lines represent sample temperature, Cd temperature and Cd partial pressure P_{Cd}, respectively. The σ_0 represents conductivity before change of P_{Cd} and σ_∞ represent an ideal equilibrium value after infinity time.

5.3 Results and Discussion

After the step-wise change of Cd pressure, the new equilibrium of electrical conductivity σ_∞ was evaluated when measured values fluctuated lower than expected precision.

The dependency of final electrical conductivity σ_∞ on final Cd pressure at sample temperatures 600 °C, 700 °C and 800 °C is presented at Fig. 5.4. The full dot represents experimental data, together with double dot-dashed lines, which correspond to the theoretical model presented by Grill[86] for undoped CdTe.

The dotted, dashed and dash-and-dot lines are theoretical data for CdTe:Cl calculated based on Grill[85] extended by introducing neutral complex of defects, which contained

singly ionized A-center, $\left(V_{Cd}^{2-} + Cl_{Te}^{+}\right)^{-}$, combined with Cl_{Te}^{+} nearby. The assumed chlorine doping concentrations were 2×10^{16}, 4×10^{16} and 1×10^{17} cm^{-3}, respectively. Introduced neutral defect was named as $\left(V_{Cd}^{2-} + 2Cl_{Te}^{+}\right)^{0}$.

The theoretical model Grill[85] extended by $\left(V_{Cd}^{2-} + 2Cl_{Te}^{+}\right)^{0}$ for CdTe:Cl was calculated using properties of native point defects, which were taken from undoped CdTe[87]. The density of $(\mathrm{V_{Cd}2Cl_{Te}})$ was calculated according Höschl[88] as

$$\left[\left(\mathrm{V_{Cd}^{2-}2Cl_{Te}^{+}}\right)^{0}\right] = \frac{3}{2n_0}\left[\left(\mathrm{V_{Cd}^{2-}2Cl_{Te}^{+}}\right)^{-}\right]\left[\mathrm{Cl_{Te}^{+}}\right]\exp\left[\frac{E_c}{k_b T}\right], \quad (5.3)$$

where the fraction $\frac{3}{2}$ represents the ratio of the configuration degeneracies of $(\mathrm{V_{Cd}Cl_{Te}})$ and $(\mathrm{V_{Cd}2Cl_{Te}})$ complexes and the binding energy of the complex $E_c = 0.69$eV was calculated assuming Coulomb forces between charged point defects defining the interaction – doubly ionized negative $\mathrm{V_{Cd}^{2-}}$ and singly ionized positive $\mathrm{Cl_{Te}^{+}}$.

The storage of inactive Cl into similar neutral centers[89] was observed at a reduced temperature lower than 140K and it may be excluded in our analysis performed at the much higher temperature.

Similar analyses were provided for dynamics of free carriers concentration n/p and mobility μ presented in Fig. 5.5 and Fig. 5.6 respectively. Its dependencies on Cd pressure were observed at the same temperature region, 600℃, 700℃ and 800℃.

Since all used models of carriers mobility stay same for high Cd-pressure, see Fig. 5.6, the f-factor was estimated for each temperature independently, see Tab. 5.1.

Table 5.1: The overview of f and k factors as a correction of welded wires.

Temperature ℃	f	k
Temperature independent	2	1.71
600	2.42	1.42
700	2.32	1.48
800	2.15	1.60

The measured points corrected by temperature-independent factor $k = 1.71$ are marked by full dot. We found that using value $k = 1.71$ does not correctly fit measured data at each temperature. Therefore we used individual k factors, which was correcting measured points individually by $k = 1.42$, $k = 1.48$, $k = 1.60$, for 600 °C, 700 °C and 800 °C, respectively, they are marked by empty dot together with same theoretical models as mentioned above.

One can see from Fig. 5.4 – 5.6, that experimental data can not be described properly by Grill's[86] model. Even more complex model[85] extended by neutral complex $\left(V_{Cd}^{2-} + 2Cl_{Te}^{+}\right)^{0}$, containing not only native defects but also chlorine induced defects, is suboptimal.

This insufficient characteristic of both models can be explained either by (a) incorrect parametrization of defects, which are already included in current models or (b) effects of welded wires correction or (c) some defect, which contributes to carrier's compensation not included in current models.

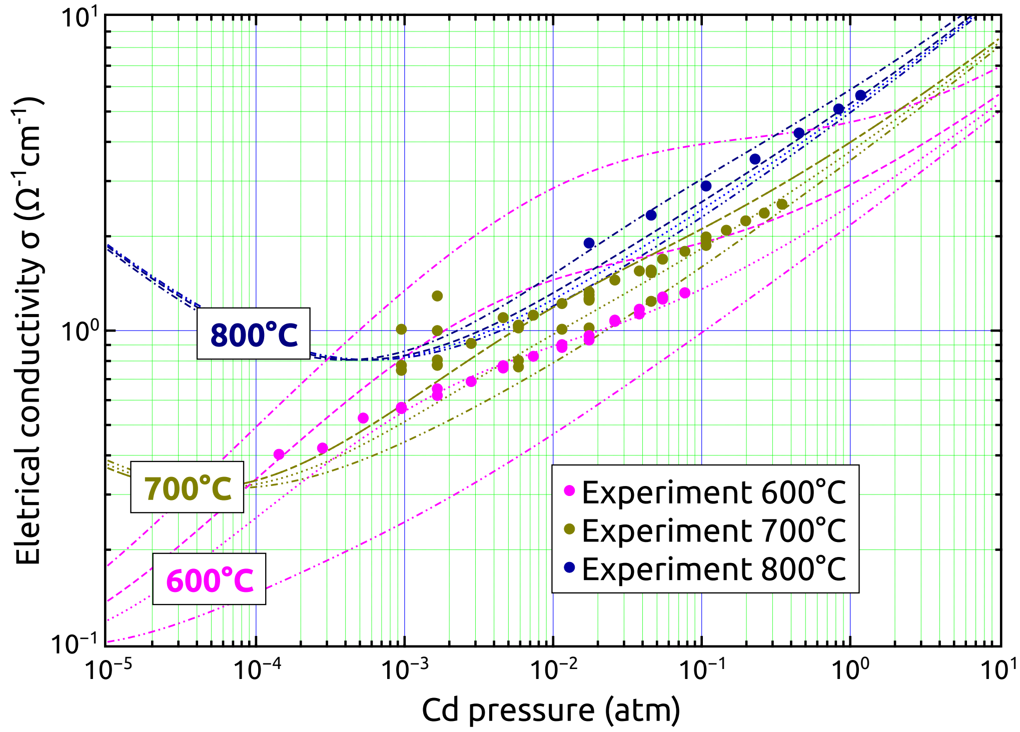

Figure 5.4: Electrical conductivity dependency on Cd pressure measured at 600 °C, 700 °C and 800 °C. The full bullets represent experimental data, together with double dot-dashed lines, which correspond to theoretical model for undoped CdTe presented by Grill[86]. The dotted, dashed and dash-and-dot lines are theoretical data for CdTe:Cl calculated based on Grill[85] extended by $\left(V_{Cd}^{2-} + 2Cl_{Te}^{+}\right)^0$ for 2×10^{16}, 4×10^{16} and 1×10^{17} cm^{-3} chlorine doping, respectively.

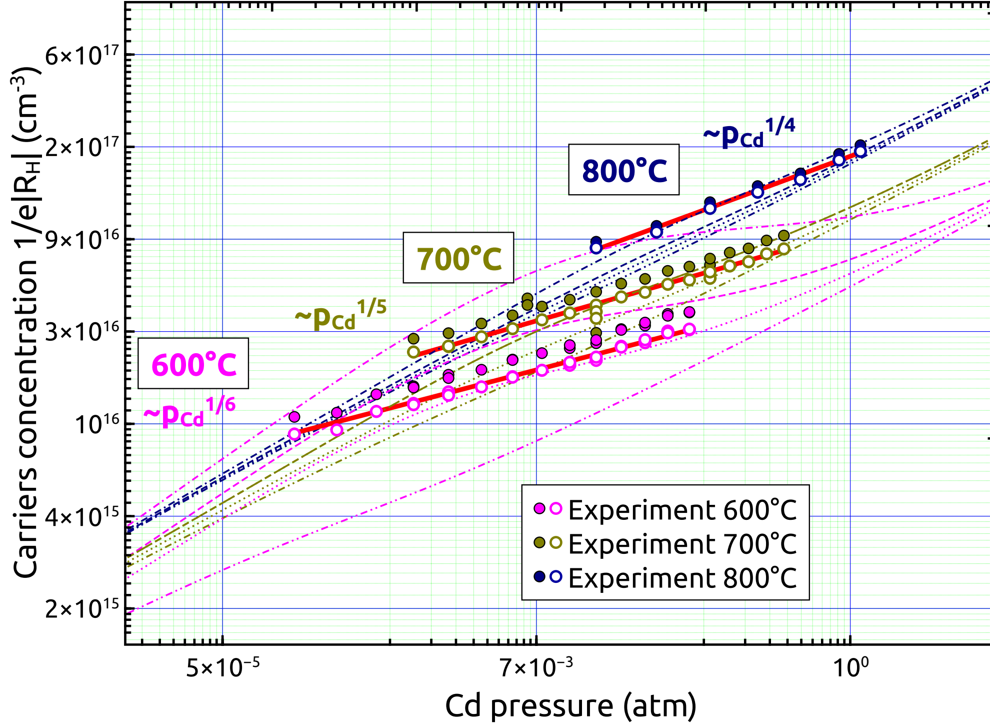

Figure 5.5: Free carriers concentration dependency on Cd pressure measured at 600 °C, 700 °C and 800 °C. The full bullets represent experimental data, corrected by $k = 1.71$ factor, the empty dots represent experimental data corrected individually by $k = 1.42$, $k = 1.48$, $k = 1.60$ for 600 °C, 700 °C and 800 °C, respectively. The red lines represent the linear fits of measured at 600 °C, 700 °C and 800 °C and its slope correspond to pressure dependency of $\sim P_{Cd}^{\frac{1}{6}}$, $\sim P_{Cd}^{\frac{1}{5}}$, $\sim P_{Cd}^{\frac{1}{4}}$, respectively. Double dot-dashed lines correspond to theoretical model for undoped CdTe presented by Grill[86]. The dotted, dashed and dash-and-dot lines are theoretical data for CdTe:Cl calculated based on Grill[85] extended by $\left(V_{Cd}^{2-} + 2Cl_{Te}^{+}\right)^0$ for 2×10^{16}, 4×10^{16} and 1×10^{17} cm^{-3} chlorine doping, respectively.

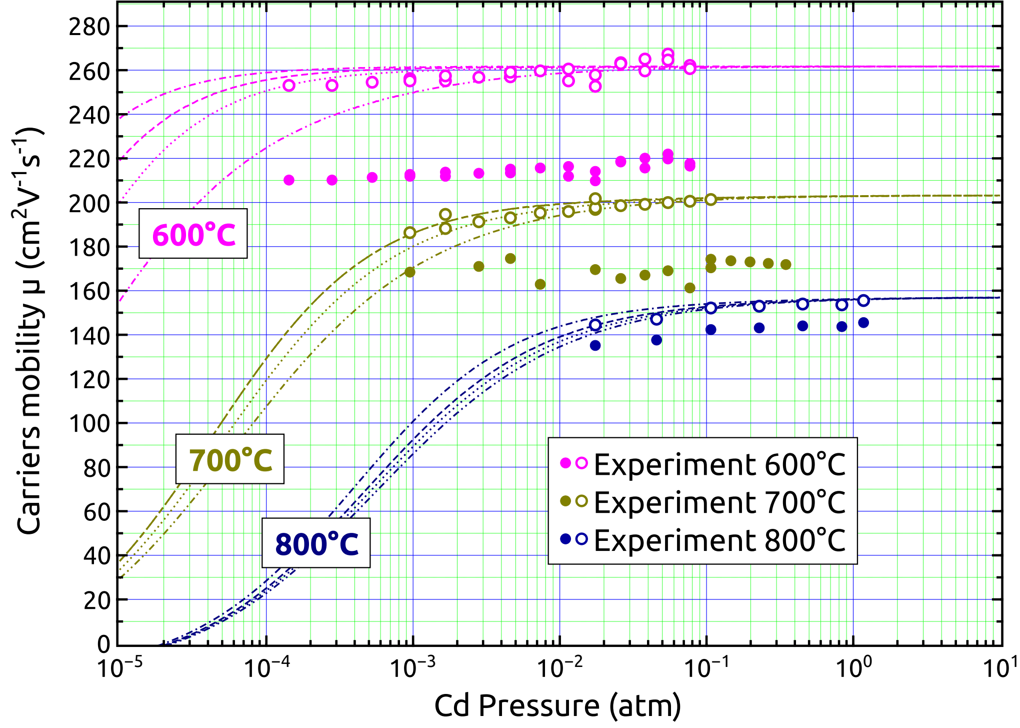

Figure 5.6: Free carriers mobility dependency on Cd pressure measured at 600 °C, 700 °C and 800 °C. The full bullets represent experimental data, corrected by $k = 1.71$ factor, the empty dots represent experimental data corrected individually by $k = 1.42$, $k = 1.48$, $k = 1.60$ for 600 °C, 700 °C and 800 °C, respectively, together with double dot-dashed lines, which correspond to theoretical model for undoped CdTe presented by Grill[86]. The dotted, dashed and dash-and-dot lines are theoretical data for CdTe:Cl calculated based on Grill[85] extended by $\left(V_{Cd}^{2-} + 2Cl_{Te}^{+}\right)^0$ for 2×10^{16}, 4×10^{16} and 1×10^{17} cm^{-3} chlorine doping, respectively.

We are able to decide between these three hypotheses based on the detail analysis of dependency free carrier's concentration on Cd pressure, Fig 5.5.

As a first assumption, let us say that for high Cd pressure, the crystal behavior will be mostly driven by native defect, mainly by cadmium interstitial Cd_I, due to Cd saturation pressure. Validation of such an assumption could be illustrated for $P_{Cd} > 1 \times 10^{-1}$ atm, especially for higher sample temperature at each Fig. 5.4 – 5.6. The theoretical lines for electrical conductivity, free charge concentration and mobility have occurred almost in an identical slope independently of chlorine doping.

The free charge concentration is therefore given as $n \sim P_{Cd}^{\frac{1}{2}}$ in case undoped CdTe as was described in Fig. 5 in [86] by Grill. For highly chlorine doped samples, the free charge concentration is given as $n \sim P_{Cd}^{\frac{1}{3}}$ for high Cd pressure. The point defects structure of high chlorine doped samples is discussed in Figure 3 in [85] by Grill. The experimental data presented in Fig. 5.5, should therefore reach slopes in the interval $\left(\frac{1}{3}; \frac{1}{2}\right)$, however it reveals slopes in the interval $\left(\frac{1}{6}; \frac{1}{4}\right)$. For high Cd pressure, the dependency slope is independent of a model parametrization and correction factor k doesn't affect slope either. Therefore, two hypotheses, (a) incorrect model parametrization and (b) effect of welded wires correction, have to be rejected.

A reasonable explanation of the model's insufficient characteristic seems to be thus the third hypothesis, (c), assuming hidden defect, which is not contained in any theoretical model. Research for this hidden defect will be presented in Chapter 7.

5.4 Conclusion

This chapter introduces an "*in-situ*" galvanomagnetic measurement technique. The dependency of electrical conductivity, free carriers concentration and its mobility on Cd pressure were investigated for 600°C, 700°C and 800°C. The limitation of multiple theoretical models was discussed. All defect models reveal insufficient characteristic, the slope of experimentally measured free carriers concentration reaching $\left(\frac{1}{6}; \frac{1}{4}\right)$ instead of theoretical $\left(\frac{1}{3}; \frac{1}{2}\right)$. It may be explained by an existence of a hidden defect type, which is an electrically neutral, temperature-activated reservoir of donors. The $\left(V_{Cd}^{2-} + 2Cl_{Te}^{+}\right)^0$ was introduced as a promising candidate as this neutral temperature has activated a reservoir of donors. Chapter 7. is dedicated to the detailed research of this hidden defect.

6. Chemical diffusion coefficient

6.1 Introduction

The successful interval bisection method for reaching the high resistivity state using post-grown annealing was presented at Chapter 4. The $\left(V_{Cd}^{2-} + 2Cl_{Te}^{+}\right)^0$ was introduced as a promising candidate since this neutral temperature has activated a reservoir of donors at Chapter 5. However, many questions still remained unanswered. What is an optimal delay during two-step annealing? Which cooling speed needs to be ensured to set up a desired point defects structure? All these questions can be addressed by understanding diffusion in $CdTe$.

Research of atomic diffusion in solids represents one of the fundamental tasks in physics with a straightforward impact on optimization of the annealing process. Diffusion is typically explored in the regime of isoconcentration diffusion at chemical equilibrium using radiotracers, which is known as a self-diffusion (tracer diffusion) and characterized by the self-diffusion coefficient D^* or in a gradient of chemical potential entailing compositional changes, which is called chemical diffusion or interdiffusion being depicted by the chemical diffusion coefficient $\tilde{D}$. The overview of experimental techniques used for measurement of diffusion in semiconductors, results and problems with their interpretation can be found elsewhere[90,91]. Despite long-term research and an extensive effort, there remain fundamental questions around the basic mechanisms of diffusion incurred by an incomplete understanding of defect properties of CdTe and by deficient experimental data. New experiments on well-defined samples are requested.

Chemical diffusion coefficient is routinely measured by the time relaxation of electrical conductivity following up on the step-wise change of ambient component pressure. This method was applied for undoped CdTe by Zanio[81], Grill[82] and Rud[83]. For In- and Cu-doped CdTe the diffusion coefficient was evaluated by Chern[92] and Rud[83,84]. For Cl-doped CdTe the diffusion coefficient was evaluated by Grill[85] for material with high chlorine doping level, $[Cl] = 5 \times 10^{18}$ cm^{-3} for temperatures 600℃ and 700℃.

Detailed understanding of reaction kinetics on the microscopic level has excited scientists since the van't Hoff's pioneer works[93] in 1884. It is generally believed that the reaction rate constant k may be expressed via Gibbs free energy change ΔG through the formula[94]

$$k \sim e^{-\frac{\Delta G}{k_B T}}, \tag{6.1}$$

where k_B is Boltzmann constant and T is absolute temperature. As k is tightly connected with $\tilde{D}$, and ΔG is defined by weakly temperature dependent changes of enthalpy ΔH and entropy ΔS,

$$\Delta G = \Delta H - T\Delta S, \tag{6.2}$$

the chemical diffusion coefficient $\tilde{D}$ attains the Arrhenius-type form

$$\tilde{D} = \gamma e^{\frac{\Delta S}{k_B}} e^{-\frac{\Delta H}{k_B T}}, \tag{6.3}$$

where the quantities weakly dependent on temperature are usually denoted in the literature as the pre-exponential term

$$D_0 = \gamma e^{\frac{\Delta S}{k_B}} \tag{6.4}$$

and activation energy

$$E_A = \Delta H \tag{6.5}$$

so as

$$\tilde{D} = D_0 e^{-\frac{E_A}{k_B T}} \tag{6.6}$$

is used[95].

Elaborate analyses of multiple processes described by the Arrhenius-type formulas revealed a surprising effect of correspondence between the logarithm of pre-exponential term and activation energy

$$\ln D_0 = a E_A + C. \tag{6.7}$$

Equation (6.7) expresses so-called compensation effect, named also enthalpy-entropy compensation, Meyer-Neldel rule (MNR) and many other names, see Liu[94], Lambert[96], Shcherbak[95] and references therein. Evidently, MNR, if it holds, reflects some hidden correlation between the enthalpy and entropy, which has not been uncovered yet.

Many authors have been theoretically studying MNR for years. Starikov[97,98] explained the MNR by enthalpy-entropy compensation, by a purely thermodynamic approach, in which he searched for hidden but physically real factors behind them. Liu[94] summarized tens of scientific papers and clarified the concepts of the isokinetic and isoequilibrium relationship and compensation effect, and summarized the theories on them to explain MNR. Magomedov[99] used the process of self-diffusion in the bulk of a simple substance and Dyre[100] presented a model based on an exponential probability distribution of energy barriers for the explanation of MNR. A recent overview of MNR investigation history was done by Starikov[101].

In this work we extend both experimental and theoretical background for the analysis of MNR by studying chemical diffusion in undoped and chlorine doped CdTe single crystals. Experiments were done on CdTe : Cl with a doping level of [Cl] $\approx 4.3 \times 10^{16}$ cm^{-3} where

$\tilde{D}$ is evaluated from the measurement of the time relaxation of electrical conductivity as a result of a step-wise change of ambient Cd pressure at temperatures 600℃, 700℃ and 800℃ and Cd pressure in the interval of 7×10^{-5} atm–1.2 atm. The experimental results are completed by theoretical calculations based on measurements of undoped CdTe[82] and heavily doped CdTe : Cl[85]. The chemical diffusion coefficient $\tilde{D}$ is evaluated independently for each temperature and the activation energy E_A and pre-exponential term D_0 are figured out. Evaluated E_A and D_0 are compared with already published experimental data for undoped CdTe[81–83] and for In-[83] and Cu-[83,92] doped CdTe. In addition, the experimental results are compared with published theoretical calculation for several types of defects[85,92,95,102–105] and also with experimental radiotracer measurements[103,105–107] and their theoretical calculations[92,108]. The validity of the Meyer-Neldel rule for diffusion in CdTe is critically assessed and its extension beyond standard linear region to a "triangle-shape area ($\Delta-$MNR)" is suggested.

The results of this chapter were successfully published at **Šedivý, L., Belas, E., Grill, R., Musiienko, A. & Vasylchenko, I. Extension of Meyer-Neldel rule using chemical diffusion experiments in CdTe. *Journal of Alloys and Compounds* 788, 897–904. ISSN: 0925-8388 (2019)**.

6.2 Experimental

The same sample, Cl-doped CdTe, **S57**, single crystal with [Cl] $\approx 4.3 \times 10^{16}$ cm^{-3}, and same experimental technique introduced at chapter 5 was used.

6.3 Results and Discussion

6.3.1 Determination of Chemical diffusion coefficient

Chemical diffusion coefficient $\tilde{D}$ can be evaluated using a single-exponential fit of the time relaxation of electrical conductivity, σ_t, after a step-wise change of Cd pressure using modified equation presented by Zanio[81] or Grill[82]:

$$|\sigma_t - \sigma_\infty| = A e^{-\frac{\tilde{D} t \pi^2 \left(a^2+b^2\right)}{a^2 b^2}}, \tag{6.8}$$

where a, b define the cross section of the sample, σ_∞ is the final conductivity, $A = |(\sigma_0 - \sigma_\infty)|$ is a normalization parameter, σ_0 is original conductivity before the step-wise change of Cd pressure and t is time.

The example of typical time relaxation of the electrical conductivity after step-wise changes of Cd pressure measured at 700℃, is shown in Fig. 6.1. It was found that the conductivity relaxation can be easily fitted for each temperature by a single exponential function according to equation (6.8), if the initial part of relaxation is skipped.

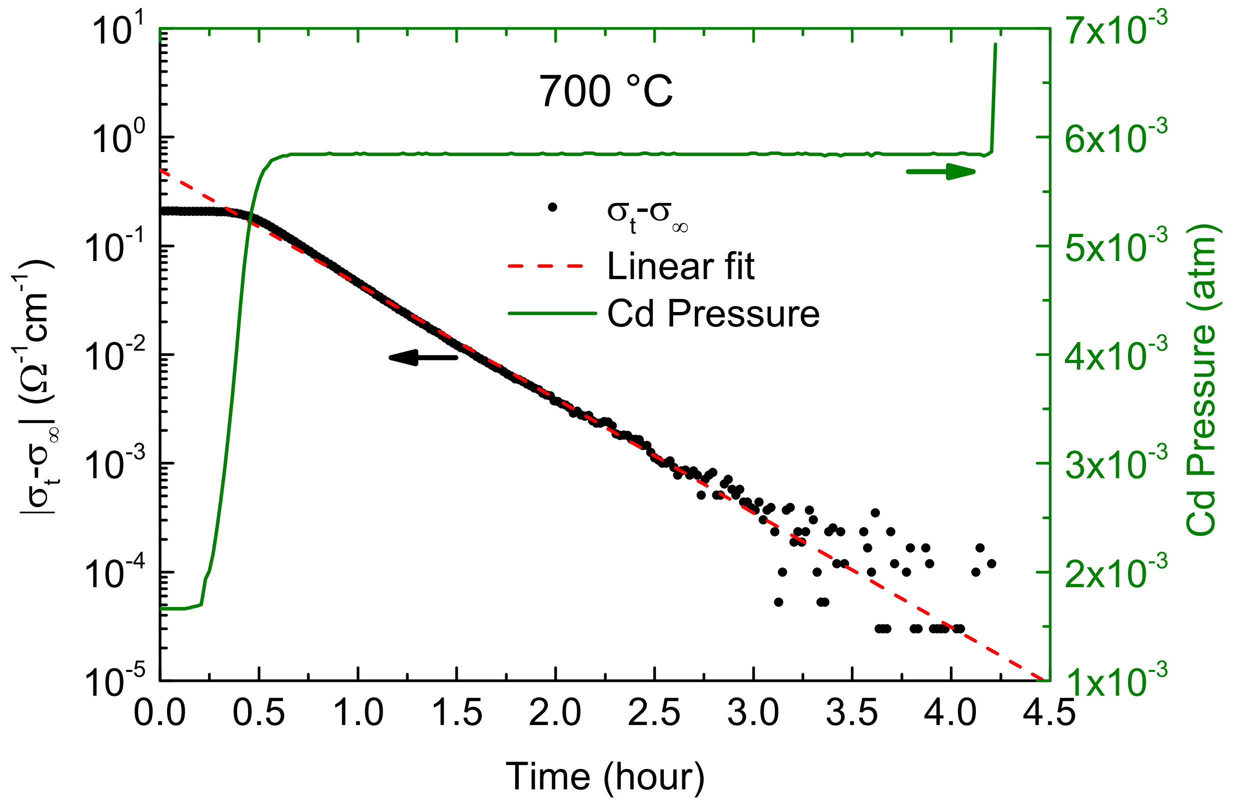

Figure 6.1: Typical time relaxation of the electrical conductivity at 700℃ (black points) after Cd overpressure step from 400℃ to 450℃, full line (green online), which corresponds to $\Delta\ P_{\mathrm{Cd}} = 4.18 \times 10^{-3}$ atm[67]. Dashed line (red online) represents linear fit according to equation (6.8).

The summary of experimentally evaluated $\tilde{D}$ is presented in Fig. 6.2 and completed by theoretical calculations based on a model for undoped CdTe[82] and for chlorine doped CdTe : Cl[85] with chlorine concentrations, [Cl] $= 2 \times 10^{16}$, 4×10^{16} and 1×10^{17} cm^{-3}, respectively. As one can see, the experimental results are described satisfactorily by theoretical model for CdTe : Cl with [Cl] $= 4 \times 10^{16}$ cm^{-3}. The original Zanio's experimental data for undoped CdTe[81] are added for a comparison, as it was found that the electrical conductivity relaxation after up/down pressure step yields usually differs, which cannot be explained within obvious single species diffusion theory. Therefore, $\tilde{D}$ presented in Fig. 6.2. using up/down pressure step are labelled by different labels, but as we can see the deviation of up/down $\tilde{D}$ is small and we may neglect that within the precision of the data evaluation. The effect was extensively studied by Rud[83,84], where a deviation of up/down $\tilde{D}$ correlating with the extrinsic defects doping was found. A detailed model explaining the mechanism of the effect is, however, still missing.

The temperature dependence of the mean value of the chemical diffusion coefficient established from experimental data for each temperature is plotted in Fig. 6.3. Based on equation (6.6) the activation energy $E_A = 1.38$ eV and pre-exponential factor $D_0 = 68$ cm^2 s^{-1} were determined and chemical diffusion coefficient can be described in the temperature interval 600–800 °C by $\tilde{D}\,(\mathrm{cm^2\,s^{-1}}) = 68 \exp(-1.38\ \mathrm{eV}/k_B T)$. Contingent dependence of $\tilde{D}$ on P_{Cd} was not established due to lower precision of evaluated data.

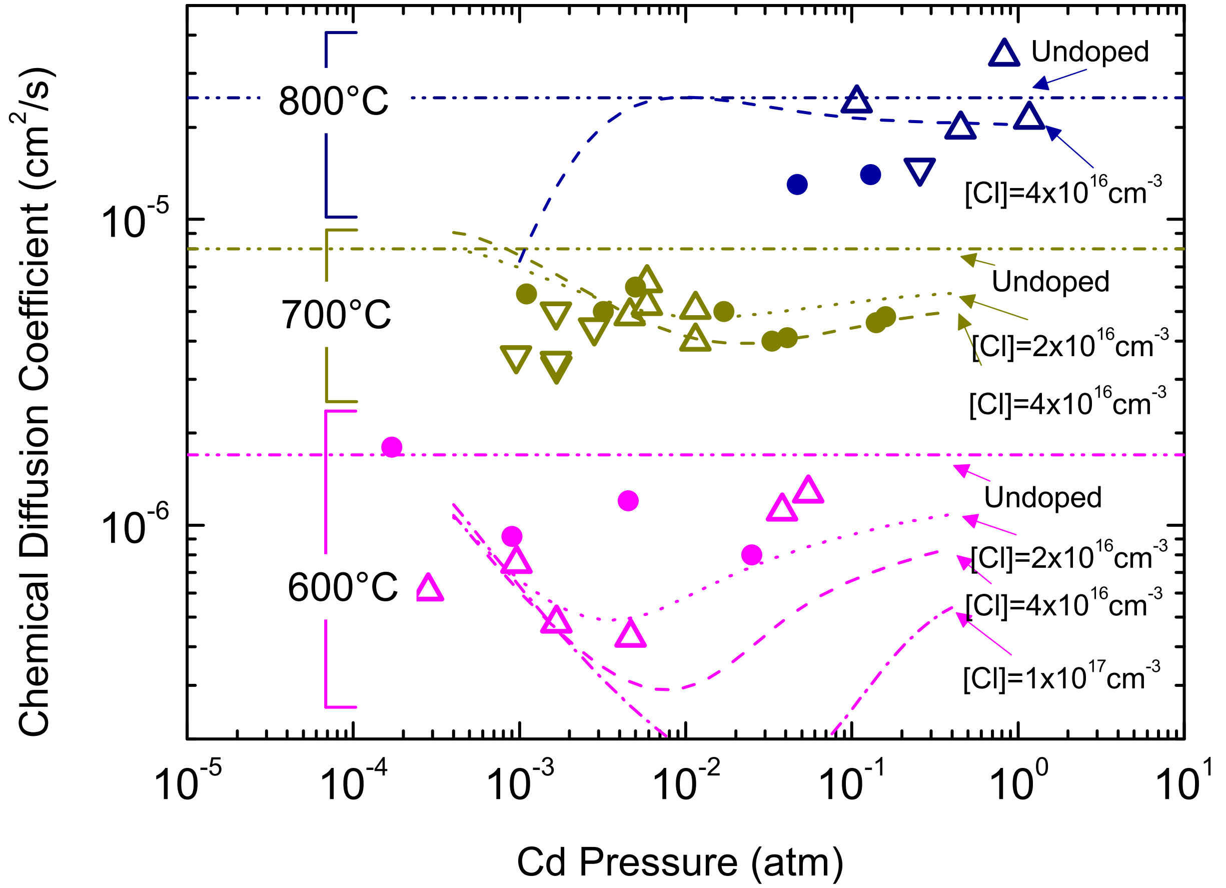

Figure 6.2: Pressure dependence of chemical diffusion coefficient at 600℃, 700℃ and 800℃, respectively (violet, beige and blue online). Top shaped triangles indicate step from lower Cd pressure to higher one, bottom shaped triangles are used for a step from higher Cd pressure to lower one. The full circles are experimental data for undoped CdTe obtained by Zanio[81]. The double dot-dashed lines are theoretical data for undoped CdTe, which were calculated based on $\tilde{D}$ given by Grill[82]. The dotted, dashed and dash-and-dot lines are theoretical data for CdTe : Cl calculated according to [85] for 2×10^{16}, 4×10^{16} and 1×10^{17} cm^2 chlorine doping, respectively.

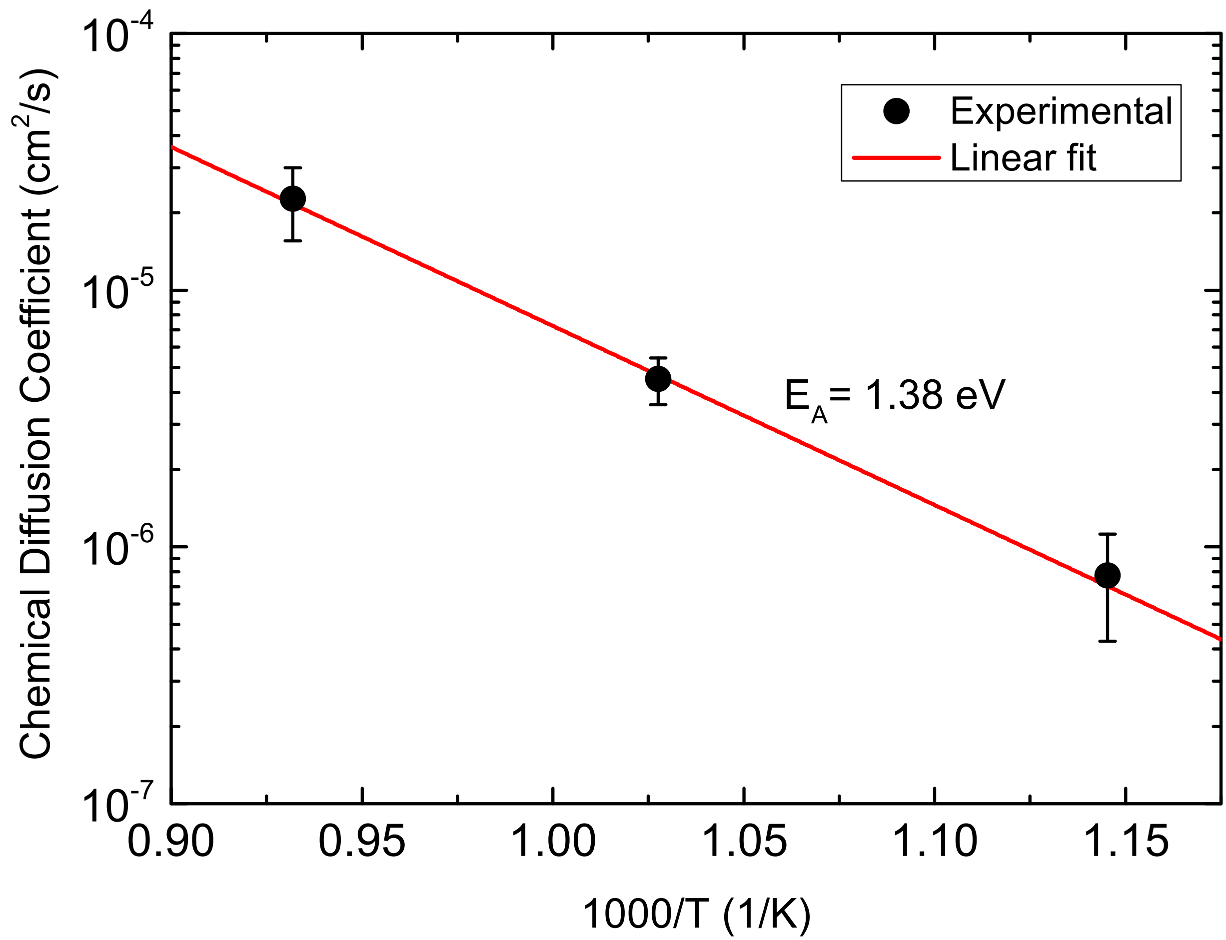

Figure 6.3: The experimental mean values of chemical diffusion coefficient at 600℃, 700℃ and 800℃, respectively. Full line represents linear fit.

6.3.2 Chemical diffusion coefficient simulations

Chemical diffusion coefficient is calculated based on the defect model[85,110], in which singly charged shallow donors Cl_{Te} or divalent donors, Cd interstitials (Cd_I), are compensated by divalent acceptors V_{Cd} and singly charged acceptor complexes $Cl_{Te} - V_{Cd}$, named A-centers[45]. Additionally, neutral three-defect complex $(V_{Cd}2Cl_{Te})$[88,111] appearing at large Cl doping density was completed. The chemical diffusion coefficient is derived within the local defect equilibrium and quasi-neutral approximation in the form[85]

$$\tilde{D} \;= -\frac{J_\Delta}{\frac{\partial \Delta}{\partial z}} = \sum\nolimits_{X,q} D_X^q \frac{X^q}{X^0} \left| \frac{dX^0}{d\Delta} \right| . \tag{6.9}$$

J_Δ represents the flux of stoichiometry deviation Δ, which is defined by

$$\begin{aligned} \Delta = [\mathrm{Cd}] - [\mathrm{Te}] = \\ = \left[\mathrm{Cd_I^0}\right] + \left[\mathrm{Cd_I^+}\right] + \left[\mathrm{Cd_I^{2+}}\right] - \left[\mathrm{V_{Cd}^0}\right] - \left[\mathrm{V_{Cd}^-}\right] - \left[\mathrm{V_{Cd}^{2-}}\right] + \\ + \left[\mathrm{Cl_{Te}^0}\right] + \left[\mathrm{Cl_{Te}^+}\right] + \left[\left(\mathrm{V_{Cd}^{2-}2Cl_{Te}^+}\right)^0\right], \end{aligned} \tag{6.10}$$

X^q and D_X^q are concentration and diffusion coefficients of defect X with charge q, respectively, and X^0 is concentration of neutral defect X. The diffusion of Cl is not assumed. Present, generally used model of chemical diffusion in undoped or weakly Cl-doped CdTe assumes that the dominant diffusing native defects are V_{Cd} at low P_{Cd} and Cd_I at high P_{Cd}.

Numerical simulations of pressure dependence of $\tilde{D}$ at 600°C and 700°C for different Cl concentrations are shown in Figs. 6.4, 6.5, respectively. We can see that for lower chlorine concentration nearly constant functions are obtained, which is in agreement with $\tilde{D}$ of undoped CdTe, where in spite of interchange of diffusion mechanisms $\tilde{D}$ remains surprisingly nearly constant in the whole interval of studied P_{Cd}[81,82]. The behaviour of $\tilde{D}$ for high chlorine doping truly follows $P_{Cd}^{-\frac{1}{2}}$ rule as predicted by the theory[85]. A more complex character of $\tilde{D}$ is found in the moderately doped CdTe : Cl where a local minimum at some specific P_{Cd} is identified. This course can be explained by a combination of diffusion mechanisms being ruled by V_{Cd} diffusion at low P_{Cd} and by Cd interstitial (Cd_I) diffusion at large P_{Cd}. Due to Cl doping and the Fermi-level effect[112] the V_{Cd} formation is suppressed in the medium P_{Cd} and $\tilde{D}$ is damped. At enhanced Cl doping above $1 \times 10^{18}\mathrm{cm}^{-3}$ the course of $\tilde{D}$ stabilizes due to the storage of excess Cl into $(V_{Cd}2Cl_{Te})$ complex. Chlorine doping changes the importance of different diffusion mechanisms in several ways: (i) Cl_{Te} induces the Fermi level shift towards the conduction band, which results in the increase of electron density and, on the other hand, in suppression of Cd_I[45]. Consequently, $\tilde{D}$ is reduced at high P_{Cd} as it is apparent in Figs. 6.4 and 6.5. (ii) In contrast to the Cd_I suppression due to the Fermi level shift, the V_{Cd} experience an enhancement and $\tilde{D}$ at low P_{Cd} increases, as may be seen especially in Fig. 6.5 (iii) Extensive Cl doping results in the formation of $Cl_{Te} - V_{Cd}$ acceptor complexes. These complexes hold principal portion of

V_{Cd} in the material, making them immobile. Due to suppressed $[Cd_I]$ and $[V_{Cd}]$ mostly fixed in complexes, $\tilde{D}$ overall decreases in heavily doped CdTe : Cl as it is correspondingly well seen in Figs. 6.4, 6.5. Simulations at selected P_{Cd} are correlated with the experimental results in Fig. 6.2 and the profile of $\tilde{D}$ conforms with $[Cl] \approx 4 \times 10^{16}$ cm^{-3} determined by Hall effect measurements.

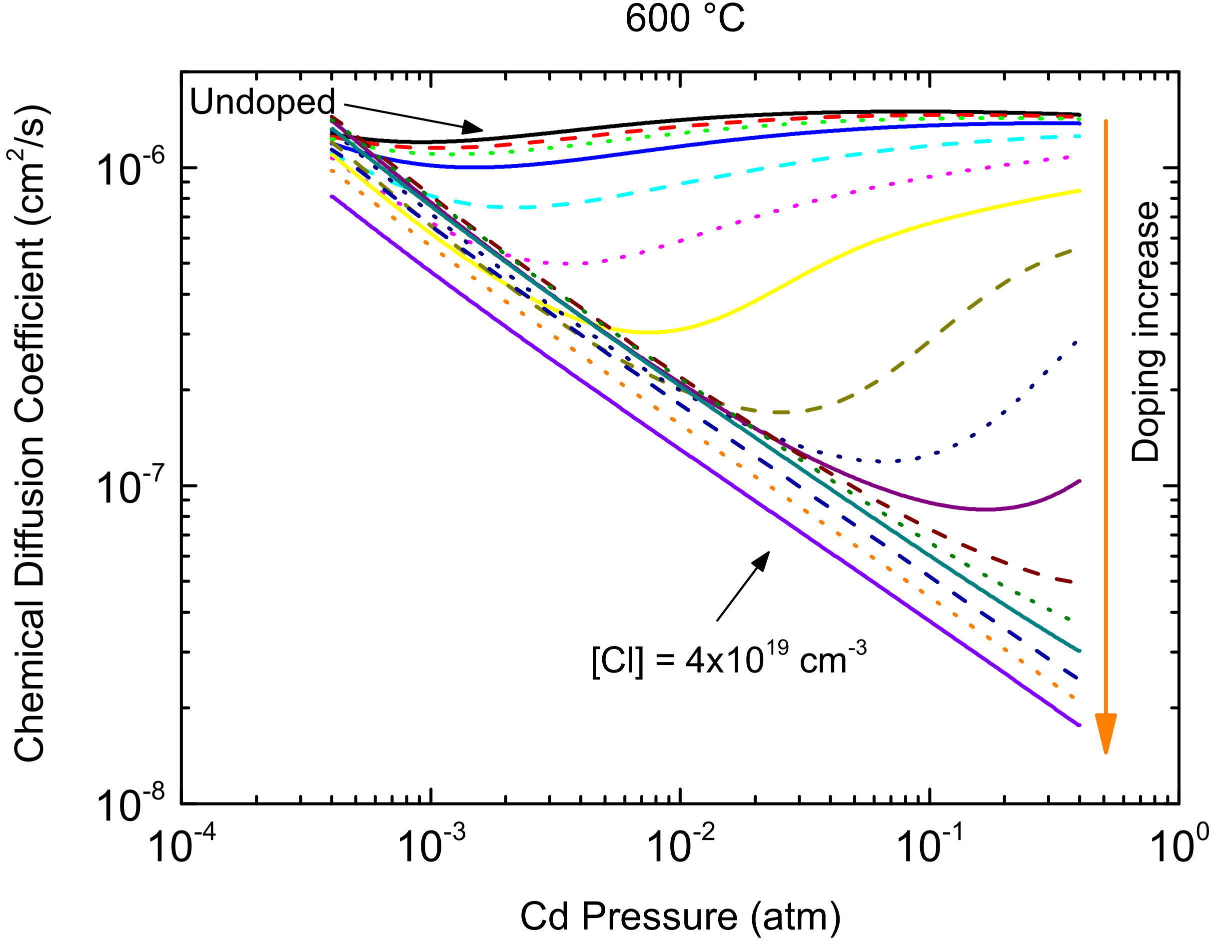

Figure 6.4: Calculated pressure dependence of chemical diffusion coefficient $\tilde{D}$ for different Cl doping at 600°C. First upper line represents undoped CdTe and then the chlorine concentration increases in the arrow direction with non-linear steps (1, 2 and 4×10^{15}–10^{19} cm^2).

6.3.3 Discussion of Meyer-Neldel rule in CdTe : Cl

The Meyer-Neldel rule expressed by equation (6.7) postulates a linear dependence of $\ln(D_0)$ on E_A. We made an extensive search over published data about the chemical diffusion and radiotracer self-diffusion coefficient of CdTe and presented them in Table 6.1 and Table 6.2, respectively. The relevant data for the MNR validity inspection were summarized in Fig. 6.6, where the data of $\tilde{D}$ for undoped CdTe[81–83] and doped CdTe[83,92] are

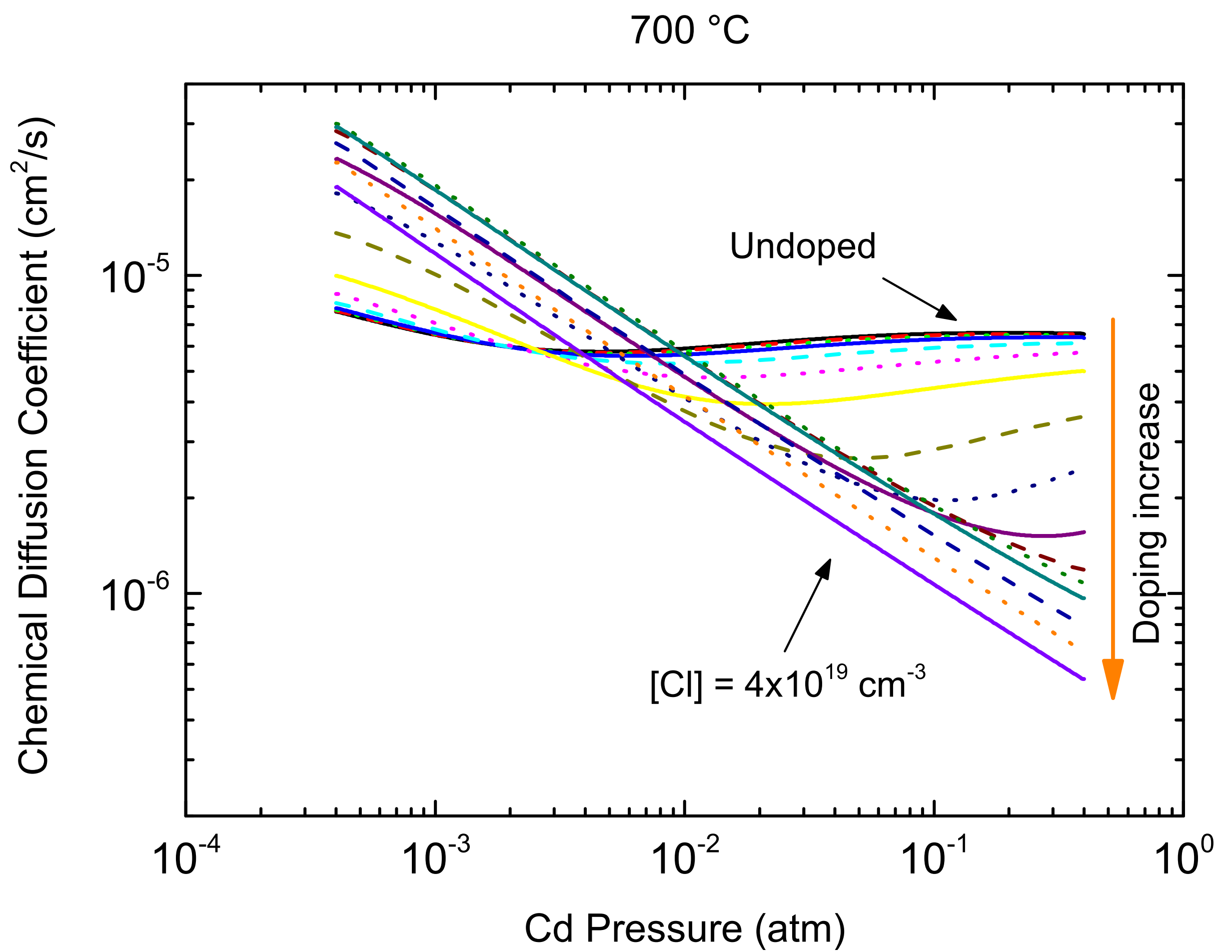

Figure 6.5: Calculated pressure dependence of chemical diffusion coefficient $\tilde{D}$ for different Cl doping at 700°C. First upper line represents undoped CdTe and then the chlorine concentration increases in the arrow direction with non-linear steps (1, 2 and 4×10^{15}–10^{19} cm^2).

combined together with experimental data published in this paper. In addition, the experimental results are compared with published theoretical calculations for several types of defects[85,92,95,102–105], see Table 6.3, and also with experimental self-diffusion data[103,105–107] and their theoretical calculations[92,108]. Full symbols in Fig. 6.6 represent E_A and D_0 deduced directly from measured $\tilde{D}$ and D^* while open symbols show data of specific point defects evaluated within various defect models (see Table 6.1, 6.2 and 6.3, for detailed description).

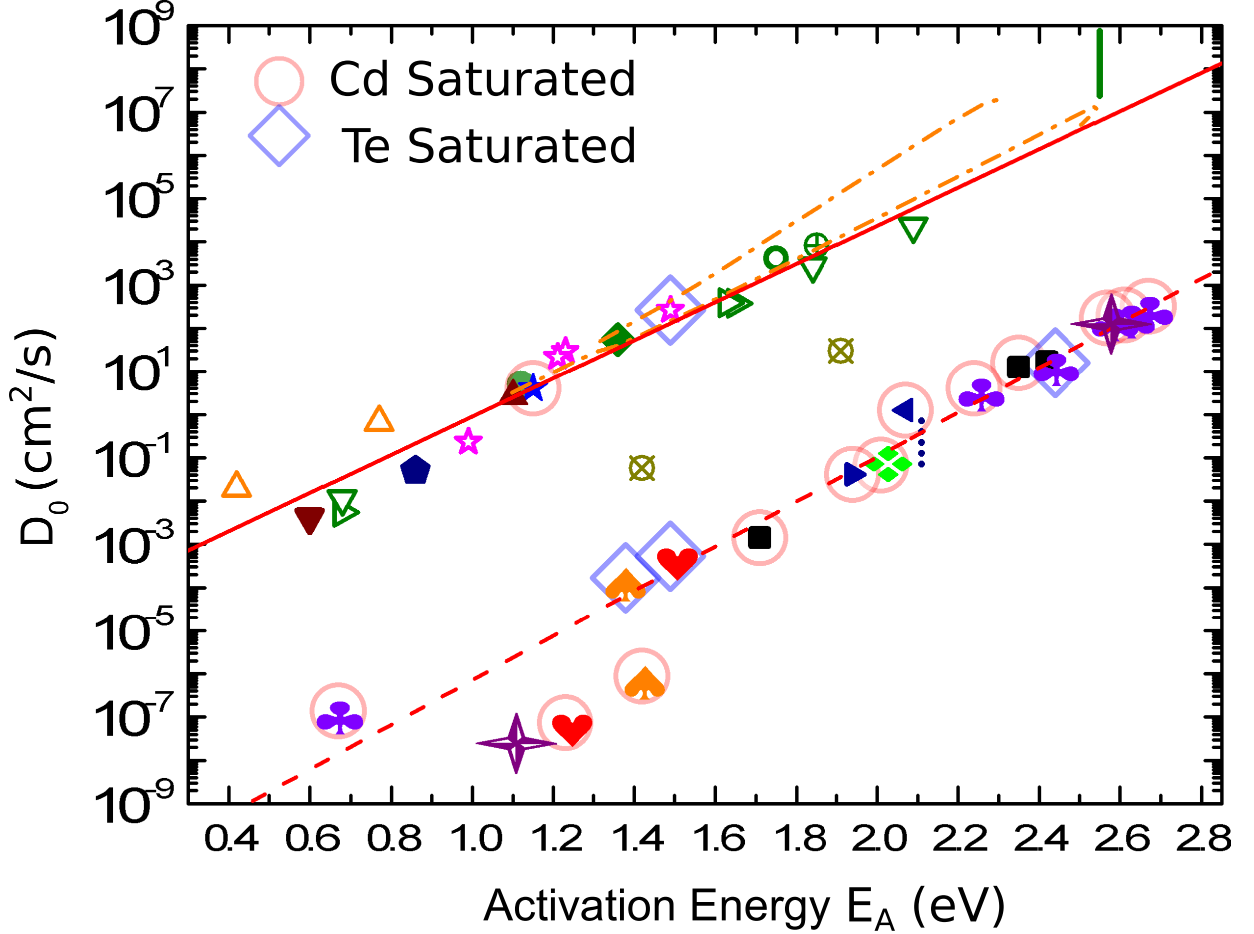

Figure 6.6: The plot of the pre-exponential factor D_0 as a function of the activation energy E_A collected from accessible chemical diffusion and self-diffusion data are summarized in Tables 6.1, 6.2 and 6.3. Full line represents the fit of chemical diffusion and single point diffusion data, dashed line is the fit of self-diffusion data. The region delimited by dash-and-dot lines represents generalized triangular MNR discussed in the text.

We can see in Fig. 6.6 that there are many data points following two separate single lines for chemical diffusion and self-diffusion, respectively, almost without any connection to dopants concentration, experimental conditions etc. Systematically much slower self-diffusion than the chemical diffusion is in agreement with theoretical prediction[92,103]. Consistent model

explaining the relative positions of lines has not been presented yet. Surprisingly, for doping with elements occupying Cd sublattice (Cu, In, Al) E_A and D_0 exhibit lower value than for elements in Te sublattice (Cl) regardless of their electrical state (donor/acceptor) in the lattice. In case of Cu-doping one may suspect that respective $\tilde{D}$ could be affected by the fast diffusion of Cu in CdTe[113].

Tables

Table 6.1: Chemical diffusion coefficient, $\tilde{D}$.

Symbol	Diffused Elements	Doping (cm^2)	E_A (eV)	D_0 (cm^2/s)	Ref.	Comments
●		Undoped	1.12	5	[82]	Electrical conductivity, P_{Cd}
◆		$[\mathrm{Cl}] = 4.3 \times 10^{16}$	1.36	54.38	This paper	Electrical conductivity, $500 - 800$°C, P_{Cd}
▲	–	Undoped	1.1	2.66	[83]	900°C, P_{Cd}, Based on raw data at Tab. 1 in [83]
▼		Cu and In	0.6	4.16×10^{-3}		900°C, P_{Cd}, Based on raw data at Tab. 1 in [83]
⬟		$[\mathrm{In}] = 5 \times 10^{17}$	0.86	5×10^{-2}	[92]	645°C, 700°C, P_{Cd}, Calculated from raw data at Fig. 5 in [92]
★		Undoped	1.15	4	[81]	Electrical conductivity, 550–800°C, P_{Cd}

Table 6.2: Self diffusion coefficient, D^*.

Symbol	Diffused Elements	Doping (cm^{-3})	E_A (eV)	D_0 (cm^2/s)	Ref.	Comments
♣	^{109}Cd	$[\mathrm{Al}] = 5 \times 10^{17}$	0.67	1.37×10^{-7}	[106]	P_{Cd}^{sat}
		Probably undoped	2.44	15.8		P_{Te}^{sat}
		Probably undoped	2.67	326		P_{Cd}^{sat}
		-	2.07	1.26	[95, 103],	According to [107]
		-	2.61	203	[103]	P_{Cd}^{sat}, according to [107]
		-	2.42	16.6	[91, 103]	P_{Te}^{sat}, according to [107]
❖	^{109}Cd	-	2.01	6.67×10^{-2}	[92]	P_{Cd}^{sat}, exchange mechanism using V_{Cd} diffusion ($D^*(V_{\mathrm{Cd}}\mathrm{Cd_I})$), according to [106]
■	^{109}Cd	-	2.57	171	[103]	P_{Te}^{sat}, according to [92]
		-	2.35	12.5		P_{Cd}^{sat}, according to [114]
		-	1.71	1.41×10^{-3}		P_{Te}^{sat}, according to [114]
♠	^{123}Te	Undoped	1.42	8.54×10^{-7}	[91, 106]	P_{Cd}^{sat},
		Undoped	1.38	1.66×10^{-4}	[106]	P_{Te}^{sat}
♥	^{123}Te	-	1.49	4.3×10^{-4}	[103]	P_{Te}^{sat}, according to [107]
		-	1.23	7.4×10^{-8}		P_{Cd}^{sat}, according to [107]
▶	Cd	-	1.94	4.1×10^{-2}	[105]	P_{Cd}, theory
◀	Te	-	2.24	4		
✦	Cd	-	2.55	125	[115]	} P_{Cd}, double exponential fit
		-	1.08	2.48×10^{-8}		

In spite of the double linear ordering being in accordance with MNR, there are also data deviating from this rule, some of them appear as pretty safe. A clear break of standard MNR was experimentally proven by self-diffusion measurements on undoped CdTe represented by two pairs of data, (♠ or ♥), in Fig. 6.6, measured on the same material differing

Table 6.3: Diffusion coefficients of individual defects D_i

Symbol	Defects	Doping (cm^{-3})	E_A (eV)	D_0 (cm^2/s)	Ref.	Comments
○	V_{Cd}^{2-}	$[In] = 4 \times 10^{18}$	1.75	4.2×10^3	[85]	P_{Cd}, Defect model and chemical diffusion experiment
⊕	V_{Cd}^{2-}	-	1.85	8.22×10^3	[85, 92, 105]	P_{Cd}, Defect model and self-diffusion and chemical diffusion experiment
▽	V_{Cd}^{2-}	$[Al] = 5 \times 10^{17}$	0.68	1.1×10^{-2}	[95, 103]	Review – Calculation, P_{Cd}^{Sat}
		$[In] = 2.7 \times 10^{17} - 2.7 \times 10^{18}$	1.84	2.74×10^3	[92]	P_{Cd}, Defect model and self-diffusion and chemical diffusion experiment
		$[In] = 2.7 \times 10^{17} - 2.7 \times 10^{18}$	2.09	2.24×10^4	[104]	P_{Cd}, Defect model and self-diffusion and chemical diffusion experiment
|	V_{Cd}^{2-}	$[Cl] = 4 \times 10^{18}$	2.55	$1.5 \times 10^7 \cdot p^{-\frac{1}{2}}$	[85]	Defect model and experiment, P_{Cd}
▷	V_{Cd}^{-}	$[Al] = 5 \times 10^{17}$	0.68	5.5×10^{-3}	[95, 103]	Review – Calculation, P_{Cd}^{Sat}
		$[In] = 2.7 \times 10^{17} - 2.7 \times 10^{18}$	1.63	3.9×10^2	[92]	P_{Cd}, Defect model and self-diffusion and chemical diffusion experiment
		$[In] = 2.7 \times 10^{17} - 2.7 \times 10^{18}$	1.65	3.8×10^2	[104]	P_{Cd}, Defect model and self-diffusion and chemical diffusion experiment
⊗	V_{Te}^{2+}	$[In] = 2.7 \times 10^{17} - 2.7 \times 10^{18}$	1.42	2.04×10^{-2}	[92]	P_{Cd}, Defect model and self-diffusion and chemical diffusion experiment
		$[In] = 2.7 \times 10^{17} - 2.7 \times 10^{18}$	1.91	6.6×10^{-1}	[104]	P_{Cd}, Defect model and self-diffusion and chemical diffusion experiment
△	Te_I	$[In] = 2.7 \times 10^{17} - 2.7 \times 10^{18}$	0.42	2.04×10^{-2}	[92]	P_{Cd}, Defect model and self-diffusion and chemical diffusion experiment.
		$[In] = 2.7 \times 10^{17} - 2.7 \times 10^{18}$	0.77	6.6×10^{-1}	[104]	P_{Cd}, Defect model and self-diffusion and chemical diffusion experiment
☆	Cd_I^{2+}	CdTe : Cu/undoped CdTe	0.99	2.3×10^{-1}	[105]	Review: equilibrium constant model based on self diffusion[116] and chemical diffusion[117] experiments.
		$[In] = 2.7 \times 10^{17} - 2.7 \times 10^{18}$	1.21	2.17×10^1	[92]	P_{Cd}, Defect model and self-diffusion and chemical diffusion experiment
		$[In] = 2.7 \times 10^{17} - 2.7 \times 10^{18}$	1.49	2.63×10^2	[92]	P_{Cd}, Defect model and self-diffusion and chemical diffusion experiment
		$[In] = 2.7 \times 10^{17} - 2.7 \times 10^{18}$	1.23	2.94×10^1	[104]	P_{Cd}, Defect model and self-diffusion and chemical diffusion experiment
⋮	Cd_I^{2+}	$[In] = 2.7 \times 10^{17} - 2.7 \times 10^{18}$	2.01	$0.95 p_{Cd}^{\frac{1}{3}}$	[92]	V_{Cd} Pressure dependency based on defects model

only by ambient atmosphere and yielding significantly different D_0 with similar E_A. The violation of standard MNR is also manifested by pressure dependence of D_0 for chemical[85] and radio-tracer[92] diffusion represented by green full-line and blue dotted line (color online) in Fig. 6.6.

On summarizing collected experimental data, we conclude that there are not sufficient experimental records for chemical diffusion for clear verification of MNR. Except for well-documented measurements on undoped CdTe, additional experiments should be done on doped CdTe using various doping elements with different density, both donors and acceptors, occupying both Cd- and Te- sublattice. Wide range of P_{Cd} or P_{Te} is envisaged. Theoretical data related to individual defects exhibit a large spread in Fig. 6.6 and depend on the chosen defect model, which was not verified by an independent experiment. Standard linear MNR is not in concord with comprehensive diffusion data due to its simplicity as it does not reflect the P_{Cd} dependence of $\tilde{D}$, which appears in the theoretical formulas and in experiments. One should also consider an inaccuracy of measured $\tilde{D}$ fitted by the model using multiple defects. Even weak experimental inaccuracy of $\tilde{D}$ may significantly influence the properties of the defect while having a minor effect on $\tilde{D}$. An argument that such a premise should be taken seriously into account stems from the fact that the full line in Fig. 6.6 may be approximated by the formula

$$D_0 = 3.4 \times 10^{-5} e^{\frac{E_A}{k_B \cdot 1140\mathrm{K}}} \mathrm{cm}^2/\mathrm{s}. \tag{6.11}$$

The characteristic temperature $T_c = 1140$ K defining the slope of the line is situated near the middle of temperature interval 650°C – 950°C usually used for CdTe in diffusion experiments. Such a finding points to the suspicion that some points in Fig. 6.6 characterising the diffusion of point defects with low or high E_A appear as a consequence of compensating effect of the artificial model of diffusion assigning experimental shortage to a seemingly real physical effect. We also noted that experimental points conforming to the single linear MNR expressed by equation (6.11) predict equal $\tilde{D} = 3.4 \times 10^{-5}$ cm^2/s of all considered defects at T_c. Apparently, in view of the fact that different experiments are largely interpreted by different diffusing point defects or diffusing mechanisms, the uniform $\tilde{D}(1140\ \mathrm{K})$ raises doubts of their common validity.

With the aim to understand the behaviour of $\tilde{D}$ and its relationship with MNR more thoroughly, we calculated $\tilde{D}$ for different [Cl] at 600°C and 700°C shown in Fig. 6.4 and Fig 6.5 respectively, and calculated corresponding D_0 and E_A assuming simple Arrhenius-type evolution of $\tilde{D}$ (see Equation (6.6)) between these temperatures. The result of the simulation is presented in Fig. 6.7, where D_0 vs E_A parametrized by P_{Cd} is plotted for nonlinear steps of [Cl] as (1, 2 and 4×10^{15}–10^{19} cm^2) respectively. The variability of $\tilde{D}$ is limited by the area between dash-and-dot lines (red online), which were obtained as an envelope of all calculated D_0 and E_A points. It is seen that both D_0 and E_A tend to lower values at the lowest and highest P_{Cd} while they rise at the medium P_{Cd}. The evolution is caused by the enhanced formation of A-centres at medium P_{Cd}, which slow down the diffusion at low temperature and induce the enhancement of E_A. Plots representing large

[Cl] > 1×10^{18} cm^2 show the deviation from the trend apparent at the lower Cl-doping, revealing even weak regression to lower E_A and D_0 at [Cl] > 4×10^{18} cm^2. This feature is caused by the ($V_{Cd}2Cl_{Te}$) complex formation, which stabilizes $\tilde{D}$ and results in significant attenuation of the effect of Cl-doping on $\tilde{D}$. Similar effects could be seen even at much less [Cl] in samples annealed at temperature lower than 600°C. Significant portion of neutral defect complexes in CdTe : Cl was identified by positron annihilation spectroscopy[118].

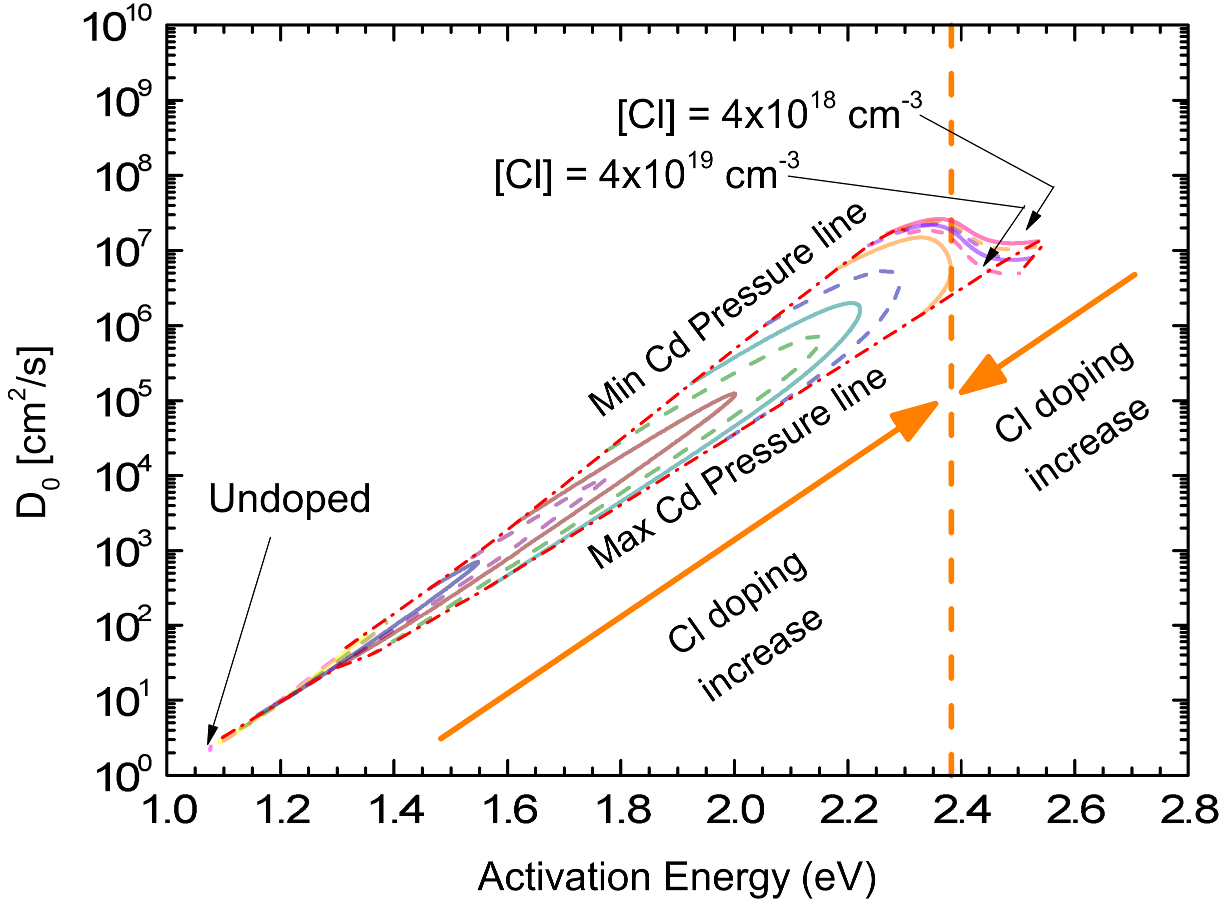

Figure 6.7: Detail of Meyer-Neldel rule calculation for different Cl-dopping of CdTe : Cl. The region delimited by dash-and-dot lines represents generalized triangular MNR discussed in the text.

One can see from Fig. 6.7 that the convergence of theoretical model to the linear dependence of D_0 on E_A fits pretty well at low [Cl] $\leq 4 \times 10^{16}$ cm^2. For higher Cl-doping, the linear rule is transformed to the triangle MNR consistent with predicted dependence of $\tilde{D}$ on P_{Cd} at high [Cl][85].

Comparing the area covered by the triangle MNR with experimental data as shown in Fig. 6.6, we may observe a very good agreement of the fit plotted by the full line with the boundary of the triangle MNR representing the diffusion near Cd saturation. Since the experimental points defining the fit were dominantly evaluated from diffusion data

measured near Cd saturation and the theoretical shape of the triangle MNR was calculated without any fitting parameter using only previously published data of defect models and defect reactions, the detected accord represents an important supporting argument for the validity of the defect model of CdTe : Cl as well as of the diffusion coefficients of considered native point defects.

Based on data in Fig. 6.7, we conclude that the standard MNR is valid only for undoped CdTe and for low doping level ($[\mathrm{Cl}] \leq 4 \times 10^{16}$ cm^2). At higher doping, MNR cannot be fit well by the linear function and it must be transformed to the "triangle-shaped area", which we call "triangle shape Meyer-Neldel rule (Δ-MNR)". Simulations show that generalized Δ-MNR is in agreement with standard diffusion theory of donor-doped CdTe and follows well both the linear shape of classical MNR at low [Cl] and the P_{Cd} dependence at high [Cl]. The question remains on the reduced E_A and D_0 measured in Al- and In-doped CdTe, see Fig. 6.6. Because the defect chemistry of Al and In donors occupying Cd sublattice is expressed by similar formulas as it is in the case of $\mathrm{Cl_{Te}}$, the reason for their quite different effect to the diffusion remains undisclosed within the presented model. A possible explanation could be based on the propensity of Cd-substituting donors to escape easily to the interstitial sites and participate in the diffusion process. Detailed exploration of such a puzzle is thus advisable. Moreover, diffusion experiments should be extended to acceptor-doped CdTe using stable, slowly diffusing elements like As, Sb and possibly Rb. Such experiments are completely absent in relevant literature and they could help to clarify the problem of MNR in a more comprehensive scope.

6.4 Conclusions

Chemical diffusion in CdTe : Cl, [Cl] $\approx 4.3 \times 10^{16}$ cm^{-3} was measured at temperatures $T = 600 - 800$°C by means of the relaxation of conductivity of bar-shaped sample after the step-wise change of Cd pressure, and successfully fit with previous theoretical model deduced for undoped and heavily Cl-doped CdTe. The chemical diffusion coefficient $D\,(\mathrm{cm^2\,s^{-1}}) = 68\exp(-1.38\ \mathrm{eV/k_BT})$ was determined. Based on sample size and applied temperature, one can set the optimal delay of annealing steps, requested at chapter 4. Simultaneously, the cooling speed could be individually set up for each sample based on this chemical diffusion coefficient.

The deviation of $\tilde{D}$ in chlorine doped CdTe from the constant function appearing in undoped CdTe was explained as a consequence of doping-induced enhancement or suppression of distinct diffusion mechanisms. Obtained diffusion data were completed by an extensive overview of relevant literature and respective activation energies, and pre-exponential terms characterizing the chemical diffusion and self-diffusion in undoped CdTe and CdTe doped by different elements were comprehensively plotted. Meyer-Neldel rule was critically discussed and its factual failures were accentuated. It was argued that seemingly valid MNR partly expresses deficiencies of experimental approaches and theoretical models used in the evaluation of diffusion coefficients of respective defects. A generalized triangle-shaped Meyer-Neldel rule that is in accordance with a theoretical model of chemical diffusion in undoped and Cl-doped CdTe was presented. The validity of Δ-MNR stems directly from the defect model used and it does not request any additional premises on enthalpy-entropy compensation.

7. Positron annihilation spectroscopy

7.1 Introduction

The Chapter 4 revealed a question of existence and origin of unidentified temperature activated reservoir of electrically neutral chlorine, which release chlorine during cooling and dynamically contributed Cl_{Te}^{+} to electrical compensation. The suspicion of existence such type of reservoir was supported by results at chapter 5, which experimental results can not be properly described by any standard models. In addition, advanced defect model containing Cl-related type of defects, which described an experimental data of Chapters 5 and 6 the most properly, assume an existence of $\left(V_{Cd}^{2-} + 2Cl_{Te}^{+}\right)^{0}$ neutral defects. This type of defects have not been experimentally proved yet, because not many experimental technique allow a measurement of electrically neutral defects with low concentration.

Positron annihilation spectroscopy (PAS) including Positron lifetime (LT) and Coincidence Doppler broadening (CDB) spectroscopy was usually used for the study of the structure of point defects in CdTe/CdZnTe in the past,[119–124] but the link between defects and controlled annealing treatment has never been studied before.

This chapter reports on an investigation of the influence of defined annealing in Cd or Te vapour on the defect structure of Cl-doped CdTe and Ge-doped CdZnTe semi-insulating single crystals, which is used for validation of PAS itself. The defect structure is characterized by PAS before and after each annealing step. The results are compared with galvanomagnetic Hall effect measurements in the Van der Pauw configuration.[125]

The results of this chapter were published at prestige scientific journal, **Šedivý, L., Čížek, J., Belas, E., Grill, R. & Melikhova, O. Positron annihilation spectroscopy of vacancy-related defects in CdTe:Cl and CdZnTe:Ge at different stoichiometry deviations. *Scientific Reports* 6, 20641. ISSN: 2045-2322 (2016)**.

7.2 Samples

The Cl-doped CdTe (CdTe:Cl) and Ge-doped $Cd_{1-x}Zn_{x}Te$, $x \sim 0.035$ (CdZnTe:Ge) single crystals were grown by the vertical gradient freeze method[70]. The annealing was done in the two zone furnace at 700 °C while the Cd or Te source temperature was 600 °C, which corresponds to Cd or Te pressure of 111 or 7.7 mbar, respectively. After annealing, the samples were cooled down at a cooling rate of $1\,^{\circ}\mathrm{C\,min^{-1}}$. Nominally undoped CdTe (u-CdTe) single crystal grown by the vertical gradient freeze method at fairly increased Cd overpressure 1.6 atm was used as a reference sample.

7.3 Experimental technique

7.3.1 Physical principles of positron annihilation spectroscopy

Positrons are usually generated by radioisotopes undergoing β^+ decay described by

$$ {}^{A}_{Z}X \quad \rightarrow \quad {}^{A}_{Z-1}X' + e^+ + \nu, \tag{7.1} $$

where nucleus ${}^{\mathrm{A}}_{\mathrm{Z}}\mathrm{X}$ simultaneously emits positron e^+ with high kinetic energy, neutrino ν and decays to nucleus ${}^{\mathrm{A}}_{\mathrm{Z-1}}\mathrm{X}'$.

In case of ${}^{22}_{11}\mathrm{Na}$, commonly used at laboratory, the decay produces the daughter ${}^{22}_{10}\mathrm{Ne}$ nucleus in excite state, which subsequently de-excites by emission of γ ray, so called start photon, with characteristic energy of 1274 keV.

Positron penetrating into semiconductor quickly loses its initial kinetic energy until it reaches thermal energy of $\sim \frac{3}{2}kT$. This process is usually called positron thermalization[126] and at condensed matter takes several ps, which is significantly less then typical lifetime of positron in semiconductor, typically around hundreds ps. Hence, the thermalization time of positron is shorter than the positron lifetime and can be neglected in most circumstances.

Thermalized positrons are scattered almost exclusively by phonons and in the classical approximation positrons perform a random isotropic diffusion motion in material. Scattering by phonons leads to temperature dependence of the positron diffusion coefficient[127]

$$ D_+ \quad \sim \quad \frac{1}{\sqrt{T}}. \tag{7.2} $$

Velocity of positron in thermal equilibrium is define by the classic Maxwell-Boltzmann distribution, which states that the mean square velocity of positron is

$$ v_+ \quad \equiv \quad \sqrt{\langle v^2 \rangle} = \sqrt{\frac{3kT}{m^*}}, \tag{7.3} $$

where k is Boltzman constant, T temperature and m^* is the effective positron mass, which reflects the interaction of positron with condensed matter and includes contribution of phonons, positron band structure and electron-positron interaction.

The mean diffusion length L_+, typically $\sim$ 100 nm is defined as the mean distance which positrons travel from the point of their thermalization to the place of annihilation during their lifetime τ_I like

$$ L_+ \quad = \quad \sqrt{D_+ \tau_I}. \tag{7.4} $$

The positron wavelength define as de Broglie wave could be written as

$$\lambda_+ = \frac{2\pi\hbar}{p} = \frac{2\pi\hbar}{m^* v_+}. \quad (7.5)$$

The positron wavelength,λ_+, in defect free condensed matter, $\sim$ 5.2 nm at room temperature, is always larger than the interatomic distance, $\sim$ Å. Therefore, positrons in condensed matter behave as waves and we speak about delocalized or free positrons. However, the negatively charged defects or free volume defects at crystal lattice leads to positron localization.

During its lifetime positron explores mean volume of $\lambda_+^2 L_+$ hence volume explored by a positron during its lifetime in the sample contains about 10^7 atoms.

7.3.2 Positron lifetime spectroscopy (LT)

Positron lifetime, experimentally set as time delay between start photon (γ_1) detected at time t_0, and the photon emitted by positron annihilation with some electrons, (γ_2) detected at time $t > t_0$, see Fig. 7.1. The positron could either annihilate in defects-free semiconductor as a free positrons with a bulk lifetime τ_B or it could be trapped at negatively charged defects or at free volume defects τ_d. Schematically is the situation showed at Fig. 7.2.

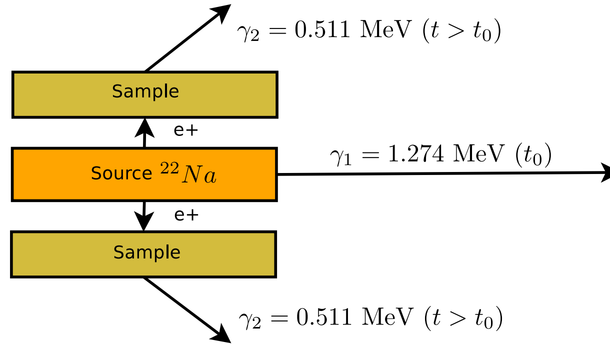

Figure 7.1: Positron lifetime spectroscopy scheme at sandwich geometry

LT measurements were carried out using a digital spectrometer[128] with time resolution of 145 ps. ^{22}Na activity of 1 MBq deposited on a 2 μm thick Ti foil was used as a positron source. The LT measurements were performed at 295 K (room temperature - RT) and at 123 K (low temperature), respectively in sandwich configuration, see Fig. 7.1. In both temperatures typically, 10^7 positron annihilation events were collected in LT spectra, which were subsequently decomposed into exponential components. The contribution of positron annihilations in the source spot and in the covering foils were always subtracted. In addition, temperature-dependent LT measurements were carried out in the temperature range of 123-295 K at a heating rate of $\sim$ 1 K hour^{-1}. Here the statistics of 5×10^5 events was collected at each temperature step.

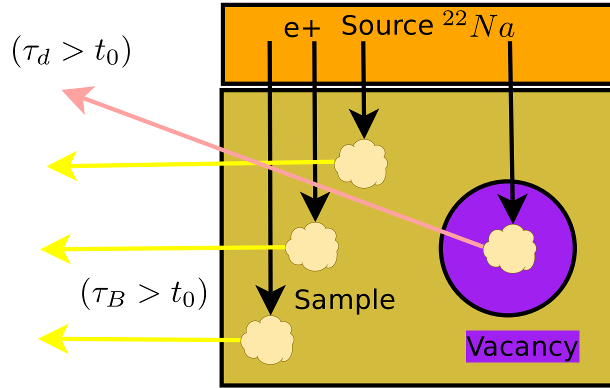

Figure 7.2: Scheme of positron annihilation at semiconductor with vacancies.

7.3.3 Coincidence Doppler broadening spectroscopy (CDB)

The laws of energy and the momentum conservation implies that at least two annihilation photons must be created during annihilation of the electron-positron pair, where the probability of creation of two photons is significantly higher, then other possibility[129].

As was mentioned above, after the thermalization positrons loses its initial kinetic energy. Hence, the momentum of annihilating electron-positron pair is driven by the electron which annihilates the positron. Non-zero momentum of the electron-positron pair occurred the Doppler shift ΔE of the measured energy of annihilation photons

$$\Delta E = \frac{1}{2}cp_L, \tag{7.6}$$

where p_L is a momentum component of the electron-positron pair in the direction of emitted photons.

Therefore, the measured annihilation peak located at the energy of 511 keV is broadened by Doppler shift projected into the axis connecting the sample and the detector. The core electrons have a high momentum, so the doppler shift caused by its annihilation with positrons is the highest. The momentum distribution of core electrons is unique for each chemical element, so doppler broadening of positron annihilation radiation carries information about chemical composition around positron annihilation sites.

CDB spectroscopy[130] was employed for characterization of local chemical environment of vacancies. The CDB studies were performed at RT using the same positron source as in the LT measurements, see Fig. 7.3. A digital CDB spectrometer[131] equipped with two High Purity Germanium (HPGe) detectors and characterized by the energy resolution of 0.9 keV at the annihilation line and the peak-to -background ratio $> 10^5$ was employed for the CDB studies. At least 10^8 annihilations were collected in each two-dimensional CDB spectrum. Subsequently the CDB spectra were reduced into one-dimensional cuts representing the resolution function of the spectrometer and the Doppler broadened annihilation peak. Normalized Doppler broadened peaks were divided by the normalized peak for the

u-CdTe reference sample. Hence, in this paper the CDB results are presented ratio curves with respect to u-CdTe.

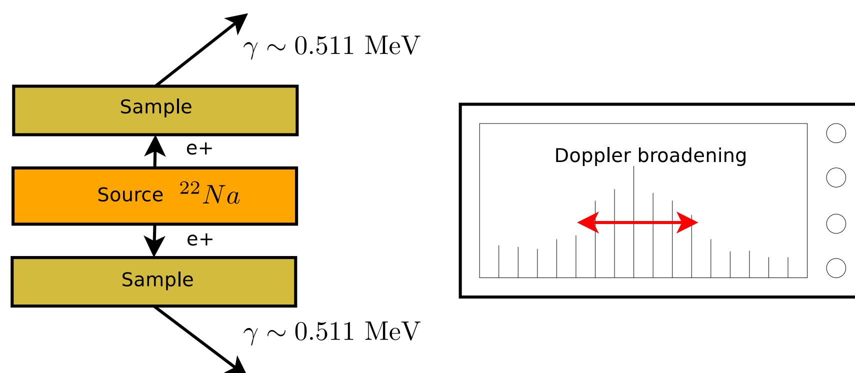

Figure 7.3: Positron doppler broadering spectroscopy scheme at sandwich geometry

7.3.4 Positron back diffusion measurement

Positron back diffusion measurement was performed on a continuous magnetically guided slow positron beam with energy of incident positrons adjustable in the range from 0.05 to 30 keV. Doppler broadening of the annihilation photopeak was measured by a HPGe detector with the relative efficiency of 35% and the energy resolution of (1.08 ± 0.01) keV at 511 KeV. Shape of Doppler broadened annihilation photopeak was characterized using the S (sharpness) parameter.[132] The dependence of of the S parameter on positron energy was fitted using the VEPFIT code.[133]

7.3.5 Glow Discharge Mass Spectrometry (GDMS)

Glow Discharge Mass Spectrometry (GDMS) was used for the chemical analysis of as-grown samples. The concentrations of elements exceeding 10^{15}cm^{-3} for u-CdTe, CdTe:Cl and CdZnTe:Ge presented in Table 7.1 in units 10^{15}cm^{-3}. A 30% error of GDMS analysis was declared.

Table 7.1: The concentrations of elements exceeding 10^{15}cm^{-3} for u-CdTe, CdTe:Cl and CdZnTe:Ge established by GDMS in units 10^{15}cm^{-3}. A 30% error of GDMS analysis was declared.

Sample	B	Mg	Al	Si	P	S	Cl	Ca	Au	Cr	Ni	Cu	Zn	Ge	Se	Ag	In	Sn
u-CdTe							1						2		2	2	1	1
CdTe:Cl		1	1	1		5	183		1			3	3					
CdZnTe:Ge	3	5	3	3	1	8		1	7	20	3	1	3.5%	60	12			

7.4 Theory

Positron properties were calculated using density functional theory (DFT) within so-called standard scheme.[134] In this approximation positron density is assumed to be everywhere vanishingly small and not affecting the bulk electron structure. At first electron density $n(\mathbf{r})$ in the material is solved without the positron. Subsequently, the effective potential for positron is constructed as

$$V_{+}(\mathbf{r}) = \phi(\mathbf{r}) + V_{\text{corr}}(n(\mathbf{r})), \tag{7.7}$$

where $\phi(\mathbf{r})$ is the Coulomb potential produced by the charge distribution of electrons and nuclei and $V_{\text{corr}}(n(\mathbf{r}))$ is the zero positron density limit of the electron-positron correlation potential.[134] Positron wave functions $\psi_i^{+}(\mathbf{r})$ were calculated by solution of a single particle Schrödinger equation

$$-\frac{1}{2}\nabla^2\psi_i^{+}(\mathbf{r}) + V_{+}(\mathbf{r})\psi_i^{+}(\mathbf{r}) = E_i\psi_i^{+}(\mathbf{r}), \tag{7.8}$$

where E_i is the energy eigenvalue for i-th positron state. In the present calculations we considered the positron ground state only.

The positron annihilation rate (i.e. the inverse of positron lifetime) is determined using the expression

$$\lambda = \pi r_e^2 c \int |\psi^{+}(\mathbf{r})|^2 n(\mathbf{r})\gamma[n(\mathbf{r}), \nabla n(\mathbf{r})]\, d\mathbf{r}, \tag{7.9}$$

where r_e is the classical electron radius, c is the speed of light, and γ denotes the electron enhancement factor describing the pileup of electrons at the positron site.[134]

The electron-positrons correlation, i.e. the correlation potential $V_{\text{corr}}(n(\mathbf{r}))$ and the enhancement factor γ, were treated by two approaches:

(i) local density approximation (LDA) utilizing the parametrization by Boroński and Nieminen[135] and taking into account incomplete positron screening[136] using a high frequency dielectric constant of $\epsilon_\infty = 7.1$[137] and

(ii) generalized gradient approach (GGA) within the approach introduced by Barbiellini et al.[138]

The electron density $n(\mathbf{r})$ was constructed by superposition of atomic electronic densities calculated by a relativistic atomic code.[139] This approach called atomic superposition (ATSUP)[140] neglects the charge transfer, but it is computationally feasible and can be used even for very large supercells retaining full 3-D geometry of the problem. In the following text the approach employing LDA and GGA scheme with superimposed electron density is denoted ATSUP-LDA and ATSUP-GGA, respectively.

The ATSUP-LDA and ATSUP -GGA calculations of positron parameters were performed on $8 \times 8 \times 8$ supercells containing 2048 Cd and 2048 Te atoms. Defects were modelled by removing the corresponding number of atoms from the supercell. Integration

over the Brillouin-zone described in Ref. autociteKorhonen96 was used in calculations of positron parameters for defects.

It is well known that LDA overestimates positron annihilation rates especially with d electrons[138] and the lifetimes calculated within the LDA approach are often shorter than the values measured in experiment. This shortcoming is to some extend compensated when LDA approach is used with electron density constructed by ATSUP.[140,141] On the other hand, the GGA approach when used with ATSUP electron density gives often lifetimes which are longer than the experimental values.[142] Hence, the lifetimes calculated using the LDA and the GGA approach can be considered as a lower and an upper bound of the interval where the actual lifetime falls. The GGA scheme is more sensitive to details of electronic structure than LDA[138] and the lifetimes calculated using the GGA approach are it the best agreement with experiment when used with a self-consistent electron density. For these reasons we performed also self-consistent electron density calculations for selected positron states. The self consistent valence electron density was calculated by the plane wave code VASP (Vienna ab-inito simulation package)[143,144] using projector augmented wave (PAW) potentials.[145] The $5s^2$, $4d^{10}$ Cd electrons and $5s^2$, $5p^4$ Te electrons were considered as valence electrons in the VASP calculations. The calculations were performed using 216 atoms based supercells and $2\times2\times2$ k-point grids generated using the Monkhorst-Pack scheme.[146] The wave functions were expanded in a plane wave basis with the cut-of energy of 277 eV. The calculated CdTe lattice constant a = 6.60 Å is in a reasonable agreement with the experimental value of 6.48 Å. Ionic relaxations were not considered at the present stage of calculations. In construction of the positron potential the frozen core electron orbitals were added to the self-consistent valence electron density calculated by VASP. In the following text this approach is denoted VASP-GGA.

The momentum distribution of annihilating pairs was calculated employing the ATSUP-based approach described in Refs. [147, 148]. The electron-positron correlations were treated within the GGA approach. The contribution $\varrho^{i,nl}(p)$ from the $i-$th atom and a shell characterized by principal (n) and orbital (l) quantum numbers is calculated by the formula

$$\varrho^{i,nl}(p) = 4\pi^2 r_e^2 c N^{i,nl} \gamma^{i,nl} \left| \int R_+^i(r) R_-^{i,nl}(r) B_l(pr) r^2 dr \right|^2 \quad (7.10)$$

where $N^{i,nl}$ denotes the number of electrons in the (n,l) shell, B_l is the spherical Bessel function and $R_-^{i,nl}$ and R_+^i denotes the electron and positron radial wave functions. The symbol $\gamma^{i,nl}$ stands for the state-dependent positron enhancement factor.[148] The momentum distribution of the annihilating electron-positron pairs is obtained by summing the partial contributions $\varrho^{i,nl}(p)$ over all occupied atomic sites and corresponding electron shells. Core electrons localized in atomic shells are practically not affected by crystal bonding. Hence, the ATSUP-based approach describes well the high momentum part of the momentum distribution where the contribution of positrons annihilated by core electrons dominates. But since it neglects the charge transfer it fails to describe properly the low momentum part of the momentum distribution defined by positrons annihilated by low momentum valence electrons.

In order to mimic the effect of the finite resolution of the experimental setup, the theoretical momentum distribution curves were convoluted with a Gaussian with FWHM of 4.0×10^{-3} m_0c. To highlight the high momentum part of momentum distributions where the contribution of core electrons dominates the calculated momentum distributions are presented as ratio curves related to a perfect CdTe crystal.

7.5 Results and Discussion

7.5.1 Galvanomagnetic measurements

The galvanomagnetic properties of as-grown u-CdTe, CdTe:Cl and CdZnTe:Ge and annealed CdTe:Cl and CdZnTe:Ge samples are summarized in Table 7.2. The properties of u-CdTe accord with its growth at Cd overpressure, where the V_{Cd}-related defects are suppressed and the electron density is afforded by residual noncompensated donors. The as-grown CdTe:Cl and CdZnTe:Ge samples exhibit rather high resistivity, which is typical for the growth of Te-rich materials, where excess donors dominating above shallow acceptors are compensated by V_{Cd}.[22,45]

Annealing in Cd vapour leads to a decrease in resistivity for both samples. CdTe:Cl exhibited n-type conductivity due to the suppressed V_{Cd} and dominating shallow donors $\mathrm{Cl_{Te}}$. The free carrier concentration of $\sim 10^{17}\,\mathrm{cm}^{-3}$ therefore gives a lower limit for the concentration of Cl dopants in the sample.[67] Cd vapour annealing of CdZnTe:Ge yield p-type conductivity contrary to CdTe:Cl. Such a behaviour is well known in annealed undoped or weakly doped CdTe/CdZnTe[149], where acceptor-like impurities are dominant after annealing. In our CdZnTe:Ge, the extrinsic shallow donor ((B)+(Al)) and shallow acceptor ((P)+(Au)+(Cu)) densities are similar, and weak excess acceptor contamination is assumed. Subsequent annealing in Te vapour produced p-type conductivity in both samples. This is in agreement with expected V_{Cd} formation. This results correspond with chapters 3 and 4.

Table 7.2: Summary of galvanomagnetic measurements: resistivity of samples, type of conductivity and concentration of free carriers.

Sample	Treatment	Resistivity (Ω cm)	Type	Concentration (cm^{-3})
u-CdTe	as-grown	5.5	n	1.1×10^{15}
CdTe:Cl	as-grown	7.3×10^{7}	p	1.5×10^{10}
	Cd-annealed	4.9×10^{-2}	n	9.7×10^{16}
	Te-annealed	6.9×10^{3}	p	8.5×10^{12}
CdZnTe:Ge	as-grown	1.8×10^{9}	n	6.1×10^{6}
	Cd-annealed	3.0×10^{4}	p	3.2×10^{12}
	Te-annealed	2.5×10^{3}	p	4.0×10^{13}

7.5.2 Calculated positron lifetimes

Positron lifetimes, calculated using ATSUP-LDA, ATSUP-GGA and VASP-GGA methods for various positron states in CdTe are listed in Table 7.3. Theoretical positron lifetimes available in literature are shown in Table 7.3 as well. The positron lifetimes calculated using the ATSUP-LDA and ATSUP-GGA schemes in the present work are in an excellent agreement with the lifetimes calculated in Refs. [121, 150] One can see in Table 7.3 that positron lifetimes calculated using various approaches for the electron-positron correlation, i.e. the enhancement factor and the electron-positron correlation potential, are differ. The positron lifetimes calculated using the LDA approach are always lower than those obtained by the GGA scheme. Moreover, calculated positron lifetimes vary depending whether superimposed or self-consistent electron density was used in the calculation.

Table 7.3: Theoretical positron lifetimes for a perfect CdTe crystal and various defects calculated various approaches. Theoretical lifetimes available in literature are shown in the table as well.

positron state	ATSUP -LDA (ps)	ATSUP -GGA (ps)	VASP -GGA (ps)	ATSUP -LDA Ref. [121] (ps)	ATSUP -LDA Ref. [150] (ps)	ATSUP -GGA Ref. [121] (ps)
bulk	276	307	291	276	276	309
V_{Cd}	289	323	325	291	288	322
$V_{Cd}Te_{Cd}$	287	315				
$V_{Cd}Ge_{Cd}$	290	323				
A_C	306	331	330			
$V_{Cd}2Cl_{Te}$	316	346				
$(V_{Cd}2Cl_{Te})_2$ cluster	319	365				
$(V_{Cd}2Cl_{Te})_3$ cluster	338	401				
$(V_{Cd}2Cl_{Te})_4$ cluster	351	427				

The bulk positron lifetime for CdTe calculated using the ATSUP-LDA method is τ_B = 276 ps, while the ATSUP-GGA scheme yielded higher bulk lifetime τ_B = 307 ps. For comparison experimental lifetimes reported in literature for CdTe are listed in Table 7.4. The experimental bulk positron lifetimes for CdTe reported in literature fall into the range from 280 to 291 ps.[119–122,124,151,152] The VASP-GGA scheme which can be considered as the most precise approach used here yielded the CdTe bulk positron lifetime τ_B = 291 ps which is comparable with the experimental values.

In order to compare positron lifetimes for various defects with the experimental values we use ratios τ_D/τ_B of the calculated lifetime τ_D to the bulk lifetime τ_B calculated by the same approach. These ratios are listed in Table 7.5.

The differences between various theoretical schemes are to a large extend cancelled using τ_D/τ_B ratios and the τ_D/τ_B values exhibit relatively low sensitivity to the approach used for electron-positron correlation[138,153].

Table 7.4: Experimental positron lifetimes for a perfect CdTe crystal and selected defects reported in literature. The τ_D/τ_B ratio is shown in the table for positrons trapped at defects. Note that in the ratios the lifetime of trapped positrons was always related to the bulk lifetime measured on the same setup, i.e. τ_D values were divided by τ_B ones published by the same authors. The uncertainties (one standard deviations) are given in parentheses in the units of the last significant digit.

positron state	lifetime (ps)	τ_D/τ_B	reference	note
bulk	280(1)		[119]	
	283(1)		[151]	
	285(1)		[122, 124]	In-doped
	287(1)		[120]	
	290(4)		[121]	CdTe film
	291(1)		[152]	
V_{Cd}	325(5)	1.15(2)	[124, 151]	electron irradiated
	320(2)	1.123(7)	[122, 124]	In-doped
	323(3)	1.13(1)	[120]	In-doped
	321(9)	1.11(3)	[121]	CdTe film
A_C	330(10)	1.18(3)	[119]	Cl-doped

While V_{Te} is believed to be positively charged in CdTe, V_{Cd} is either neutral (V^0_{Cd}) or negatively charged (V^-_{Cd}, V^{2-}_{Cd}) depending on the Fermi level position.[40] Hence, positrons are repelled by V_{Te} while V_{Cd} represent trapping sites for positrons. This is illustrated in Fig. 7.4(c) shown the positron density in the (001) plane calculated by the ATSUP-GGA approach. Fig. 7.4(a) shows the positron density in a perfect CdTe crystal where positron is de-localized in the lattice. The positron density calculated for a CdTe crystal containing V_{Cd} is plotted in Fig. 7.4(b). Clearly the positron is localized in V_{Cd}. Experimental evidence for positron trapping in V_{Cd} has been reported by many authors[120–122,124,151].

Table 7.5: Theoretical τ_D/τ_B ratios for positrons trapped at various defects in CdTe calculated by various approaches. Theoretical τ_D/τ_B ratios available in literature are shown in the table as well.

positron state	ATSUP -LDA	ATSUP -GGA	VASP -GGA	ATSUP -LDA Ref. [121]	ATSUP -LDA Ref. [150]	ATSUP -GGA Ref. [121]
V_{Cd}	1.05	1.05	1.12	1.05	1.04	1.04
$V_{Cd}Te_{Cd}$	1.04	1.03				
$V_{Cd}Ge_{Cd}$	1.05	1.05				
A_C	1.11	1.08	1.13			
$V_{Cd}2Cl_{Te}$	1.14	1.13				
$(V_{Cd}2Cl_{Te})_2$ cluster	1.16	1.19				
$(V_{Cd}2Cl_{Te})_3$ cluster	1.22	1.31				
$(V_{Cd}2Cl_{Te})_4$ cluster	1.27	1.39				

The lifetimes of positrons trapped V_{Cd} determined experimentally fall into the range from 320 to 325 ps which corresponds to τ_D/τ_B falling into the interval 1.11 - 1.15, see Table 7.4. The ATSUP-LDA and ATSUP-GGA calculations for positrons trapped at V_{Cd} resulted in $\tau_D/\tau_B = 1.05$, which is remarkably lower than the experimental values. On the other hand, the VASP-GGA approach yielded $\tau_D/\tau_B = 1.12$ which is close to the values measured in experiment. This indicates that charge transfer which was neglected in ATSUP calculations leads to a slight decrease of electron density in V_{Cd} and consequently an increase of the lifetime of trapped positrons.

Positron lifetime was calculated also for V_{Cd} associated with Te anti-site Te_{Cd} and with various impurities. One can see in Table 7.3 that Te_{Cd} causes shortening of positron lifetime. A Ge_{Cd}^{2+} donor associated with V_{Cd}^{2-} acceptor forms $V_{Cd}^{2-}Ge_{Cd}^{2+}$ complex which is electrically neutral. Theoretical calculations revealed that positrons trapped at $V_{Cd}^{2-}Ge_{Cd}^{2+}$ complexes exhibit practically the same lifetime as V_{Cd}. Hence, these two kinds of defects cannot be distinguished by measurement of positron lifetime.

In Cl doped CdTe V_{Cd}^{2-} may couple with Cl_{Te}^{-} shallow donors forming negatively charged $(V_{Cd}Cl_{Te})^{-}$ complexes called A-centres (A_C) or neutral $V_{Cd}2Cl_{Te}$ complexes. Results in Table 7.3 indicate that replacement of Te nearest neighbours of V_{Cd} by Cl atoms increases the lifetime of trapped positron. This effect is caused by smaller size of Cl atoms compared to Te ones. Hence replacement of a Te nearest neighbour of V_{Cd} by a Cl impurity increases the open volume of vacancy. This is illustrated in Fig. 7.4, which presents calculated positron density in the (001) plane for a positron trapped at A_C defect. One can see in the figure that positron density in A_C becomes asymmetric since it expanded towards the Cl nearest neighbour.

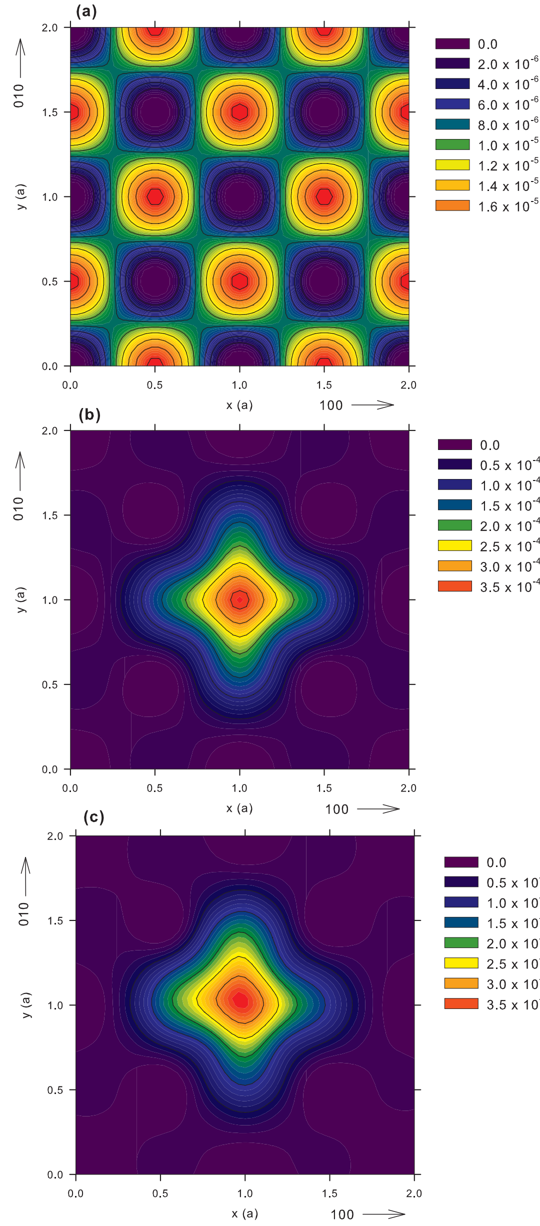

Figure 7.4: Positron density in the (001) plane calculated using the ATSUP-GGA approach: (a) perfect CdTe crystal, (b) CdTe crystal containing V_{Cd} in 1,1,0 position, (c) CdTe crystal containing A_C defect consisting of V_{Cd} and Cl_{Te} located in 1,1,0 and 0.25,1.75,0.25 position, respectively. The co-ordinates are expressed in the units of the CdTe lattice constant a. Positron density is given in the atomic units.

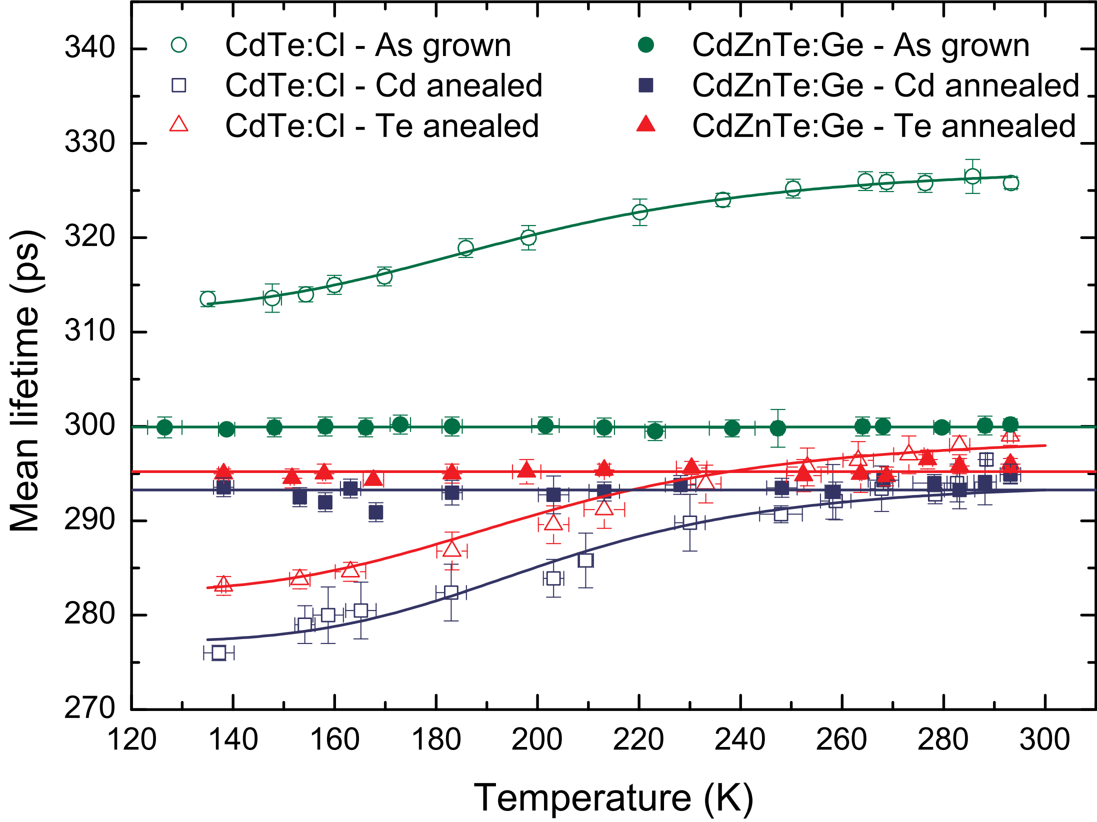

Figure 7.5: Temperature dependence of the mean positron lifetime for CdTe:Cl and CdZnTe:Ge. The lines represent the fit using 3-STM.

7.5.3 Lifetime spectroscopy

The results of LT measurements, i.e. lifetimes τ_i and relative intensities I_i resolved in LT spectra for u-CdTe, CdTe:Cl and CdZnTe:Ge samples, are summarized in Table 7.6 for temperatures 295 and 123 K, respectively. The temperature dependences of the mean positron lifetime $\overline{\tau} = \sum_i \tau_i I_i$ are presented in Fig. 7.5.

Undoped CdTe

The u-CdTe crystal exhibits a single component LT spectrum (except of the source contribution) with lifetime of $\sim$ 290 ps, which fits in the CdTe bulk lifetimes reported in literature, see Table 7.4. Hence, the concentration of positron traps in the u-CdTe crystal is very low (below the sensitivity threshold of LT spectroscopy) and virtually all positrons are annihilated in the de-localized state. Low temperature LT measurements of the u-CdTe crystal yielded practically the same results as the measurement at RT.

Results of positron back-diffusion measurement, i.e. dependence of the S parameter on the energy E of incident positrons in plotted in Fig. 7.6. The positron penetration depth increases with increasing energy of implanted positrons. Hence, at very low energies

virtually all positrons are annihilated at the surface. With increasing energy positrons penetrate deeper into the sample and the fraction of positrons diffusing back to the surface gradually decreases. Finally at high energies virtually all positrons are annihilated in the bulk and the S parameter approaches a plateau. One can see in Fig. 7.6 that the $S(E)$ curve exhibits a maximum at energy around 2 keV. This indicates that the sample contains a thin surface layer of native oxides most probably a mixture of $CdTeO_3$, TeO_2 and CdO.[154,155] The $S(E)$ curve for the u-CdTe sample was fitted by VEPFIT[133] using a two layer model: (i) native oxide layer on the surface and (ii) CdTe bulk region. The model curve calculated by VEPFIT is plotted in Fig. 7.6 by a solid line and is obviously in good agreement with the experimental points. The thickness of the native oxide layer ≈ 30 nm was fitted.

The positron diffusion length determined in the CdTe region is $L_{+,B} = (240 \pm 20)$ nm. This value is comparable with the positron diffusion lengths in defect-free semiconductors.[132] Hence, the u-CdTe crystal contains very low density of positron traps (except of the thin surface oxide layer) and almost all positrons are annihilated from the free state in accordance with the results of positron lifetime characterization. Assuming that the u-CdTe sample contains no positron traps one can calculate the positron diffusion coefficient for u-CdTe from the expression $D_+ = L^2_{+,B}/\tau_B$, where $\tau_B = 290$ ps is the bulk u-CdTe lifetime. This yields the positron diffusion coefficient for u-CdTe $D_+ = 1.98$ cm^{2}s^{-1} which is in very good agreement with the value $D_+ = 2$ cm^{2}s^{-1} reported for CdTe by Neretina et al.[156]

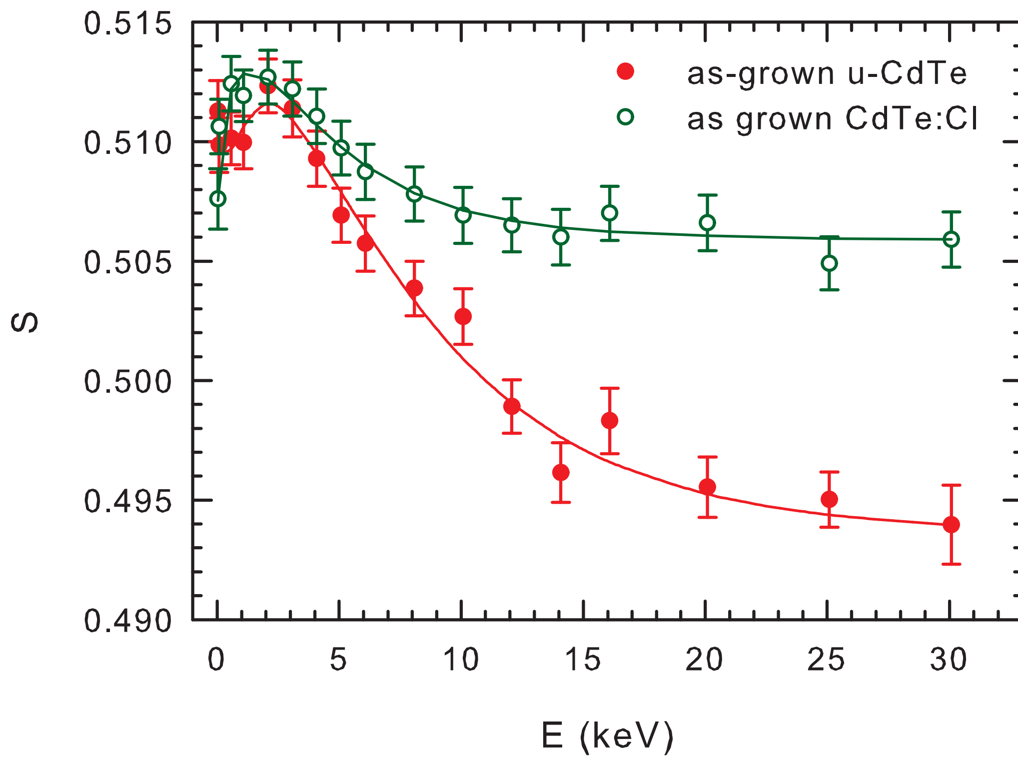

Figure 7.6: The dependence of the S parameter on the energy E of incident positrons for undoped CdTe (full symbols) and CdTe:Cl sample in the as-grown state (open symbols) . Solid lines show model curves calculated by VEPFIT.

CdTe:Cl

The LT spectra of the CdTe:Cl crystal generally consist of up to three components (except of the source contribution) corresponding to the three positron states: (i) free positrons (lifetime τ_1), (ii) positrons trapped in shallow traps (lifetime τ_2, trapping rate K_{d1}), and (iii) positrons trapped in deep traps (lifetime τ_3, trapping rate K_{d2}). The kinetics of positron trapping for these defects is described by the three-state simple trapping model (3-STM).[132] The rate equations for such system read[132]

$$\begin{aligned} \frac{\mathrm{d}n_f}{\mathrm{d}t} &= -(\tau_B^{-1} + K_{d1} + K_{d2})n_f(t) + \delta_{d1}n_{d1}(t) \\ \frac{\mathrm{d}n_{d1}}{\mathrm{d}t} &= -(\tau_{d1}^{-1} + \delta_{d1})n_{d1}(t) + K_{d1}n_f(t) \\ \frac{\mathrm{d}n_{d2}}{\mathrm{d}t} &= -\tau_{d2}^{-1}n_{d2}(t) + K_{d2}n_f(t) \end{aligned} \tag{7.11}$$

with the initial conditions $n_f(0) = 1$ and $n_{d1}(0) = n_{d2}(0) = 0$. The symbols $n_B(t)$, $n_{d1}(t)$ and $n_{d2}(t)$ denote the probabilities that a positron is at time t de-localized in the free state or trapped in a shallow or deep trap, respectively. K_{d1} and K_{d2} stand for the positron trapping rates for the shallow and the deep traps, respectively, and δ_{d1} is the de-trapping rate from the shallow traps. The lifetimes of positrons trapped at the shallow and the deep traps, i.e. inverse of the annihilation rates of trapped positrons, are denoted τ_{d1} and τ_{d2}, respectively. The visualization of 3-STM is showed at Fig. 7.7.

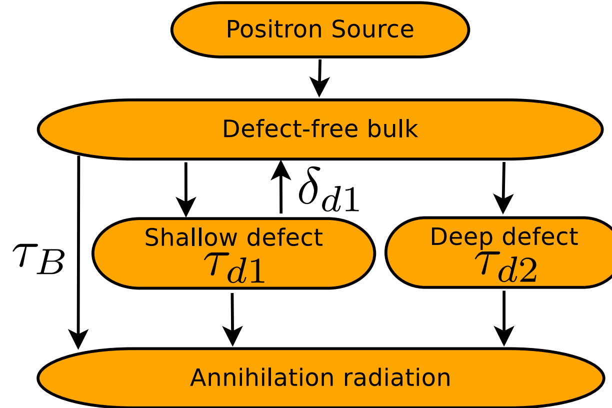

Figure 7.7: 3-STM positron trapping model, which containing a lifetimes of positrons trapped at the shallow (τ_{d1}), the deep traps (τ_{d2}), bulk lifetime (τ_B) and δ_{d1} is the de-trapping rate from the shallow traps.

Solution of the differential equations (7.11) gives the decay spectrum of positrons

$$Q_{3-STM}(t) = \sum_{i=1}^{3} I_i e^{-\frac{t}{\tau_i}}, \tag{7.12}$$

where

$$\begin{aligned}
\tau_1 &= \frac{2}{\Lambda + \Xi}, \quad \tau_2 = \frac{2}{\Lambda - \Xi}, \quad \tau_3 = \tau_{d2}, \\
I_1 &= 1 - (I_2 + I_3) \qquad (7.13) \\
I_2 &= \frac{\delta_{d1} + \tau_{d1}^{-1} - \frac{1}{2}(\Lambda - \Xi)}{\Xi} \left[1 + \frac{K_{d1}}{\delta_{d1} + \tau_{d1}^{-1} - \frac{1}{2}(\Lambda - \Xi)} + \frac{K_{d2}}{\tau_{d2}^{-1} - \frac{1}{2}(\Lambda - \Xi)} \right] \\
I_3 &= \frac{K_{d2}(\delta_{d1} + \tau_{d1}^{-1} - \tau_{d2}^{-1})}{\left[\tau_{d2}^{-1} - \frac{1}{2}(\Lambda + \Xi)\right]\left[\tau_{d2}^{-1} - \frac{1}{2}(\Lambda - \Xi)\right]}
\end{aligned}$$

and

$$\begin{aligned}
\Lambda &= \tau_B^{-1} + K_{d1} + K_{d2} + \tau_{d1}^{-1} + \delta_{d1} \qquad (7.14) \\
\Xi &= \sqrt{(\tau_B^{-1} + K_{d1} + K_{d2} - \tau_{d1}^{-1} - \delta_{d1})^2 + 4\delta_{d1}K_{d1}}.
\end{aligned}$$

The LT spectrum $S_{3-STM}(t)$ is the number of positrons annihilated in various times and is obtained as a negative time derivative of the decay spectrum $Q_{3-STM}(t)$

$$S_{3-STM}(t) = -\frac{\mathrm{d}Q_{3-STM}(t)}{\mathrm{d}t} = \sum_{i=1}^{3} \frac{I_i}{\tau_i} e^{-\frac{t}{\tau_i}}. \qquad (7.15)$$

Hence the lifetimes τ_1, τ_2, τ_3 of the exponential components resolved in experimental LT spectra and their relative intensities I_1, I_2, I_3 can be interpreted within 3-STM using Eqs. (7.13–7.15). Note that for a high concentration of shallow or deep positron traps the lifetime τ_1 becomes extremely short and its intensity I_1 diminishes. In such case it is not possible to resolve the first component in LT spectrum due to limited resolution of LT spectrometer. This situation happened here in the case of low temperature LT spectra for CdTe:Cl. The short lived component could not be resolved in LT spectra due to very high density of shallow traps in this sample as will be shown in the following text.

The probability that a positron trapped in a shallow trap will escape by thermal excitation decreases with falling temperature. Hence the positron de-trapping rate from shallow traps δ_{d1} depends on temperature[157]

$$\delta_{d1}(T) = \frac{K_{d1}}{[c]} \left(\frac{m^* k_B T}{2\pi\hbar^2} \right)^{3/2} \exp\left(-\frac{E_b}{k_B T} \right), \qquad (7.16)$$

where m^* is the effective positron mass,[134] k_B the Boltzmann constant, $[c]$ the concentration of shallow traps, and E_b the positron binding energy to the shallow traps. The temperature dependence of the mean lifetime $\overline{\tau} = \sum_{i=1}^{3} \tau_i I_i$ was fitted using 3-STM with K_{d1}, K_{d2}, $[c]$ and E_b as fitting parameters. If the sample contains shallow traps, then the mean positron

lifetime $\overline{\tau}$ varies with temperature due to the temperature dependence of δ_{d1}. Fig. 7.5 shows that $\overline{\tau}$ for CdTe:Cl decreases with temperature, which testifies to the presence of shallow traps in this sample. The temperature dependence of $\overline{\tau}$ can be explained by the formation of series of attractive shallow Rydberg states connected with negatively-charged defects.[158,159] Since the positron binding energy of the shallow Rydberg states is rather small (typically ≤ 0.1 eV), they act as efficient positron traps at low temperatures only where the positron may not escape by thermal excitation.[158]

Hence, to describe LT spectra measured at RT 3-STM can be simplified by elimination of the shallow traps, i.e. by setting $K_{d1} = \delta_{d1} = 0$, $n_{d1}(t) \equiv 0$ in Eqs. (7.11–7.15). This leads to the following rate equations

$$\begin{aligned}\frac{\mathrm{d}n_f}{\mathrm{d}t} &= -(\tau_B^{-1} + K_{d2})n_f(t) \qquad (7.17)\\ \frac{\mathrm{d}n_{\mathrm{d2}}}{dt} &= -\tau_{d2}^{-1}n_{d2}(t) + K_{d2}n_f(t)\end{aligned}$$

This simplified trapping model called two-state simple trapping model (2-STM) was used for analysis of the LT spectra measured at RT. The solution of 2-STM with the initial conditions $n_f(0) = 1$ and $n_{d2}(0) = 0$ is two-component decay spectrum of positrons

$$Q_{2-STM}(t) = I_1 e^{-\frac{t}{\tau_1}} + I_3 e^{-\frac{t}{\tau_3}}, \qquad (7.18)$$

where

$$\begin{aligned}\tau_1 &= \left(\tau_B^{-1} + K_{d2}\right)^{-1}, \quad \tau_3 = \tau_{d2}, \qquad (7.19)\\ I_1 &= 1 - I_3, \quad I_3 = \frac{K_{d2}}{\tau_B^{-1} - \tau_{d2}^{-1} + K_{d2}}.\end{aligned}$$

The LT spectrum $S_{2-STM}(t)$ predicted by 2-STM is

$$S_{2-STM}(t) = -\frac{\mathrm{d}Q_{2-STM}(t)}{\mathrm{d}t} = \frac{I_1}{\tau_1} e^{-\frac{t}{\tau_1}} + \frac{I_3}{\tau_3} e^{-\frac{t}{\tau_3}}. \qquad (7.20)$$

Decomposition of LT spectrum of the as-grown CdTe:Cl measured at RT revealed two exponential components, see Table 7.6. The shorter component with lifetime $\tau_1 = 230(2)$ ps represents a contribution of free positrons. Note that τ_1 is shorter than the bulk positron lifetime for CdTe due to parallel positron annihilation and trapping in the deep traps, c.f. Eq (7.19).

Table 7.6: Results of LT studies: lifetime τ_i and the relative intensity I_i of the exponential components resolved in the LT spectra evaluated at 295 K and 123 K. The uncertainties (one standard deviations) are given in parentheses in the units of the last significant digit.

sample	treatment	T (K)	τ_1 (ps)	I_1 (%)	τ_2 (ps)	I_2 (%)	τ_3 (ps)	I_3 (%)
u-CdTe	as-grown	295	292(1)	100	–	–	–	–
		123	290(1)	100	–	–	–	–
CdTe:Cl	as-grown	295	230(2)	45(1)	–	–	405(2)	55(1)
		123	–	–	281(9)	94(5)	400(10)	6(2)
	Cd-annealed	295	283(8)	81(5)	–	–	328(7)	19(5)
		123	–	–	280(10)	98(5)	330(10)	2(1)
	Te-annealed	295	240(10)	22(5)	–	–	316(6)	78(5)
		123	–	–	278(8)	93(5)	320(10)	7(3)
CdZnTe:Ge	as-grown	295	263(9)	42(1)	–	–	327(8)	58(1)
		123	260(9)	37(4)	–	–	326(8)	63(1)
	Cd-annealed	295	295.0(4)	100	–	–	–	–
		123	293.0(5)	100	–	–	–	–
	Te-annealed	295	260(10)	40(5)	–	–	320(5)	60(10)
		123	253(8)	45(5)	–	–	325(5)	55(8)

The lifetime $\tau_3 = 405(2)$ ps, $\tau_3/\tau_B = 1.387(6)$, of the longer component is significantly higher than the positron lifetime for single vacancies in CdTe, see Table 7.3. Hence, we deduce that positrons in the as-grown CdTe:Cl are trapped in larger point defects with the open volume comparable with that of several vacancies. The positron trapping rate to these vacancy clusters can be calculated within 2-STM from Eqs. (7.19)

$$K_{d2} = \frac{I_3}{I_1}(\tau_B^{-1} - \tau_3^{-1}). \tag{7.21}$$

The concentration of vacancy clusters is directly proportional to the trapping rate K_{d2} determined by 2-STM, $[c] = K_{d2}/\nu_{cluster}$. The specific positron trapping rate for the vacancy clusters was estimated as $\nu_{cluster} \approx n_v \nu_v$, where $\nu_v \approx 5 \times 10^{14}$ s^{-1} is the specific positron trapping rate for neutral vacancies in semiconductors[132] and $n_v \approx 4$ is the average number of vacancies constituting the cluster. The latter value was estimated by comparison of the ratio $\tau_3/\tau_B = 1.387(6)$ determined experimentally with the theoretical calculations of clusters of the neutral $V_{Cd}2Cl_{Te}$ complexes of various sizes in Table 7.5.

Extended investigations of CdTe:Cl with chlorine content from 100 to 3000 ppm performed by Krause-Rehberg et al.[119] revealed two components in LT spectra measured at RT: (i) the shorter component, with a lifetime of 330(10) ps, $\tau_3/\tau_B = 1.18(3)$, which was attributed to $A_C \equiv (V_{Cd}Cl_{Te})^-$ and (ii) a long-lived component with a lifetime of 450(15) ps, $\tau_3/\tau_B = 1.61(3)$, which was assigned to clusters of $(V_{Cd}2Cl_{Te})$ neutral complexes. The concentration of both defects increased with Cl content, testifying that they are associated with chlorine. Our CdTe:Cl sample exhibits a smaller lifetime τ_3 than 450 ps. This could be due to significantly lower Cl concentration leading to the formation of $V_{Cd}2Cl_{Te}$ clusters of smaller size.

The analysis of the LT spectrum of the as-grown CdTe:Cl measured at 123 K revealed a new component with lifetime $\tau_2 = 281(9)$ ps, which is slightly shorter than the bulk positron lifetime (290 ps) and dominates the spectrum with 94% intensity, see Table 7.4. Taking into account the temperature dependence of $\overline{\tau}$ in Fig. 7.5, this component obviously comes from positrons trapped in the shallow Rydberg states associated with negatively-charged A-centres (A_C^R). Indeed, the positron binding energy $E_b = (0.09 \pm 0.05)$ eV determined from fitting of the temperature dependence of $\overline{\tau}$ falls into the range $0.01 - 0.10$ eV expected for the Rydberg states.[160] Evidently, $[A_C] \approx [A_C^R]$. The concentration $[A_C^R]$ obtained from fitting of LT data by 3-STM is presented in Table 7.7. From the comparison of K_{d1} with $[c]$ we can estimate the specific positron trapping rate for the shallow traps $\nu_s \sim 4 \times 10^{16}$ s^{-1}. This value falls into the expected range for ν_s calculated in Ref. [158].

Note that Rydberg states are characterized by a lifetime which is close to the bulk lifetime.[158,159] Depending on the local electron density the lifetime of positrons confined at low temperatures in shallow traps can be either slightly higher or lower than the bulk positron lifetime. The latter case has been recently reported for Cu in-diffused GaAs:Te crystals.[161] Low temperature LT studies of Cu in-diffused GaAs:Te revealed shallow traps characterized by a lifetime of 220 ps, which is about of 8 ps shorter than the GaAs bulk lifetime of 228 ps.[161] The shallow traps in Cu-indiffused GaAs:Te were identified as Cu_{Ga} ions coupled with Ga vacancies (V_{Ga}). At RT positrons in the Cu-indiffused GaAs:Te

sample are trapped at deep traps identified as $V_{Ga}Cu_{Ga}$ complexes and characterized by a positron lifetime of 280 ps. At low temperatures positrons are confined predominantly in Rydberg states associated with Cu_{Ga} ions and characterized by a positron lifetime of 220 ps, which is shorter than the bulk lifetime.[161] Thus, it seems that positron trapping in the CdTe:Cl sample is to some extent analogous to that in Cu-indiffused GaAs:Te: at RT positrons are trapped at deep traps (vacancy clusters) while at low temperatures positrons are confined at Rydber states associated with Coulomb field around negatively charged A-centers and characterized by a positrons lifetime ≈ 280 ps, which is about of ≈ 10 ps shorter than the CdTe bulk lifetime of ≈ 290 ps measured on the u-CdTe sample, see Table 7.4. We assume that the reduced lifetime of the positron in the Rydberg state comparing to the bulk lifetime may stem from a lattice relaxation and enhanced mass density in the vicinity of the vacancy, at the radius about 1 nm, where the positrons in Rydberg state mostly occur.

Annealing the CdTe:Cl sample in Cd vapour led to a significant reduction of the intensity of the long-lived defect component and shortening of its lifetime down to $\tau_3 = 328(7)$ ps at RT. The ratio $\tau_3/\tau_B = 1.12(2)$ is close to the value calculated for A_C or single $V_{Cd}2Cl_{Te}$ complex The reduction of this component is clearly caused by the removal of V_{Cd} by Cd annealing and the reduction in cluster size. Ensuing analysis within 2-STM proves the depression of the density of V_{Cd} related defects, see Table 7.7. The Cd-annealed CdTe:Cl is characterized by very low resistivity and n-type conductivity, caused by Cl_{Te}^{+} shallow donors which in contrast to the as-grown sample are not compensated by V_{Cd}^{2-} shallow acceptors. In spite of significant V_{Cd} depreciation the sample measured at low temperature again exhibits a remarkable contribution of A_C^R, see Table 7.6. The temperature dependence of $\overline{\tau}$ plotted in Fig. 7.5 is similar to the as-grown sample just shifted to lower values due to the suppressed contribution from neutral clusters. Since the lifetime of positrons localized in the shallow traps is lower than the CdTe bulk lifetime, $\overline{\tau}$ decreases below the bulk lifetime value at low temperatures where almost all positrons are confined in the shallow traps. Referring to similar concentration of defects at RT and at low temperature, see Table 7.7, we deduce that τ_3 in the Cd-annealed CdTe:Cl sample is associated with A_C only.

Subsequent annealing of a CdTe:Cl sample in Te vapour leads to the appearance of a defect component with lifetime $\tau_3 \approx 316-320$ ps, which corresponds to negatively-charged A_C and neutral $V_{Cd}2Cl_{Te}$ defects. Unlike the as-grown CdTe:Cl crystal, the $V_{Cd}2Cl_{Te}$ complexes formed after Te-annealing are isolated and do not agglomerate into clusters. This could be caused by the fact that during Te-annealing the sample was kept at a lower temperature than during crystal growth, and the mobility of the $V_{Cd}2Cl_{Te}$ complexes was therefore lower. The analysis of LT spectra measured at 123 K revealed that the positron trapping in A_C^R dominates at low temperatures in a similar way as in the Cd-annealed crystal. The temperature dependence of $\overline{\tau}$ presented in Fig 7.5 again shows a drop with decreasing temperature in a similar manner as for the Cd-annealed sample.

Referring to the concentration of defects (Table 7.7), we can deduce that the defects observed at RT in the Te-annealed sample are associated with $V_{Cd}2Cl_{Te}$ and A_C at the total density $[V_{Cd}2Cl_{Te}] + [A_C] = 9 \times 10^{16}$ cm^{-3}. Similarly, the low temperature measurements allow us to establish $[A_C] = [A_C^R] = 2.6 \times 10^{16}$ cm^{-3}, which yields

$[V_{Cd}2Cl_{Te}] = 6.4 \times 10^{16}$ cm^{-3}. Consequently, the calculation of the total Cl density in V_{Cd}-related complexes provides $[Cl]_C = 1.54 \times 10^{17}$ cm^{-3}. This result is very close to the concentration of chlorine determined by GDMS ($[Cl] = 1.8 \times 10^{17}$cm^{-3}). Since GDMS analysis is affected by up to 30% error, we consider this finding as an excellent confirmation of our assignment of defects.

Similar estimation can be done also for the as-grown CdTe:Cl sample where the concentration of $V_{Cd}2Cl_{Te}$ clusters of 1.5×10^{16} cm^{-3} was estimated in Table 7.7. Assuming that each cluster consists on average of 4 $V_{Cd}2Cl_{Te}$ complexes (as deduced from the ratio $\tau_3/\tau_B = 1.387$) the concentration of Cl contained in $V_{Cd}2Cl_{Te}$ clusters is 1.2×10^{17} cm^{-3}. At the same time the low temperature measurement of the same sample yielded $[A_C^R] = 1.9 \times 10^{16}$ cm^{-3}. Hence, the total concentration of Cl in V_{Cd}-related complexes the as-grown CdTe:Cl is $[Cl]_C = 1.39 \times 10^{17}$ cm^{-3}. Again this value is in very reasonable agreement with the total Cl density determined by GDMS.

The as-grown CdTe:Cl crystal was characterized also by positron back-diffusion measurement on the slow positron beam. The dependence of the S-parameter on the energy E of incident positrons for the as-grown CdTe:Cl crystal is plotted in Fig. 7.6. Obviously the $S(E)$ curve for the as-grown CdTe:Cl sample exhibits similar features as the curve for the u-CdTe crystal, namely a maximum at low energies (≈ 2 keV) followed by a gradual decrease down to a plateau value at high energies where virtually all positrons are annihilated inside the CdTe:Cl region. However the plateau value at high energies for the as-grown CdTe:Cl sample is remarkably higher than that for the u-CdTe. The $S(E)$ curve was fitted in the similar manner as the curve for u-CdTe sample, i.e. using a two-layer model consisting of a thin surface oxide layer and the bulk CdTe:Cl region. The model curve calculated by VEPFIT[133] is plotted by solid line in Fig. 7.6 and describes the experimental points accurately. The thickness of the oxide layer of ≈ 20 nm obtained from fitting is comparable with that measured in the u-CdTe. The positron diffusion length in the CdTe:Cl region is $L_+ = (206 \pm 8)$ nm. This value is shorter than the positron diffusion length $L_{+,B} = (240 \pm 9)$ nm determined for the u-CdTe. Shortened positron diffusion length and higher S parameters at high energies give clear evidence that the as-grown CdTe:Cl sample exhibits higher density of defects than the u-CdTe. The concentration of defects $[c]$ in the as-grown CdTe:Cl sample can be estimated from shortening of the positron diffusion length using the expression[162]

$$[c] = \frac{1}{\nu \tau_B} \left(\frac{L_{+,B}^2}{L_+^2} - 1 \right), \tag{7.22}$$

where ν is the specific positron trapping rate to defects. From LT studies we know that the as-grown CdTe:Cl sample contains $V_{Cd}2Cl_{Te}$ clusters consisting on average of four V_{Cd}. Assuming $\nu = 4\nu_v$ one gets $[c] = 1.8 \times 10^{16}$ cm^{-3} which is in very reasonable agreement with the concentration of $V_{Cd}2Cl_{Te}$ clusters (1.5×10^{16} cm^{-3}) determined by LT spectroscopy in Table 7.7.

Table 7.7: The concentration of defects calculated from the LT data. The neutral defects at CdTe:Cl and at CdZnTe:Ge, negatively-charged A-centres and shallow Rydberg states associated with negatively-charged A-centres are symbolized by $\mathrm{V_{Cd}2Cl_{Te}}$, $\mathrm{V_{Cd}Ge_{Cd}}$, $\mathrm{A_C}$, $\mathrm{A_C^R}$, respectively.

sample	**treatment**	**defect type**	**[c] (cm^{-3})**
u-CdTe	as-grown	–	$< 1 \times 10^{15}$
CdTe:Cl	as-grown	$\mathrm{V_{Cd}2Cl_{Te}}$ cluster	$1.5(1) \times 10^{16}$
		$\mathrm{A_C^R}$	$1.9(3) \times 10^{16}$
	Cd-annealed	$\mathrm{A_C}$	$5(1) \times 10^{15}$
		$\mathrm{A_C^R}$	$7(2) \times 10^{15}$
	Te-annealed	$\mathrm{A_C}$ and $\mathrm{V_{Cd}2Cl_{Te}}$	$9.0(5) \times 10^{16}$
		$\mathrm{A_C^R}$	$2.6(6) \times 10^{16}$
CdZnTe:Ge	as-grown	$\mathrm{V_{Cd}Ge_{Cd}}$	$2.6(2) \times 10^{16}$
	Cd-annealed	–	$< 1 \times 10^{15}$
	Te-annealed	$\mathrm{V_{Cd}Ge_{Cd}}$	$2.7(2) \times 10^{16}$

CdZnTe:Ge

At RT the CdZnTe:Ge as-grown crystal exhibits a defect component with lifetime $\tau_3 = 327(8)$ ps falling into the range $320 - 330$ ps commonly attributed to $\mathrm{V_{Cd}^{2-}}$ shallow acceptors or complexes of $\mathrm{V_{Cd}^{2-}}$ associated with donors, see Table 7.4. The lifetime τ_3 at 123 K is practically the same as in RT, and $\overline{\tau}$ remains constant apart from the statistical scattering in the whole temperature range of 123-295 K, see Fig 7.5. A similar result was observed[123] for undoped CdZnTe. The temperature independence of $\overline{\tau}$ observed in CdZnTe:Ge crystal testifies that (i) the defects responsible for the lifetime τ_3 in this sample are mostly electrically neutral, and (ii) unlike CdTe:Cl, the CdZnTe:Ge crystal does not contain shallow traps in detectable concentration.

Taking into account electrical neutrality of defects and positron lifetime comparable to $\mathrm{V_{Cd}^{2-}}$ the component with the lifetime τ_3 can be attributed to positrons trapped at electrically neutral $\mathrm{V_{Cd}^{2-}Ge_{Cd}^{2+}}$ complexes which are likely formed in CdZnTe:Ge. Table 7.7 shows the concentration of $\mathrm{V_{Cd}^{2-}Ge_{Cd}^{2+}}$ complexes determined as $[c] = K_{d2}/\nu_v$, where K_{d2} is the trapping rate calculated within 2-STM by Eq. (7.21) and $\nu_v \approx 5 \times 10^{14}$ s^{-1} is the specific positron trapping rate for neutral vacancies in semiconductors.[132]

Annealing of CdZnTe:Ge crystal in Cd vapour led to the disappearance of the defect component with lifetime τ_3, and the LT spectrum became single-component with the lifetime $\tau_1 \approx 295$ ps, which is close to the bulk lifetime of 292(1) ps measured in the u-CdTe, see Table 7.6. Hence, virtually all positrons in the Cd-annealed CdZnTe:Ge sample are annihilated in the de-localized state. This result proves that $\mathrm{V_{Cd}}$ annihilation is due to Cd-annealing. Slightly higher value of the bulk positron for CdZnTe:Ge compared to that for u-CdTe could be caused by lower electron density in CdZnTe compared to that in CdTe. Temperature-dependent measurements did not reveal any temperature dependence of LT results for the Cd-annealed CdZnTe:Ge sample, see Fig. 7.5 and Table 7.6, which is in

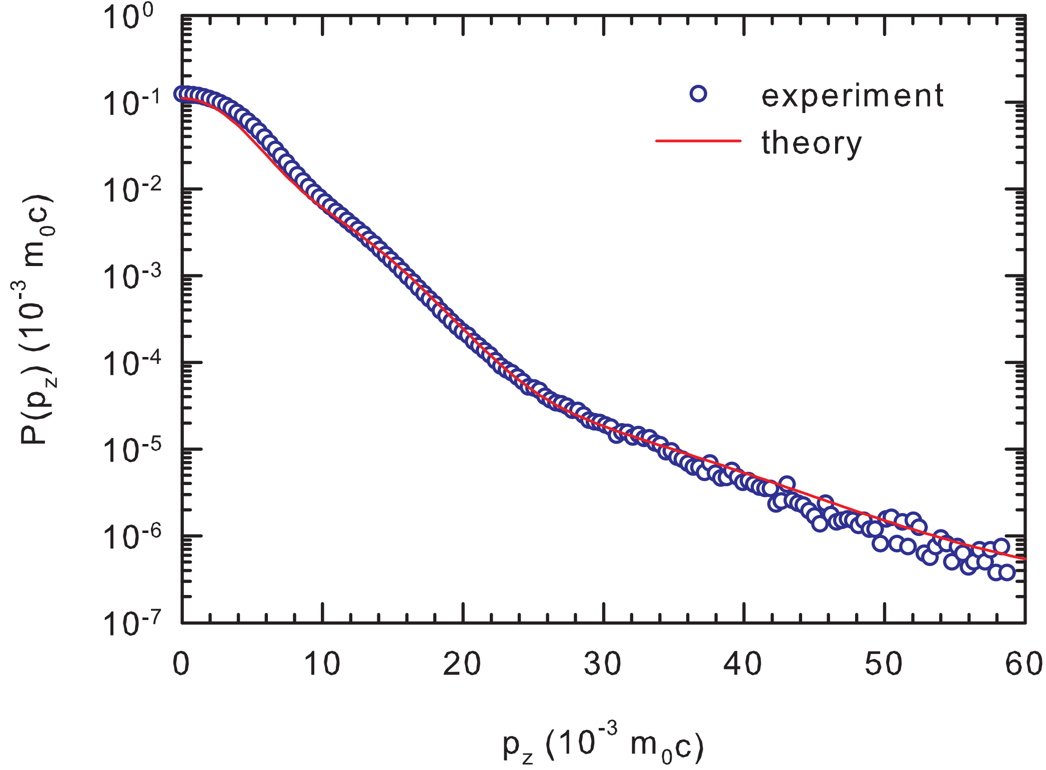

Figure 7.8: The positron annihilation momentum density $P(p_z)$ measured by CDB in the undoped CdTe sample and calculated for a perfect CdTe crystal using the ATSUP-GGA approach.

accordance with the assignment of the τ_1 component to the free positrons.

The subsequent annealing of CdZnTe:Ge in Te vapour resulted in the restoration of the defect component with lifetime $\tau_3 \approx 320$ ps, which shows the re-emergence of V_{Cd}. The LTs obtained after annealing are very similar to those measured in the as-grown CdZnTe:Ge, including the temperature independence of $\overline{\tau}$ in Fig 7.5, which testifies to positron trapping in electrically neutral $V_{Cd}^{2-}Ge_{Cd}^{2+}$ complexes.

7.5.4 CDB spectroscopy

The CDB spectroscopy was employed in order to obtain direct information about chemical environment of V_{Cd} in CdTe:Cl and CdZnTe:Ge crystals. Fig. 7.8 shows the momentum distribution of annihilating electron-positron pairs measured in the u-CdTe reference sample. The calculated momentum distribution for a perfect CdTe crystal is plotted in the figure as well. One can see in the figure that the momentum distribution calculated using

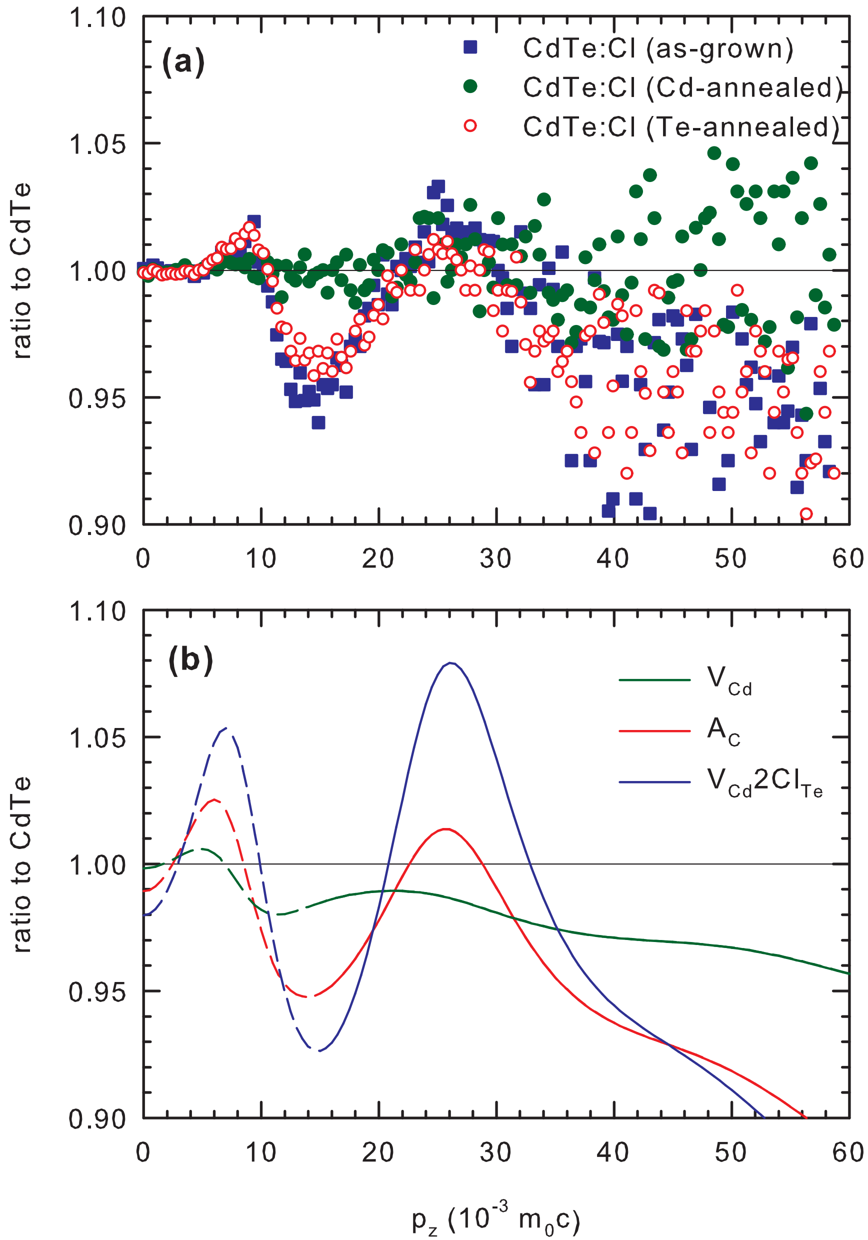

Figure 7.9: The CDB ratio curves (related to defect-free u-CdTe): (a) experimental data for CdTe:Cl in the as-grown state and after annealing in Cd and Te vapour; (b) calculated ratio curves for V_{Cd}, A_C and $V_{Cd}2Cl_{Te}$ defects. The calculated curves are plotted by dashed lines in the low momentum range ($p_z < 15 \times 10^{-3} m_0 c$) where the accuracy of the momentum distribution calculated by ASTUP is poor.

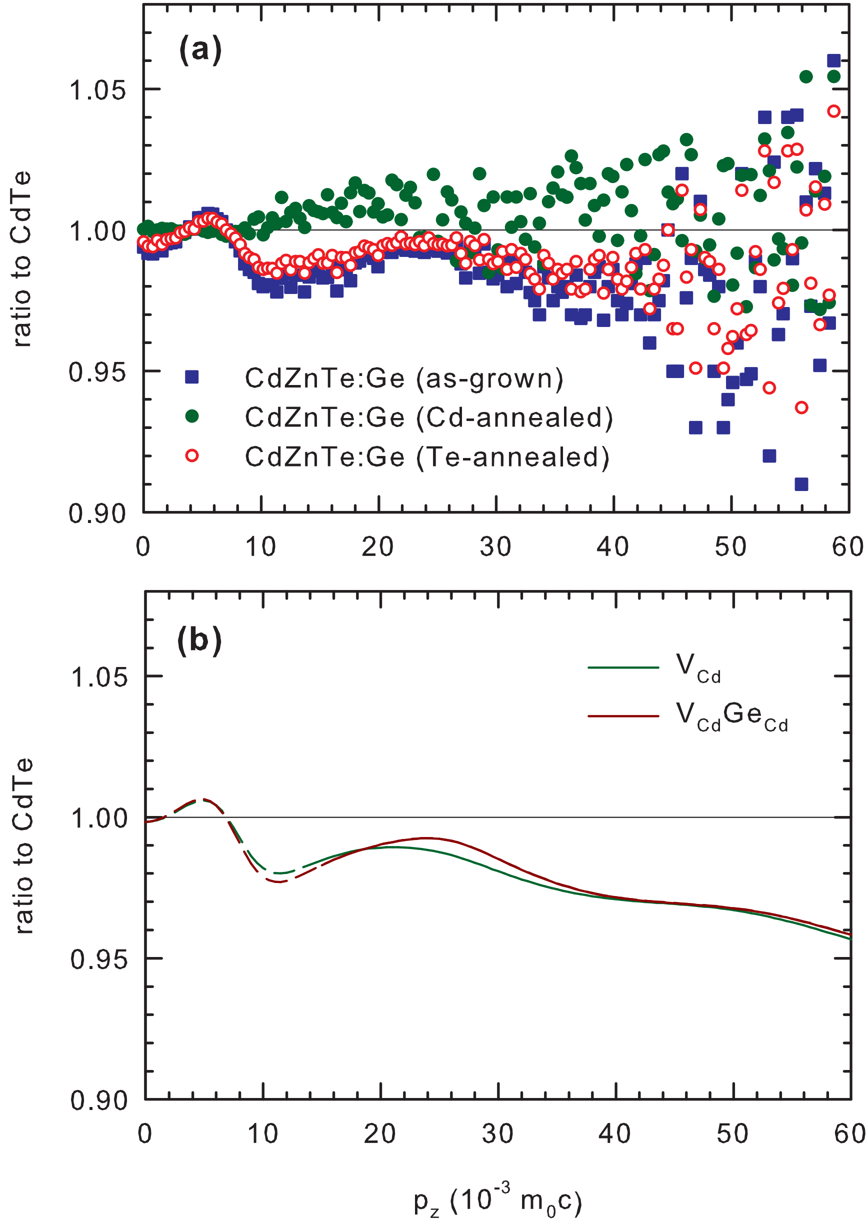

Figure 7.10: The CDB ratio curves (related to defect-free u-CdTe): (a) experimental data for CdZnTe:Ge in the as-grown state and after annealing in Cd and Te vapour; (b) calculated ratio curves for V_{Cd} and $V_{Cd}Ge_{Cd}$ defects. The calculated curves are plotted by dashed lines in the low momentum range ($p_z < 15 \times 10^{-3}\ m_0c$) where the accuracy of the momentum distribution calculated by ASTUP is poor.

the ATSUP-GGA approach agrees well with the experimental points in the high momentum range ($p_z > 15 \times 10^{-3}\ m_0c$) where the contribution of positrons annihilated by core electrons dominates. This is caused by the fact that core electrons in the inner shells retain their atomic character are almost not influenced by crystal bonding. On the other the ATSUP-based approach is not able to describe accurately the momentum distribution in the the low momentum region ($p_z < 15 \times 10^{-3}\ m_0c$) where the contribution of positrons annihilated by valence electrons becomes dominating. For this reason the calculated momentum distributions will be compared with the experimental data in the high momentum region only

Fig. 7.9a shows the experimental CDB ratio curves related to the u-CdTe reference for the CdTe:Cl sample in the as-grown state and after annealing in Cd and Te vapour, respectively. The calculated CDB curves related to a perfect CdTe crystal for V_{Cd}, A_C and $V_{Cd}2Cl_{Te}$ defects are plotted in Fig. 7.9b. From inspection of Fig. 7.9 it becomes clear that the CDB curve for CdTe:Cl annealed in Cd vapour is almost flat (except of statistical scattering) and close to unity in the whole momentum range testifying that the momentum distribution for the Cd-annealed CdTe:Cl is very similar to that in the u-CdTe reference. This confirms the picture that positron traps were removed by annealing in Cd vapour and virtually all positrons in the Cd-annealed sample are annihilated in the free state. On the other hand, the CDB ratio curves for the as-grown CdTe:Cl and the sample annealed in Te vapour clearly differ from unity and exhibit a distinct peak in the high momentum range at $p_z \approx 25 \times 10^{-3}\ m_0c$. Similar peak is observed in the CDB curves calculated for positrons trapped in A_C and $V_{Cd}2Cl_{Te}$ defects in Fig. 7.9b. This testifies to positron trapping in defects associated with chlorine in the as-grown and Te-annealed CdTe:Cl sample.

The CDB results for CdZnTe:Ge samples are presented in Fig. 7.10. The experimental CDB curves for the as-grown and Cd or Te-annealed CdZnTe:Ge are plotted in Fig. 7.10a while Fig. 7.10b shows the CDB ratio curves calculated for positrons trapped at V_{Cd} and $V_{Cd}Ge_{Cd}$ defects. The CDB ratio curve for Cd-annealed CdZnTe:Ge sample is again almost flat and close to unity indicating that the momentum distribution in this sample is similar to that in the u-CdTe reference. A slight enhancement in the momentum range $(10 - 30) \times 10^{-3}\ m_0c$ is most probably due to positrons annihilated by electrons belonging to Zn. Annealing in Te vapour modified the momentum distribution of CdZnTe:Ge sample. Shape of the ratio curve for the Te-annealed sample is very similar to the curves calculated for positrons trapped at V_{Cd} and $V_{Cd}Ge_{Cd}$ defects. Hence, in accordance with the results of LT spectroscopy the CDB data in Fig. 7.10 indicate that positrons in CdZnTe:Ge annealed in Te vapour are trapped at defects containing V_{Cd}. Very similar CDB curve was observed also in the as-grown sample. However, CDB spectroscopy does not allow to discern positrons trapped in isolated V_{Cd} from those trapped in $V_{Cd}Ge_{Cd}$ complexes due to very similar CDB ratio curves for both defects, see Fig. 7.10b.

In spite of extensive research, the basic properties of native point defect structure in CdTe/CdZnTe are still far from agreed understanding. Both formation and ionization energies are not settled and analyses based on various defect models or experimental data produce incompatible defect characteristics[22]. Nowadays, it is generally assumed that the difficulties in detecting of native point defects ensue from their reactivity and fast diffusion

at elevated temperature. During cooling to room temperature native defects are supposed to migrate and interact with charged impurities. As a result, various types of associates and precipitates are formed[163,164]. The remaining isolated V_{Cd} mostly annihilate during cooling at surface or dislocations and the final room temperature density of V_{Cd} comes out very low[45]. Evidently, such premise is in pure agreement with evaluated defect structure both in CdTe:Cl and CdZnTe:Ge. Analysis of PAS data suggests that all detected V_{Cd} are incorporated in various complexes stabilizing them in the lattice.

Detailed characterization of defect structure of CdTe:Cl and CdZnTe:Ge samples summarized in Table 7.7 raises a query on the unambiguity of the presented defect model. I believe that the comprehensive exploration of CdTe:Cl and CdZnTe:Ge samples, which were studied both in Cd- and in Te-rich state by multiple techniques, LT, CDB and galvanomagnetic measurements, and characterized by GDMS, allowed me the interpreting of measured data by rather unique way. In view of the fact that the defect densities in Te-rich state significantly exceed the densities of obvious residual extrinsic acceptor, we may conclude that V_{Cd} is the only candidate for the acceptor defect at these conditions.

Similarly, the intentional doping by Cl or Ge donors supplied the only extrinsic elements with the large enough concentration to arrange the detected density of revealed A-centres and complexes. Nevertheless, suggested interpretation of the defect structure of complexes does not represent the only possibility to create neutral or acceptor-type complex in CdTe and CdZnTe. An analogous defect might be created also without participation of extrinsic atoms taking only native point defects into account. That is the complex of Cd vacancy and Te anti-site defect ($V_{Cd}Te_{Cd}$) predicted in Ref. [165]. Such complex was not identified in experiments yet and its electrical properties are not known. The reason, why we favour the structure of complex related to extrinsic Cl or Ge donors rises from the proximity of the evaluated complex densities in Te-annealed samples and respective element concentrations revealed by GDMS. The density of $V_{Cd}Te_{Cd}$ complexes appears significantly below extrinsic-donor-related complexes and does not manifest in presented measurements. This picture is supported also by theoretical calculations in Table 7.3 since the $V_{Cd}Te_{Cd}$ complex is characterized positron lifetime which is slightly lower that the lifetime for isolated V_{Cd}. But such trend was not observed in experimental lifetimes.

7.6 Conclusions

Point defects in CdTe:Cl and CdZnTe:Ge crystals have been characterized by LT and CDB spectroscopies combined with galvanomagnetic measurements. The as-grown CdTe:Cl crystal exhibits larger point defects with open volume comparable with several vacancies. The low temperature LT studies in CdTe:Cl have proved the existence of negatively-charged shallow traps interpreted as Rydberg states associated with Cl-related *A*-centres. These shallow traps are able to confine positrons at low temperatures only when thermal detrapping becomes sufficiently small. The lifetime of positrons localized in the shallow traps is slightly shorter than the CdTe bulk lifetime. The as-grown CdZnTe:Ge crystal contains V_{Cd}^{2-} shallow acceptors forming neutral complexes with Ge_{Cd}^{2+} deep donors. It has been

confirmed that Cd-rich annealing of both CdTe:Cl and CdZnTe:Ge crystals suppresses the concentration of V_{Cd}, which are created again during subsequent Te-rich annealing.

This chapter experimentally proved an existence of $\left(V_{Cd}^{2-} + 2Cl_{Te}^{+}\right)^0$ neutral defects, which is necessary for advance defect model used at chapters 5 and 6. As far as we know , its a first experimental direct observation of this type of defect. However, the key question, what is a secret reservoir of electrical neutral chlorine, which release chlorine during cooling and dynamically contributed Cl_{Te}^{+} to electrical compensation still remain unidentified.

Conclusion

This thesis covers the author's complete scientific path from understanding the theoretical and methodological concepts of crystal physics, ranging from technological steps during sample preparation up to the key focus of the thesis - the experimental investigation of $CdTe$ defect structure with aim to produce high-quality crystals for the gamma-ray detector's applications. We used a broad range of methods which included several types of annealing, room- and high-temperature *in-situ* Hall effects measurement, IR microscopy and positron annihilation spectroscopy.

Different parts of the work were published in three papers and presented at a number of scientific conferences. The author's additional articles are only marginally related to the main thesis topic; therefore, they are mentioned only as non-bold font records in the Author's list of publications.

We introduced an efficient technique for the elimination of both Cd and Te inclusions existing in $CdTe$. We have also introduced a usable but time-consuming interval bisection method for the verification of repeatable reaching the high resistivity $CdTe : Cl$ by the post grown annealing. The correlation between high-resistivity state, chlorine doping, and Te-pressure was proved and deeper analyzed and corresponding observation was presented. The two step Te-annealing profile was successfully used to suppress the influence of the assumed electrically neutral temperature-activated reservoir of donors.

Corresponding high temperature *in-situ* galvanomagnetic measurements led us to the conclusion that a new experimentally unproved electrically neutral defect complex exists in the lattice supplying electrically charged point defects at the dissociation occurring at the temperature or pressure changes. We introduced $\left(V_{Cd}^{2-} + 2Cl_{Te}^{+}\right)^{0}$ as a promising candidate of this neutral defect conforming to all theoretical models.

We studied the chemical diffusion in $CdTe : Cl$, which was measured at temperatures $T = 600$–$800\,°\mathrm{C}$ by means of the relaxation of conductivity of bar-shaped sample after the step-wise change of Cd pressure, and successfully fit with previous theoretical model deduced for undoped and heavily Cl-doped $CdTe$. The chemical diffusion coefficient $D\,(\mathrm{cm^2\,s^{-1}}) = 68\exp(-1.38\ \mathrm{eV/k_BT})$ was determined for CdTe : Cl, $[\mathrm{Cl}] \approx 4.3 \times 10^{16}$ $\mathrm{cm^{-3}}$ samples.

Therefore, based on the sample size and applied temperature, we were able to set the optimal delay of annealing steps to reach high resistivity crystals. Simultaneously, the cooling speed could be individually set up for each sample based on this chemical diffusion coefficient.

We observed a deviation of $\tilde{D}$ in chlorine doped $CdTe : Cl$ from the constant function appearing in undoped $CdTe$ and explained it as a consequence of doping-induced enhancement or suppression of distinct diffusion mechanisms. Obtained diffusion data were completed by an extensive overview of relevant literature and respective activation energies, and pre-exponential terms characterizing the chemical diffusion and self-diffusion in undoped $CdTe$ and $CdTe$ doped by different elements were comprehensively plotted.

The author critically discussed the Meyer-Neldel rule and its factual failures were accen-

tuated in the thesis. I argued that seemingly valid MNR partly expresses deficiencies of experimental approaches and theoretical models used in the evaluation of diffusion coefficients of respective defects. Simultaneously, we have presented the generalized triangle-shaped Meyer-Neldel rule that is in accordance with a theoretical model of chemical diffusion in undoped and Cl-doped $CdTe$. The validity of validity of Δ-MNR directly stems from the defect model used and it does not request any additional premises on enthalpy-entropy compensation.

Point defects in $CdTe : Cl$ and $CdZnTe : Ge$ crystals have been characterized by positron LT and CDB spectroscopies combined with galvanomagnetic measurements. We found out that the as-grown $CdTe : Cl$ crystal exhibits larger point defects with an open volume comparable with several vacancies. The low-temperature LT studies in $CdTe : Cl$ have proved the existence of negatively-charged shallow traps interpreted as Rydberg states associated with Cl-related A-centers. These shallow traps are able to confine positrons at low temperatures only when thermal de-trapping becomes sufficiently small. The lifetime of positrons localized in the shallow traps is slightly shorter than the $CdTe$ bulk lifetime. The as-grown $CdZnTe : Ge$ crystal contains $\mathrm{V}_{\mathrm{Cd}}^{2-}$ shallow acceptors forming neutral complexes with $\mathrm{Ge}_{\mathrm{Cd}}^{2+}$ deep donors. It has been confirmed that Cd-rich annealing of both $CdTe : Cl$ and $CdZnTe : Ge$ crystals suppresses the concentration of V_{Cd}, which are created again during subsequent Te-rich annealing.

We have experimentally proved an existence of assumed $\left(V_{Cd}^{2-} + 2Cl_{Te}^{+}\right)^0$ neutral defects by two independent method - In-Situ galvanomagnetic measurements and Positron annihilation spectroscopy. As far as we know, it is the first experimental direct observation of this type of defect. However, the key question, what a secret reservoir of electrical neutral chlorine is, which releases chlorine during cooling and dynamically affords Cl_{Te}^{+} to the electrical compensation, still remains unanswered.

To conclude, this work attempts to provide a comprehensive understanding of the annealing processes and investigate the effect of annealing conditions on bulk $CdTe$-based crystals' structural and electrical properties. Naturally, the work presented here covers the first phases of our research and opens a number of doors for future investigations, ideas and concepts.

Author's contribution

The author of this thesis prepared samples for all types of measurements, which included the crystal cutting, sample's surface treatment described in detail at Appendix A, characterization of inclusions by IR microscopy, and contact preparation and welding in samples for high-temperature measurements. Author prepared ampoules and optimized the furnace for the annealing. He subsequently performed respective annealing and high-temperature measurements and evaluated respective transport characteristics. The author evaluated electrical conductivity, free carrier concentration and mobility using the home-made software accessible in the Institute of Physics. Simultaneously, he wrote a script for the evaluation of the chemical diffusion coefficient from *In-Situ* galvanomagnetic measurements. He performed extensive search of relevant scientific literature. Author also significantly participated at all discussions defining appropriate theoretical models describing observed effects and performed some numerical calculations. The author is the initiator of the collaboration with the group of Positron annihilation led by Prof. Čížek at the Faculty of Mathematics and Physics. He figured out the design of the experimental study, gathered all data and established the discussion group for its interpretation. This group continues at the investigating of semiconductor materials by means of positron annihilation till now using the approaches developed in this thesis.

Author publications list

1. **Franc, J., Šedivý, L., Belas, E., Bugár, M., Zázvorka, J., Pekárek, J., Uxa, Š., Höschl, P. & Fesh, R. Melt growth and post-grown annealing of semiinsulating (CdZn)Te by vertical gradient freeze method.** ***Crystal Research and Technology*** **48, 214–220. ISSN: 02321300 (2013)**.

   Citations: 9

   IF at the year of publication: 1.331

   Author contribution: Annealing experiments, samples preparation, galvanomagnetic characterization and IR microscopy corresponds approximately to 40% of publication.

2. **Šedivý, L., Čížek, J., Belas, E., Grill, R. & Melikhova, O. Positron annihilation spectroscopy of vacancy-related defects in CdTe:Cl and CdZnTe:Ge at different stoichiometry deviations.** ***Scientific Reports*** **6, 20641. ISSN: 2045-2322 (2016)**.

   Citations: 10

   IF at the year of publication: 4.259

   Author contribution: Main article idea, establishing and managing cooperation, annealing experiments, samples preparation, galvanomagnetic characterization, GDMS spectroscopy handling, corresponds approximately to 60% of publication.

3. **Šedivý, L., Belas, E., Grill, R., Musiienko, A. & Vasylchenko, I. Extension of Meyer-Neldel rule using chemical diffusion experiments in CdTe.** ***Journal of Alloys and Compounds*** **788, 897–904. ISSN: 0925-8388 (2019)**.

   Citations: 4

   IF at the year of publication: 4.650

   Author contribution: Main annealing and *in-situ* experiments, samples preparation, extensive literature study, corresponds approximately to 65% of publication.

4. Belas, E., Uxa, Š., Grill, R., Hlídek, P., Šedivý, L. & Bugár, M. High temperature optical absorption edge of CdTe single crystal. *Journal of Applied Physics* **116,** 103521. ISSN: 0021-8979 (2014)

   Citations: 12

   Author contribution: Some optical measurement, samples optimization of laboratory set-up corresponds to 10% of publication.

5. Zázvorka, J., Franc, J., Moravec, P., Jesenská, E., Šedivý, L., Ulrych, J. & Mašek, K. Contactless resistivity and photoconductivity correlation to surface preparation of CdZnTe. *Applied Surface Science* **315,** 144–148. ISSN: 01694332 (2014)

   Citations: 12

   IF at the year of publication: 2.711

   Author contribution: Sample surface treatment corresponds to 10% of publication.

6. Musiienko, A., Grill, R., Moravec, P., Korcsmáros, G., Rejhon, M., Pekárek, J., Elhadidy, H., Šedivý, L. & Vasylchenko, I. Dual-wavelength photo-Hall effect spectroscopy of deep levels in high resistive CdZnTe with negative differential photoconductivity. *Journal of Applied Physics* **123,** 161502. ISSN: 0021-8979 (2018)

   Citations: 12

   IF at the year of publication: 2.328

   Author contribution: Measurement set-up optimization corresponds to 10% of publication.

7. Musiienko, A., Grill, R., Moravec, P., Fochuk, P., Vasylchenko, I., Elhadidy, H. & Šedivý, L. Photo-Hall-Effect Spectroscopy with Enhanced Illumination in p-Cd1-xMnxTeShowing Negative Differential Photoconductivity. *Physical Review Applied* **10,** 014019. ISSN: 2331-7019 (2018)

   Citations: 6

   IF at the year of publication: 4.532

   Author contribution: Sample preparation corresponds to 10% of publication.

Bibliography

1. Enn Velmre. Thomas Johann Seebeck (1770–1831). *Estonian Journal of Engineering* **13,** 276–282 (2007).
2. Faraday, M. in (ed Richard and John Edward Taylor) 1st ed., 122–124 (London, 1839).
3. Becquerel, A. E. Comptes rendus hebdomadaires des séances de l'Académie des sciences / publiés... par MM. les secrétaires perpétuels. *Comptes Rendus* **9,** 561–567 (1839).
4. Effect of Light on Selenium During the Passage of An Electric Current*. *Nature* **7,** 303–303. ISSN: 0028-0836 (1873).
5. Braun, F. Ueber die Stromleitung durch Schwefelmetalle. *Annalen der Physik und Chemie* **229,** 556–563. ISSN: 00033804 (1875).
6. Morris, P. R. & of Electrical Engineers, I. *A History of the World Semiconductor Industry* ISBN: 9780863412271 (P. Peregrinus, 1990).
7. Perlin, J. *From Space to Earth* ISBN: 978-0674010130 (Harvard University Press, Cambridge, Massachusetts, 2002).
8. Hall, E. H. On a New Action of the Magnet on Electric Currents. *American Journal of Mathematics* **2,** 287–292 (1879).
9. *The Electrician* **39** (James Gray, 1897).
10. Buchwald, J. Z. & Warwick, A. *Histories of the Electron: The Birth of Microphysics* ISBN: 9780262024945 (MIT Press, 2001).
11. Bloch, F. Über die Quantenmechanik der Elektronen in Kristallgittern. *Z Phys Chem (N F)* **52,** 555–600. ISSN: 1434-6001 (1929).
12. Cahn, R. W. *The Coming of Materials Science* ISBN: 9780080529424 (Elsevier Science, 2001).
13. Wilson, A. H. *Semiconductors and Metals: An Introduction to the Electron Theory of Metals* (Cambridge University Press, 1939).
14. Schottky, W. On the Origin of the Super-Heterodyne Method. *Proceedings of the IRE* **14,** 695–698. ISSN: 0096-8390 (1926).
15. Fang, Z., Wang, X. C., Wu, H. C. & Zhao, C. Z. *Achievements and challenges of CdS/CdTe solar cells* 2011.
16. Kranz, L., Buecheler, S. & Tiwari, A. N. Technological status of CdTe photovoltaics. *Solar Energy Materials and Solar Cells* **119,** 278–280. ISSN: 09270248 (2013).

17. Gessert, T. a., Wei, S. H., Ma, J., Albin, D. S., Dhere, R. G., Duenow, J. N., Kuciauskas, D., Kanevce, A., Barnes, T. M., Burst, J. M., Rance, W. L., Reese, M. O. & Moutinho, H. R. Research strategies toward improving thin-film CdTe photovoltaic devices beyond 20% conversion efficiency. *Solar Energy Materials and Solar Cells* **119,** 149–155. ISSN: 09270248 (2013).

18. Szeles, C. CdZnTe and CdTe materials for X-ray and gamma ray radiation detector applications. *physica status solidi (b)* **241,** 783–790. ISSN: 03701972 (2004).

19. Del Sordo, S., Abbene, L., Caroli, E., Mancini, A. M., Zappettini, A. & Ubertini, P. Progress in the Development of CdTe and CdZnTe Semiconductor Radiation Detectors for Astrophysical and Medical Applications. *Sensors* **9,** 3491–3526. ISSN: 1424-8220 (2009).

20. Nishimura, T., Aritome, H., Masuda, K. & Namba, S. Optical Waveguiding and Electrooptic Modulation in Ion-Implanted CdTe. *Japanese Journal of Applied Physics* **15,** 2283–2284. ISSN: 0021-4922 (1976).

21. Sen, S., Liang, C. S., Rhiger, D. R., Stannard, J. E. & Arlinghaus, H. F. Reduction of CdZnTe substrate defects and relation to epitaxial HgCdTe quality. *Journal of Electronic Materials* **25,** 1188–1195. ISSN: 0361-5235 (1996).

22. Schlesinger, T. E., Toney, J. E., Yoon, H., Lee, E. Y., Brunett, B. A., Franks, L. & James, R. B. *Cadmium zinc telluride and its use as a nuclear radiation detector material* 2001.

23. De Nobel, D. *Phase Equilibria and Semiconducting Properties of Cadmium Telluride* (sn, 1958).

24. Zanio, K. & Pollak, F. H. in *Semiconductors and Semimetals* (eds Beer, A. C. & Willardson, R.) 13th ed. 8, 53–54 (Academic Press, New York, 1978). ISBN: 9780127521138.

25. Triboulet, R. & Siffert, P. *CdTe and Related Compounds; Physics, Defects, Hetero- and Nano-structures, Crystal Growth, Surfaces and Applications* 1st ed., 550. ISBN: 9780080914589 (Elsevier Science, 2009).

26. Fiederle, M., Feltgen, T., Meinhardt, J., Rogalla, M. & Benz, K. State of the art of (Cd,Zn)Te as gamma detector. *Journal of Crystal Growth* **197,** 635–640. ISSN: 00220248 (1999).

27. Chadov, S., Qi, X. .-L., Kübler, J., Fecher, G. H., Felser, C. & Zhang, S. .-C. Tunable Multifunctional Topological Insulators in Ternary Heusler Compounds. arXiv: 1003.0193 (2010).

28. Grill, R., Franc, J., Hoschl, P., Turkevych, I., Belas, E., Moravec, P., Fiederle, M. & Benz, K. High-temperature defect structure of Cd- and Te-rich CdTe. *IEEE Transactions on Nuclear Science* **49,** 1270–1274. ISSN: 0018-9499 (2002).

29. Franc, J., Šedivý, L., Belas, E., Bugár, M., Zázvorka, J., Pekárek, J., Uxa, Š., Höschl, P. & Fesh, R. Melt growth and post-grown annealing of semiinsulating (CdZn)Te by vertical gradient freeze method. *Crystal Research and Technology* **48,** 214–220. ISSN: 02321300 (2013).
30. Carvalho, A., Tagantsev, A. K., Öberg, S., Briddon, P. R. & Setter, N. Cation-site intrinsic defects in Zn-doped CdTe. *Physical Review B* **81,** 75215. ISSN: 1098-0121 (2010).
31. Gibbs, J. W., Bumstead, H. A. & Van Name, R. G. *The Scientific Papers of J. Willard Gibbs, Ph.D. Ll.D., Formerly Professor of Mathematical Physics in Yale University: Thermodynamics* ISBN: 0918024773 (Longmans, Green and Company, 1906).
32. Greenberg, J. P–T–X phase equilibrium and vapor pressure scanning of non–stoichiometry in the Cd–Zn–Te system. *Progress in Crystal Growth and Characterization of Materials* **47,** 196–238. ISSN: 09608974 (2003).
33. Haloui, A., Feutelais, Y. & Legendre, B. Experimental study of the ternary system CdTeZn. *Journal of Alloys and Compounds* **260,** 179–192. ISSN: 09258388 (1997).
34. Greenberg, J. *Thermodynamic Basis of Crystal Growth: P-T-X Phase Equilibrium and Non-Stoichiometry* (eds Zunger, A., Hull, R., Osgood, R., Sakaki, H. & Parisi, J.) ISBN: 9783662048764 (Springer Berlin Heidelberg, Heidelberg, 2013).
35. Grill, R. & Zappettini, A. Point defects and diffusion in cadmium telluride. *Progress in Crystal Growth and Characterization of Materials* **48-49,** 209–244. ISSN: 09608974 (2004).
36. Bugár, M. *Dynamics of structural defects in CdTe-based semiconductors* PhD thesis (Charles University, 2011).
37. Belas, E., Bugár, M., Grill, R., Franc, J., Moravec, P., Hlídek, P. & Höschl, P. Reduction of Inclusions in (CdZn)Te and CdTe:In Single Crystals by Post-Growth Annealing. *Journal of Electronic Materials* **37,** 1212–1218. ISSN: 0361-5235 (2008).
38. Uxa, Š. *Transport and optical properties of CdTe/CdZnTe single crystals* PhD thesis (Charles University, 2014).
39. Schreiber, J., Höring, L., Uniewski, H., Hildebrandt, S. & Leipner, H. S. Recognition and Distribution of A(g) and B(g) Dislocations in Indentation Deformation Zones on {111} and {110} Surfaces of CdTe. *physica status solidi (a)* **171,** 89–97. ISSN: 00318965 (1999).
40. Biswas, K. & Du, M.-H. What causes high resistivity in CdTe. *New Journal of Physics* **14,** 63020. ISSN: 1367-2630 (2012).
41. Rudolph, P. Non-stoichiometry related defects at the melt growth of semiconductor compound crystals – a review. *Crystal Research and Technology* **38,** 542–554. ISSN: 02321300 (2003).

42. Kröger, F. *The Chemistry of Imperfect Crystals* 2nd Revised (American Elsevier Publishing, London, 1973).
43. Neumark, G. Defects in wide band gap II-VI crystals. *Materials Science and Engineering: R: Reports* **21,** iii–46. ISSN: 0927796X (1997).
44. Neumark, G. F. Are impurities the cause of selfcompensation in large band gap semiconductors? *Journal of Applied Physics* **51,** 3383–3387. ISSN: 0021-8979 (1980).
45. Grill, R., Franc, J., Hoschl, P., Turkevych, I., Belas, E. & Moravec, P. Semi-insulating Te-saturated CdTe. *IEEE Transactions on Nuclear Science* **52,** 1925–1931. ISSN: 0018-9499 (2005).
46. Grill, R., Franc, J., Höschl, P., Belas, E., Turkevych, I., Turjanska, L. & Moravec, P. Semiinsulating CdTe. *Nuclear Instruments and Methods in Physics Research Section A: Accelerators, Spectrometers, Detectors and Associated Equipment* **487,** 40–46. ISSN: 01689002 (2002).
47. Belas, E., Bugar, M., Grill, R., Franc, J. & Hoschl, P. Preparation of Inclusion and Precipitate Free Semi-Insulating CdTe. *IEEE Transactions on Nuclear Science* **56,** 1758–1762. ISSN: 0018-9499 (2009).
48. Allachen, K., Tapiero, M., Guellil, Z., Zielinger, J. & Launay, J. Photoconductivity studies in vanadium-doped CdTe and Cd1-xZnxTe. *Journal of Crystal Growth* **184-185,** 1142–1146. ISSN: 00220248 (1998).
49. (eds Beer, A., Willardson, R. K. & Weber, E.) *Semiconductors for Room Temperature Nuclear Detector Applications* 1995.
50. Franc, J., Fiederle, M., Babentsov, V., Fauler, A., Benz, K. W. & James, R. Defect structure of Sn-doped CdTe. *Journal of Electronic Materials* **32,** 772–777. ISSN: 0361-5235 (2003).
51. Elhadidy, H. *Development of room temperature CdTe gamma ray detectors for security and medical applications* PhD thesis (Charles University, 2008).
52. Rudolph, P., Engel, A., Schentke, I. & Grochocki, A. Distribution and genesis of inclusions in CdTe and (Cd,Zn)Te single crystals grown by the Bridgman method and by the travelling heater method. *Journal of Crystal Growth* **147,** 297–304. ISSN: 00220248 (1995).
53. Brion, H., Mewes, C., Hahn, I. & Schäufele, U. Infrared contrast of inclusions in CdTe. *Journal of Crystal Growth* **134,** 281–286. ISSN: 00220248 (1993).
54. Wada, M. & Suzuki, J. Characterization of Te Precipitates in CdTe Crystals. *Jpn. J. Appl. Phys.* **27,** L972–L975. ISSN: 0021-4922 (1988).
55. Shen, J., Aidun, D., Regel, L. & Wilcox, W. Etch pits originating from precipitates in CdTe and Cd1-xZnxTe grown by the vertical Bridgman-Stockbarger method. *Journal of Crystal Growth* **132,** 351–356. ISSN: 00220248 (1993).

56. Shen, J., Aidun, D., Regel, L. & Wilcox, W. Characterization of precipitates in CdTe and Cd1-xZnxTe grown by vertical Bridgman-Stockbarger technique. *Journal of Crystal Growth* **132,** 250–260. ISSN: 00220248 (1993).
57. Kim, W., Park, M., Kim, S., Lee, T., Kim, J., Song, W. & Suh, S. Effect of Cd-annealing on the IR transmittance of CdTe wafers grown by the Bridgman method. *Journal of Crystal Growth* **104,** 677–682. ISSN: 00220248 (1990).
58. Sen, S., Rhiger, D. R., Curtis, C. R., Kalisher, M. H., Hettich, H. L. & Currie, M. C. Infrared absorption behavior in CdZnTe substrates. *Journal of Electronic Materials* **30,** 611–618. ISSN: 0381-5235 (2001).
59. Shen, J., Aidun, D., Regel, L. & Wilcox, W. Effect of thermal annealing on the microstructure of CdTe and Cd1-xZnxTe crystals. *Materials Science and Engineering: B* **16,** 182–185. ISSN: 09215107 (1993).
60. Ayoub, M., Hage-Ali, M., Zumbiehl, A., Regal, R., Koebel, J., Rit, C., Fougeres, P. & Siffert, P. Study of the resistivity mapping in CdTe:Cl-correlation with annealing and Te-precipitates. *IEEE Transactions on Nuclear Science* **49,** 1954–1959. ISSN: 0018-9499 (2002).
61. Ayoub, M., Hage-Ali, M., Koebel, J., Zumbiehl, A., Klotz, F., Rit, C., Regal, R., Fougres, P. & Siffert, P. Annealing effects on defect levels of CdTe:Cl materials and the uniformity of the electrical properties. *IEEE Transactions on Nuclear Science* **50,** 229–237. ISSN: 0018-9499 (2003).
62. Vydyanath, H. R. Recipe to minimize Te precipitation in CdTe and (Cd,Zn)Te crystals. *Journal of Vacuum Science & Technology B: Microelectronics and Nanometer Structures* **10,** 1476. ISSN: 0734211X (1992).
63. Vydyanath, H. R., Ellsworth, J. A., Parkinson, J. B., Kennedy, J. J., Dean, B., Johnson, C. J., Neugebauer, G. T., Sepich, J. & Liao, P.-K. Thermomigration of Te precipitates and improvement of (Cd,Zn)Te substrate characteristics for the fabrication of LWIR (Hg, Cd)Te photodiodes. *Journal of Electronic Materials* **22,** 1073–1080. ISSN: 0361-5235 (1993).
64. Lee, T. S., Park, J. W., Jeoung, Y. T., Kim, H. K., Chun, C. H., Kim, J. M., Park, I. H., Chang, J. M., Kim, S. U. & Park, M. J. Thermomigration of tellurium precipitates in CdZnTe crystals grown by vertical bridgman method. *Journal of Electronic Materials* **24,** 1053–1056. ISSN: 0361-5235 (1995).
65. Bugár, M., Belas, E., Procházka, J., Hlídek, P., Grill, R., Franc, J. & Höschl, P. IR transmittance of CdTe after high-temperature annealing. *Nuclear Instruments and Methods in Physics Research Section A: Accelerators, Spectrometers, Detectors and Associated Equipment* **633,** S83–S85. ISSN: 01689002 (2011).

66. Fochuk, P., Grill, R., Kopach, O., Bolotnikov, A. E., Belas, E., Bugar, M., Camarda, G., Chan, W., Cui, Y., Hossain, A., Kim, K. H., Nakonechnyi, I., Panchuk, O., Yang, G. & James, R. B. Elimination of Te Inclusions in Cd_(1-x)Zn_xTe Crystals by Short-term Thermal Annealing. *IEEE Transactions on Nuclear Science* **59,** 256–263. ISSN: 0018-9499 (2012).

67. Belas, E., Grill, R., Franc, J., Moravec, P., Bok, J. & Hoschl, P. Preparation of Semi-Insulating CdTe:In by Post-Grown Annealing After Elimination of Te Inclusions. *IEEE Transactions on Nuclear Science* **54,** 786–791. ISSN: 0018-9499 (2007).

68. Bugar, M., Belas, E., Grill, R., Prochazka, J., Uxa, Š., Hlidek, P., Franc, J., Fesh, R. & Hoschl, P. Inclusions Elimination and Resistivity Restoration of CdTe:Cl Crystals by Two-Step Annealing. *IEEE Transactions on Nuclear Science* **58,** 1942–1948. ISSN: 0018-9499 (2011).

69. Franc, J., Belas, E., Bugár, M., Hlídek, P., Grill, R., Yang, G., Cavallini, A., Fraboni, B., Castaldini, A. & Assali, S. Semi insulating CdTe:Cl after elimination of inclusions and precipitates by post grown annealing. *Journal of Instrumentation* **7,** C11001–C11001. ISSN: 1748-0221 (2012).

70. Höschl, P., Ivanov, Y., Belas, E., Franc, J., Grill, R., Hlídek, P., Moravec, P., Zvára, M., Sitter, H. & Toth, A. Electrical and luminescence properties of (CdZn)Te single crystals prepared by the vertical gradient freezing method. *Journal of Crystal Growth* **184-185,** 1039–1043. ISSN: 00220248 (1998).

71. Schroder, D. K. *Semiconductor Material and Device Characterization* Third Edition. ISBN: 0471749095 (Wiley-Interscience, USA, 2006).

72. Van Der Pauw, L. J. A method of measuring the resistivity and Hall coefficient on lamellae of arbitrary shape. *Philips Technical Review* **20,** 220–224 (1958).

73. Kasap, S. O. (O. & Capper, P. *Springer handbook of electronic and photonic materials* 1st ed. (eds Kasap, S. O. (O. & Capper, P.) 1406. ISBN: 9780387260594 (Springer, New Delhi, India, 2006).

74. Belas, E., Grill, R., Toth, A., Moravec, P., Horodysky, P., Franc, J., Hoschl, P., Wolf, H. & Wichert, T. Electrical and optical properties of in-doped CdTe after Cd-rich annealing. *IEEE Transactions on Nuclear Science* **52,** 1932–1936. ISSN: 0018-9499 (2005).

75. Biswas, K. & Du, M.-H. What causes high resistivity in CdTe. *New Journal of Physics* **14,** 063020. ISSN: 1367-2630 (2012).

76. Ohmori, M., Iwase, Y. & Ohno, R. High quality CdTe and its application to radiation detectors. *Materials Science and Engineering: B* **16,** 283–290. ISSN: 09215107 (1993).

77. Ayoub, M., Hage-Ali, M., Zumbiehl, A., Regal, R., Koebel, J., Rit, C., Fougeres, P. & Siffert, P. Study of the resistivity mapping in CdTe:Cl-correlation with annealing and Te-precipitates. *IEEE Transactions on Nuclear Science* **49,** 1954–1959. ISSN: 0018-9499 (2002).

78. Ayoub, M., Hage-Ali, M., Koebel, J., Zumbiehl, A., Klotz, F., Rit, C., Regal, R., Fougres, P. & Siffert, P. Annealing effects on defect levels of CdTe:Cl materials and the uniformity of the electrical properties. *IEEE Transactions on Nuclear Science* **50,** 229–237. ISSN: 0018-9499 (2003).

79. Bugar, M., Belas, E., Grill, R., Prochazka, J., Uxa, Š., Hlidek, P., Franc, J., Fesh, R. & Hoschl, P. Inclusions Elimination and Resistivity Restoration of CdTe:Cl Crystals by Two-Step Annealing. *IEEE Transactions on Nuclear Science* **58,** 1942–1948. ISSN: 0018-9499 (2011).

80. Grill, R., Franc, J. & Turkevych, I. Semi-insulating CdTe with a minimum deep level doping. *phys. stat. sol. (c)* **494,** 1489–1494 (2005).

81. Zanio, K. Chemical Diffusion in Cadmium Telluride. *Journal of Applied Physics* **41,** 1935–1940. ISSN: 0021-8979 (1970).

82. Grill, R., Turjanska, L., Franc, J., Belas, E., Turkevych, I. & Höschl, P. Chemical Self-Diffusion in CdTe. *physica status solidi (b)* **229,** 161–164. ISSN: 0370-1972 (2002).

83. Rud, Y. V. & Sanin, K. V. Observation of high-temperature relaxation of electrical conductivity in cadmium telluride crystals. *SOVIET Physics Semiconductors-USSR* **6,** 764. ISSN: 0038-5700 (1972).

84. Rud, Y. V. & Sanin, K. V. Electrical conductivity of cadmium telluride in region of melting-point. *SOVIET Physics Semiconductors-USSR* **5,** 1385. ISSN: 0038-5700 (1972).

85. Grill, R., Nahlovskyy, B., Belas, E., Bugár, M., Moravec, P. & Höschl, P. Chemical diffusion in CdTe:Cl. en. *Semiconductor Science and Technology* **25,** 045019. ISSN: 0268-1242 (2010).

86. Grill, R. & Zappettini, A. Point defects and diffusion in cadmium telluride. *Progress in Crystal Growth and Characterization of Materials* **48-49,** 209–244. ISSN: 09608974 (2004).

87. Grill, R., Belas, E., Bugar, M., Hoschl, P., Nahlovskyy, B., Fochuk, P., Panchuk, O., Bolotnikov, A. E. & James, R. B. Multi-Species Diffusion in CdTe. *IEEE Transactions on Nuclear Science* **56,** 1763–1767. ISSN: 0018-9499 (2009).

88. Höschl, P., Grill, R., Franc, J., Moravec, P. & Belas, E. Native defect equilibrium in semi-insulating CdTe(Cl). *Mater. Sci. Eng. B.* **16,** 215–218. ISSN: 09215107 (1993).

89. Shan, Y. Y., Lynn, K. G., Szeles, C., Asoka-Kumar, P., Thio, T., Bennett, J. W., Beling, C. B., Fung, S. & Becla, P. Microscopic Structure of DX Centers in $Cd_{0.8}Zn_{0.2}Te$: Cl. *Phys. Rev. Lett.* **79,** 4473–4476. ISSN: 0031-9007 (1997).

90. Capper, P. *Properties of Narrow Gap Cadmium-based Compounds* 103, 457. ISBN: 9780852968802 (INSPEC, the Institution of Electrical Engineers, 1994).

91. Belova, I. V., Shaw, D. & Murch, G. E. Limits of the ratios of tracer diffusivities for diffusion by vacancy pairs: Application to compound semiconductors. *Journal of Applied Physics* **106,** 113707. ISSN: 0021-8979 (2009).

92. Chern, S. & Kroger, F. The defect structure of CdTe: Self-diffusion data. *Journal of Solid State Chemistry* **14,** 44–51. ISSN: 00224596 (1975).

93. Atkins, P. & de Paula, J. *Elements of Physical Chemistry* Fifth, 600. ISBN: 978–1-–4292–1813–9 (Oxford University Press, Oxford, Great Britain, 2009).

94. Liu, L. & Guo, Q.-X. Isokinetic Relationship, Isoequilibrium Relationship, and Enthalpy-Entropy Compensation. *Chemical Reviews* **101,** 673–696. ISSN: 0009-2665 (2001).

95. Shcherbak, L., Kopach, O., Fochuk, P., Bolotnikov, A. E. & James, R. B. Empirical Correlations Between the Arrhenius' Parameters of Impurities' Diffusion Coefficients in CdTe Crystals. *Journal of Phase Equilibria and Diffusion* **36,** 99–109. ISSN: 1547-7037 (2015).

96. Lambert, F. L. & Leff, H. S. The Correlation of Standard Entropy with Enthalpy Supplied from 0 to 298.15 K. *Journal of Chemical Education* **86,** 94. ISSN: 0021-9584 (2009).

97. Starikov, E. & Nordén, B. Entropy–enthalpy compensation as a fundamental concept and analysis tool for systematical experimental data. *Chemical Physics Letters* **538,** 118–120. ISSN: 00092614 (2012).

98. Starikov, E. Valid entropy–enthalpy compensation: Fine mechanisms at microscopic level. *Chemical Physics Letters* **564,** 88–92. ISSN: 00092614 (2013).

99. Magomedov, M. N. No Title. en. *High Temperature* **40,** 142–144. ISSN: 0018151X (2002).

100. Dyre, J. C. A phenomenological model for the Meyer-Neldel rule. en. *Journal of Physics C: Solid State Physics* **19,** 5655–5664. ISSN: 0022-3719 (1986).

101. Starikov, E. Meyer-Neldel Rule: True History of its Development and its Intimate Connection to Classical Thermodynamics. en. *Journal of Applied Solution Chemistry and Modeling* **3,** 15–31. ISSN: 1929-5030 (2014).

102. Chern, S. & Kröger, F. Chemical self diffusion in CdTe. *Journal of Solid State Chemistry* **14,** 299–306. ISSN: 00224596 (1975).

103. Shaw, D. Diffusion mechanisms in II–VI materials. *Journal of Crystal Growth* **86,** 778–796. ISSN: 00220248 (1988).

104. Kröger, F. The defect structure of CdTe. en. *Revue de Physique Appliquée* **12,** 205–210. ISSN: 0035-1687 (1977).

105. Shaw, D. The diffusivity of the Cd interstitial in CdTe. *Semiconductor Science and Technology* **27,** 035003. ISSN: 0268-1242 (2012).

106. Borsenberger, P. & Stevenson, D. Self-diffusion of cadmium and tellurium in cadmium telluride. *Journal of Physics and Chemistry of Solids* **29,** 1277–1286. ISSN: 00223697 (1968).

107. Borsenberger, P. *Phd Thesis* PhD thesis (Stanford University, 1967).

108. Jones, E. D., Malzbender, J., Mullins, J. B. & Shaw, N. The diffusion of Cl into CdTe. *Journal of Physics: Condensed Matter* **6,** 7499–7504. ISSN: 0953-8984 (1994).

109. Šedivý, L., Belas, E., Grill, R., Musiienko, A. & Vasylchenko, I. Extension of Meyer-Neldel rule using chemical diffusion experiments in CdTe. *Journal of Alloys and Compounds* **788,** 897–904. ISSN: 0925-8388 (2019).

110. Grill, R., Belas, E., Franc, J., Höschl, P. & Moravec, P. Diffusion of charged defects in Tellurium-rich CdTe. *Nuclear Instruments and Methods in Physics Research Section A: Accelerators, Spectrometers, Detectors and Associated Equipment* **591,** 218–220. ISSN: 01689002 (2008).

111. Bell, R. O., Wald, F. V., Canali, C., Nava, F. & Ottaviani, G. Characterization of the Transport Properties of Halogen-Doped CdTe Used for Gamma-Ray Detectors. *IEEE T. Nucl. Sci.* **21,** 331–341. ISSN: 0018-9499 (1974).

112. Robinson, H. G., Berding, M. A., Hamilton, W. J., Kosai, K., DeLyon, T., Johnson, W. B. & Walker, B. J. Enhanced diffusion and interdiffusion in HgCdTe from fermi-level effects. *Journal of Electronic Materials* **29,** 657–663. ISSN: 0361-5235 (2000).

113. Wolf, H., Wagner, F. & Wichert, T. The unusual influence of intrinsic defects on the diffusion of Ag and Cu in CdTe. *Physica B: Condensed Matter* **340-342,** 275–279. ISSN: 09214526 (2003).

114. Jones, E. & Stewart, N. *Unpublished paper* 1987.

115. Jones, E., Stewart, N. & Mullin, J. Studies on the self-diffusion of cadmium in cadmium telluride in the temperature range 350–650°C using anodic oxidation. *Journal of Crystal Growth* **130,** 6–12. ISSN: 00220248 (1993).

116. Ahmed, M., Jones, E. & Stewart, N. Cd self-diffusion in Cu doped CdTe. *Journal of Crystal Growth* **160,** 36–40. ISSN: 00220248 (1996).

117. Fochuk, P., Grill, R. & Panchuk, O. The nature of point defects in CdTe. *Journal of Electronic Materials* **35,** 1354–1359. ISSN: 0361-5235 (2006).

118. Šedivý, L., Čížek, J., Belas, E., Grill, R. & Melikhova, O. Positron annihilation spectroscopy of vacancy-related defects in CdTe:Cl and CdZnTe:Ge at different stoichiometry deviations. *Scientific Reports* **6,** 20641. ISSN: 2045-2322 (2016).

119. Krause-Rehberg, R., Leipner, H., Abgarjan, T. & Polity, A. Review of defect investigations by means of positron annihilation in II-VI compound semiconductors. *Appl. Phys. A Mater. Sci. Process.* **66,** 599–614. ISSN: 0947-8396 (1998).

120. Kauppinen, H., Baroux, L., Saarinen, K., Corbel, C. & Hautojärvi, P. Identification of cadmium vacancy complexes in CdTe(In), CdTe(Cl) and CdTe(I) by positron annihilation with core electrons. en. *J. Phys. Condens. Matter* **9,** 5495–5505. ISSN: 0953-8984 (1997).

121. Keeble, D. J., Major, J. D., Ravelli, L., Egger, W. & Durose, K. Vacancy defects in CdTe thin films. *Phys. Rev. B* **84,** 174122. ISSN: 1098-0121 (2011).

122. Gély-Sykes, C., Corbel, C. & Triboulet, R. Positron trapping in vacancies in indium doped CdTe crystals. *Solid State Commun.* **80,** 79–83. ISSN: 00381098 (1991).

123. Martyniuk, M. & Mascher, P. Investigation of the defect structure in Cd1-xZnxTe by positron lifetime spectroscopy. *Phys. B Condens. Matter* **308-310,** 924–927. ISSN: 09214526 (2001).

124. Corbel, C., Baroux, L., Kiessling, F., Gély-Sykes, C. & Triboulet, R. Positron trapping at native vacancies in CdTe crystals: In doping effect. *Mater. Sci. Eng. B* **16,** 134–138. ISSN: 09215107 (1993).

125. Boerger, D. M. Generalized Hall-effect measurement geometries and limitations of van der Pauw-type Hall-effect measurements. *J. Appl. Phys.* **52,** 269. ISSN: 00218979 (1981).

126. Vlček, M. *Phd Thesis* PhD thesis (Charles University, 2016).

127. Bergersen, B., Pajanne, E., Kubica, P., Stott, M. & Hodges, C. Positron diffusion in metals. *Solid State Communications* **15,** 1377–1380. ISSN: 00381098 (1974).

128. Bečvář, F., Čížek, J., Procházka, I. & Janotová, J. The asset of ultra-fast digitizers for positron-lifetime spectroscopy. *Nucl. Instrum. Meth. A* **539,** 372–385. ISSN: 01689002 (2005).

129. Ore, A. & Powell, J. L. Three-photon annihilation of an electron-positron pair. *Physical Review* **75,** 1696–1699. ISSN: 0031899X (1949).

130. Asoka-Kumar, P., Alatalo, M., Ghosh, V., Kruseman, A., Nielsen, B. & Lynn, K. Increased Elemental Specificity of Positron Annihilation Spectra. *Phys. Rev. Lett.* **77,** 2097–2100. ISSN: 0031-9007 (1996).

131. Čížek, J., Vlček, M. & Procházka, I. Digital spectrometer for coincidence measurement of Doppler broadening of positron annihilation radiation. *Nucl. Instrum. Meth. A* **623,** 982–994. ISSN: 01689002 (2010).

132. Krause-Rehberg, R. & Leipner, H. S. *Positron Annihilation in Semiconductors* (Springer-Verlag, Berlin, 1999).

133. Van Veen, A., Schut, H., Clement, M., de Nijs, J., Kruseman, A. & IJpma, M. VEPFIT applied to depth profiling problems. *Appl. Surf. Sci.* **85,** 216–224. ISSN: 01694332 (1995).

134. Puska, M. J. & Nieminen, R. M. Theory of positrons in solids and on solid surfaces. *Rev. Mod. Phys.* **66,** 841–897. ISSN: 0034-6861 (1994).

135. Boroński, E. & Nieminen, R. Electron-positron density-functional theory. *Phys. Rev. B* **34,** 3820–3831. ISSN: 0163-1829 (1986).

136. Puska, M., Mäkinen, S., Manninen, M. & Nieminen, R. Screening of positrons in semiconductors and insulators. *Phys. Rev. B* **39,** 7666–7679. ISSN: 0163-1829 (1989).

137. Perkowitz, S. & Thorland, R. Far-infrared study of free carriers and the plasmon-phonon interaction in CdTe. *Phys. Rev. B* **9,** 545–550. ISSN: 0556-2805 (1974).

138. Barbiellini, B., Puska, M., Korhonen, T., Harju, A., Torsti, T. & Nieminen, R. Calculation of positron states and annihilation in solids: A density-gradient-correction scheme. *Phys. Rev. B* **53,** 16201–16213. ISSN: 0163-1829 (1996).

139. Desclaux, J. A multiconfiguration relativistic DIRAC-FOCK program. *Comput.-Phys. Commun.* **9,** 31–45. ISSN: 00104655 (1975).

140. Puska, M. J. & Nieminen, R. M. Defect spectroscopy with positrons: a general calculational method. *J. Phys. F Met. Phys.* **13,** 333–346. ISSN: 0305-4608 (1983).

141. Puska, M., Seitsonen, A. & Nieminen, R. Electron-positron Car-Parrinello methods: Self-consistent treatment of charge densities and ionic relaxations. *Phys. Rev. B* **52,** 10947–10961. ISSN: 0163-1829 (1995).

142. Campillo Robles, J. M., Ogando, E. & Plazaola, F. Positron lifetime calculation for the elements of the periodic table. *J. Phys. Condens. Matter* **19,** 176222. ISSN: 0953-8984 (2007).

143. Kresse, G. & Hafner, J. Ab initio molecular dynamics for liquid metals. *Phys. Rev. B* **47,** 558–561. ISSN: 0163-1829 (1993).

144. Kresse, G. Efficient iterative schemes for ab initio total-energy calculations using a plane-wave basis set. *Phys. Rev. B* **54,** 11169–11186. ISSN: 0163-1829 (1996).

145. Kresse, G. From ultrasoft pseudopotentials to the projector augmented-wave method. *Phys. Rev. B* **59,** 1758–1775. ISSN: 1098-0121 (1999).

146. Monkhorst, H. J. & Pack, J. D. Special points for Brillouin-zone integrations. *Phys. Rev. B* **13,** 5188–5192. ISSN: 0556-2805 (1976).

147. Alatalo, M., Barbiellini, B., Hakala, M., Kauppinen, H., Korhonen, T., Puska, M., Saarinen, K., Hautojärvi, P. & Nieminen, R. Theoretical and experimental study of positron annihilation with core electrons in solids. *Phys. Rev. B* **54,** 2397–2409. ISSN: 0163-1829 (1996).

148. Kuriplach, J., Morales, A., Dauwe, C., Segers, D. & Šob, M. Vacancies and vacancy-oxygen complexes in silicon: Positron annihilation with core electrons. *Phys. Rev. B* **58,** 10475–10483. ISSN: 0163-1829 (1998).

149. Belas, E., Franc, J., Grill, R., Toth, A. L., Horodysky, P., Moravec, P. & Höschl, P. Regular and anomalous-type conversion of p-CdTe during Cd-rich annealing. *J. Electron. Mater.* **34,** 957–962. ISSN: 0361-5235 (2005).

150. Plazaola, F., Seitsonen, A. P. & Puska, M. J. Positron annihilation in II-VI compound semiconductors: theory. en. *J. Phys. Condens. Matter* **6,** 8809–8827. ISSN: 0953-8984 (1994).

151. Gély, C., Corbel, C. & Triboulet, C. Positron lifetime measurements in a II-VI-compound - Indium doped CdTe. *Acad. Sci. Paris* **309,** 179–182 (1989).

152. Dannefaer, S. A systematic study of positron lifetimes in semiconductors. en. *J. Phys. C Solid State Phys.* **15,** 599–605. ISSN: 0022-3719 (1982).

153. Korhonen, T., Puska, M. & Nieminen, R. First-principles calculation of positron annihilation characteristics at metal vacancies. *Phys. Rev. B* **54,** 15016–15024. ISSN: 0163-1829 (1996).

154. Choi, S. S. & Lucovsky, G. Native oxide formation on CdTe. *J. Vac. Sci. Technol. B* **6,** 1198 (1988).

155. Badano, G., Million, A., Canava, B., Tran-Van, P. & Etcheberry, A. Fast Detection of Precipitates and Oxides on CdZnTe Surfaces by Spectroscopic Ellipsometry. *J. Electron. Mater.* **36,** 1077–1084. ISSN: 0361-5235 (2007).

156. Neretina, S., Grebennikov, D., Hughes, R., Weber, M., Lynn, K., Simpson, P., Preston, J. & Mascher, P. Defect characterization of CdTe thin films using a slow positron beam. *Phys. Stat. Sol. c* **4,** 3659 (2007).

157. Manninen, M. & Nieminen, R. M. Positron detrapping from defects: A thermodynamic approach. *Appl. Phys. A Mater. Sci. Process.* **26,** 93–100. ISSN: 0721-7250 (1981).

158. Puska, M., Corbel, C. & Nieminen, R. Positron trapping in semiconductors. *Phys. Rev. B* **41,** 9980–9993. ISSN: 0163-1829 (1990).

159. Corbel, C., Pierre, F., Saarinen, K., Hautojärvi, P. & Moser, P. Gallium vacancies and gallium antisites as acceptors in electron-irradiated semi-insulating GaAs. *Phys. Rev. B* **45,** 3386–3399. ISSN: 0163-1829 (1992).

160. Hautojärvi, P. & Corbel, C. *Positron spectroscopy of defects in metals and semiconductors* in *Positron spectroscopy of solids* (eds Dupasqier, A. & Mills, A. P.) **125** (IOS Press, Amsterdam, 1995), 491–532.

161. Elsayed, M., Krause-Rehberg, R., Anwand, W., Butterling, M. & Korff, B. Identification of defect properties by positron annihilation in Te-doped GaAs after Cu in-diffusion. *Phys. Rev. B* **84,** 195208 (2011).

162. Veen, A. v., Schut, H., Vries, J. d., Hakvoort, R. A. & Ijpma, M. R. *Analysis of positron profiling data by means of "VEPFIT"* in *AIP Conference Proceedings No. 218* (eds Schultz, P., Massoumi, G. & Simpson, P.) (AIP, New York, 1990), 83.

163. Marfaing, Y. Self-compensation in II—VI compounds. *Prog. Cryst. Growth Charact. Mater.* **4,** 317–343. ISSN: 0146-3535 (1981).

164. Marfaing, Y. in *CdTe and Related Compounds; Physics, Defects, Hetero- and Nanostructures, Crystal Growth, Surfaces and Applications* (eds Siffert, R. & Triboulet, P.) First edition, 363–388 (Elsevier, Amsterdam, 2010). ISBN: 978-0-08-046409-1.

165. Berding, M. A. Annealing conditions for intrinsic CdTe. *Appl. Phys. Lett.* **74,** 552. ISSN: 00036951 (1999).

166. Belas, E., Uxa, Š., Grill, R., Hlídek, P., Šedivý, L. & Bugár, M. High temperature optical absorption edge of CdTe single crystal. *Journal of Applied Physics* **116,** 103521. ISSN: 0021-8979 (2014).

167. Zázvorka, J., Franc, J., Moravec, P., Jesenská, E., Šedivý, L., Ulrych, J. & Mašek, K. Contactless resistivity and photoconductivity correlation to surface preparation of CdZnTe. *Applied Surface Science* **315,** 144–148. ISSN: 01694332 (2014).

168. Musiienko, A., Grill, R., Moravec, P., Korcsmáros, G., Rejhon, M., Pekárek, J., Elhadidy, H., Šedivý, L. & Vasylchenko, I. Dual-wavelength photo-Hall effect spectroscopy of deep levels in high resistive CdZnTe with negative differential photoconductivity. *Journal of Applied Physics* **123,** 161502. ISSN: 0021-8979 (2018).

169. Musiienko, A., Grill, R., Moravec, P., Fochuk, P., Vasylchenko, I., Elhadidy, H. & Šedivý, L. Photo-Hall-Effect Spectroscopy with Enhanced Illumination in p-Cd1-xMnxTeShowing Negative Differential Photoconductivity. *Physical Review Applied* **10,** 014019. ISSN: 2331-7019 (2018).

List of Figures

1.1 Zinc-blende crystal structure 7
1.2 band-gap structure of CdTe 8

2.1 3-dimensional $P - T - x$ phase diagram (solid and liquid lines) for CdTe. Value $x = 0.5$ corresponds to CdTe containing exactly 50% Cd atoms and 50% Te atoms. VLS curve corresponds to vapour-liquid-solid CdTe equilibrium for pure Cd. SLV correspond to solid CdTe-liquid-vapour equilibrium of pure Te. $S{=}V$ curve is called sublimation line and represents an equilibrium between solid CdTe and vapour pressure. 10
2.2 $T - x\, diagram$ 11
2.3 $P - T\, diagram$ 11
2.4 Detailed view on the stability region of CdTe defined by the solid lines[35]. . 13
2.5 Visualization of dislocations 14
2.6 Energy levels in CdTe. 15
2.7 Illustration of several points defects at CdTe and its complexes 20

3.1 Scheme of annealing in a two-zone furnace. T_S, T_P correspond to sample and metal temperature, respectively. 23
3.2 Scheme of Hall bar coated at classical 6 wires configuration. Yellow spots are Au contacted places, l, d and w correspond to sample dimension and B represents the oriented intensity of the magnetic field. 24
3.3 Coeficients R_1, R_2 – Van der Pauw 25
3.4 Coeficients U^0, U^H – Van der Pauw 26
3.5 Experimental setup – Van der Pauw configuration 27
3.6 Ilustration of Cd-annealing profile. 29
3.7 Cd inclusions at **S57** $CdTe : Cl$ after annealing at Cd overpressure followed by annealing at Te overpressure. 30
3.8 Te inclusions at **S56** after annealing at Cd overpressure. 31

4.1 Ilustration of Te-annealing two steps profile. 34
4.2 Dependence of the sample resistivity on Te-pressure of the second step during the sub-sequential Te-annealing. 38

5.1 Experimental setup – High temperature Hall configuration 41
5.2 Infrared microscopy detail image of one tungsten wire welded into the sample. The area destroyed by welding is opaque for infrared light. 42
5.3 Typical conductivity profile after step-like P_{Cd} changes 43

5.4 Electrical conductivity dependency on Cd pressure measured at 600 °C, 700 °C and 800 °C. The full bullets represent experimental data, together with double dot-dashed lines, which correspond to theoretical model for undoped CdTe presented by Grill[86]. The dotted, dashed and dash-and-dot lines are theoretical data for CdTe:Cl calculated based on Grill[85] extended by $\left(V_{Cd}^{2-} + 2Cl_{Te}^{+}\right)^{0}$ for 2×10^{16}, 4×10^{16} and 1×10^{17} cm^{-3} chlorine doping, respectively. 45

5.5 Free carriers concentration dependency on Cd pressure measured at 600 °C, 700 °C and 800 °C. The full bullets represent experimental data, corrected by $k = 1.71$ factor, the empty dots represent experimental data corrected individually by $k = 1.42$, $k = 1.48$, $k = 1.60$ for 600 °C, 700 °C and 800 °C, respectively. The red lines represent the linear fits of measured at 600 °C, 700 °C and 800 °C and its slope correspond to pressure dependency of $\sim P_{Cd}^{\frac{1}{6}}$, $\sim P_{Cd}^{\frac{1}{5}}$, $\sim P_{Cd}^{\frac{1}{4}}$, respectively. Double dot-dashed lines correspond to theoretical model for undoped CdTe presented by Grill[86]. The dotted, dashed and dash-and-dot lines are theoretical data for CdTe:Cl calculated based on Grill[85] extended by $\left(V_{Cd}^{2-} + 2Cl_{Te}^{+}\right)^{0}$ for 2×10^{16}, 4×10^{16} and 1×10^{17} cm^{-3} chlorine doping, respectively. 46

5.6 Free carriers mobility dependency on Cd pressure measured at 600 °C, 700 °C and 800 °C. The full bullets represent experimental data, corrected by $k = 1.71$ factor, the empty dots represent experimental data corrected individually by $k = 1.42$, $k = 1.48$, $k = 1.60$ for 600 °C, 700 °C and 800 °C, respectively, together with double dot-dashed lines, which correspond to theoretical model for undoped CdTe presented by Grill[86]. The dotted, dashed and dash-and-dot lines are theoretical data for CdTe:Cl calculated based on Grill[85] extended by $\left(V_{Cd}^{2-} + 2Cl_{Te}^{+}\right)^{0}$ for 2×10^{16}, 4×10^{16} and 1×10^{17} cm^{-3} chlorine doping, respectively. 47

6.1 Typical time relaxation of the electrical conductivity at 700℃ (black points) after Cd overpressure step from 400℃ to 450℃, full line (green online), which corresponds to $\Delta\ P_{\mathrm{Cd}}\ =\ 4.18 \times 10^{-3}$ atm[67]. Dashed line (red online) represents linear fit according to equation (6.8). 52

6.2 Pressure dependence of chemical diffusion coefficient at 600℃, 700℃ and 800℃, respectively (violet, beige and blue online). Top shaped triangles indicate step from lower Cd pressure to higher one, bottom shaped triangles are used for a step from higher Cd pressure to lower one. The full circles are experimental data for undoped CdTe obtained by Zanio[81]. The double dot-dashed lines are theoretical data for undoped CdTe, which were calculated based on $\tilde{D}$ given by Grill[82]. The dotted, dashed and dash-and-dot lines are theoretical data for CdTe : Cl calculated according to [85] for 2×10^{16}, 4×10^{16} and 1×10^{17} cm^2 chlorine doping, respectively. 54

6.3 The experimental mean values of chemical diffusion coefficient at 600°C, 700°C and 800°C, respectively. Full line represents linear fit. 55
6.4 Calculated pressure dependence of chemical diffusion coefficient $\tilde{D}$ for different Cl doping at 600°C. First upper line represents undoped CdTe and then the chlorine concentration increases in the arrow direction with non-linear steps (1, 2 and 4×10^{15}–10^{19} cm^2). 57
6.5 Calculated pressure dependence of chemical diffusion coefficient $\tilde{D}$ for different Cl doping at 700°C. First upper line represents undoped CdTe and then the chlorine concentration increases in the arrow direction with non-linear steps (1, 2 and 4×10^{15}–10^{19} cm^2). 58
6.6 The plot of the pre-exponential factor D_0 as a function of the activation energy E_A collected from accessible chemical diffusion and self-diffusion data are summarized in Tables 6.1, 6.2 and 6.3. Full line represents the fit of chemical diffusion and single point diffusion data, dashed line is the fit of self-diffusion data. The region delimited by dash-and-dot lines represents generalized triangular MNR discussed in the text. 59
6.7 Detail of Meyer-Neldel rule calculation for different Cl-dopping of CdTe : Cl. The region delimited by dash-and-dot lines represents generalized triangular MNR discussed in the text. 63

7.1 Positron lifetime spectroscopy 68
7.2 Positron annihilation scheme 69
7.3 Positron doppler broadering spectroscopy 70
7.4 Positron density in the (001) plane calculated using the ATSUP-GGA approach: (a) perfect CdTe crystal, (b) CdTe crystal containing V_{Cd} in 1,1,0 position, (c) CdTe crystal containing A_C defect consisting of V_{Cd} and Cl_{Te} located in 1,1,0 and 0.25,1.75,0.25 position, respectively. The co-ordinates are expressed in the units of the CdTe lattice constant a. Positron density is given in the atomic units. 79
7.5 Temperature dependence of the mean positron lifetime for CdTe:Cl and CdZnTe:Ge. The lines represent the fit using 3-STM. 80
7.6 The dependence of the S parameter on the energy E of incident positrons for undoped CdTe (full symbols) and CdTe:Cl sample in the as-grown state (open symbols) . Solid lines show model curves calculated by VEPFIT. . . 82
7.7 3-STM positron trapping model 83
7.8 The positron annihilation momentum density $P(p_z)$ measured by CDB in the undoped CdTe sample and calculated for a perfect CdTe crystal using the ATSUP-GGA approach. 91

7.9 The CDB ratio curves (related to defect-free u-CdTe): (a) experimental data for CdTe:Cl in the as-grown state and after annealing in Cd and Te vapour; (b) calculated ratio curves for V_{Cd}, A_C and $V_{Cd}2Cl_{Te}$ defects. The calculated curves are plotted by dashed lines in the low momentum range ($p_z < 15 \times 10^{-3} m_0 c$) where the accuracy of the momentum distribution calculated by ASTUP is poor. 92
7.10 The CDB ratio curves (related to defect-free u-CdTe): (a) experimental data for CdZnTe:Ge in the as-grown state and after annealing in Cd and Te vapour; (b) calculated ratio curves for V_{Cd} and $V_{Cd}Ge_{Cd}$ defects. The calculated curves are plotted by dashed lines in the low momentum range ($p_z < 15 \times 10^{-3}\ m_0 c$) where the accuracy of the momentum distribution calculated by ASTUP is poor. 93

List of Tables

1.1 Physical parameters CdTe 7

3.1 Annealing of $CdTe : Cl$ ($S56$ and $S57$) 28

4.1 Annealing of $CdTe : Cl$ ($S57$) 36
4.2 Annealing of $CdTe : Cl$ ($S56$) 37

5.1 Correction of welded wires 44

6.1 Chemical diffusion coefficient, $\tilde{D}$. 60
6.2 Self diffusion coefficient, D^*. 60
6.3 Diffusion coefficients of individual defects D_i 61

7.1 The concentrations of elements exceeding 10^{15}cm^{-3} for u-CdTe, CdTe:Cl and CdZnTe:Ge established by GDMS in units 10^{15}cm^{-3}. A 30% error of GDMS analysis was declared. 71
7.2 Summary of galvanomagnetic measurements: resistivity of samples, type of conductivity and concentration of free carriers. 74
7.3 Theoretical positron lifetimes for a perfect CdTe crystal and various defects calculated various approaches. Theoretical lifetimes available in literature are shown in the table as well. 75
7.4 Experimental positron lifetimes for a perfect CdTe crystal and selected defects reported in literature. The τ_D/τ_B ratio is shown in the table for positrons trapped at defects. Note that in the ratios the lifetime of trapped positrons was always related to the bulk lifetime measured on the same setup, i.e. τ_D values were divided by τ_B ones published by the same authors. The uncertainties (one standard deviations) are given in parentheses in the units of the last significant digit. 76
7.5 Theoretical τ_D/τ_B ratios for positrons trapped at various defects in CdTe calculated by various approaches. Theoretical τ_D/τ_B ratios available in literature are shown in the table as well. 77
7.6 Results of LT studies: lifetime τ_i and the relative intensity I_i of the exponential components resolved in the LT spectra evaluated at 295 K and 123 K. The uncertainties (one standard deviations) are given in parentheses in the units of the last significant digit. 86
7.7 The concentration of defects calculated from the LT data. The neutral defects at CdTe:Cl and at CdZnTe:Ge, negatively-charged A-centres and shallow Rydberg states associated with negatively-charged A-centres are symbolized by $V_{Cd}2Cl_{Te}$, $V_{Cd}Ge_{Cd}$, A_C, A_C^R, respectively. 90

Appendices

A. Laboratory cook book

This chapter contains laboratory recipes for sample and laboratory equipment preparation. Individual recipes are sorted randomly, independently and usually without any citation to the other authors. It represents only the laboratory practices, which was used when this thesis was under preparation.

A.1 Ampoule preparation

Quartz ampoule fabricated by HERAEUS can be shaped by diamonds knives or using $H_2 + O_2$ pilot flame. The head of pilot has to be from quartz glass to prevent any particles incorporation from pilot head (usually cooper) to shaped glass.

After quartz shaping, its surface has to be cleaned:

1. Surface etching by concentrate **Chromosulfuric acid** for approximately **8 hours**. This is necessary only if precise ampoule **dimensions need to be guaranteed**. Otherwise this step could be skipped and consequently duration of following step has to expanded.

2. Quartz ampoule was etched by **40%** HF solution for approximately **15 minutes** in case of not skipping the previous step. Otherwise it needs to be etched for approximately **1 hour**.

3. Repeatable cleaning using distilled water (3 times or more).

4. Drying in a dryer with low dustiness.

A.2 $CdTe$ sample preparation

A.2.1 Cutting

Wafers cutting

Plan-parallel wafers were sliced perpendicularly to the growth direction from grown ingots by a diamond wire saw Well Diamond Wire Saws Inc. (model 6234) with wire diameter 0.3 mm (cooled by water). The thickness of wafers was usually in the range of 2-3 mm.

Samples cutting

Monocrystalline samples were cut from wafers by a wire saw South Bay Technology Inc. (model 850) using stainless steel wire with diameter of 0.1 mm (with abrasive boroncarbide-glycerine solution).

A.2.2 Polishing

Wafers polishing

Wafers were polished by boron carbide abrasive B_4C **F400** (grit size $8 - 32\,\mu\text{m}$) to reveal the structure of grains on the wafer surface.

Sample polishing

Sample was slowly polished by boron carbide abrasive B_4C **F1200** (grit size $1 - 7\,\mu\text{m}$) to minimalize surface damages. The depth of surface damages corresponds to three times of abrasive grit size.

A.2.3 Chemo-mechanical polishing

For production of high quality surface for **infra-red microscopy**, the chemo-mechanical polishing by **3% bromine-ethyleneglycol** solution on the new **silk** cloth needs to be used. Process was performed for 60 seconds each side. However, it produces low quality surface from **electrical** point of view, resulting in high surface current production. In this case, the **1% bromine-ethyleneglycol** for **3 minutes** from each side should be performed to decrease surface current.

A.2.4 Etching

Samples etching in **3% bromine-methanol** solution for **1 minute** to obtain mirror-like sample surfaces for **infra red microscopy**. The **1% bromine-methanol** solution for **3 minutes** should be performed for any **other usage**.

A.2.5 Cleaning

After etching, samples has to be cleaned at **least 3 times** at destil water. Following with **acetone** and **isoprophanol** bath and carefully dried by clean air.

A.3 Contacts preparation

Ohmic contacts are necessary for precious electric measurement. The sample surface, except contacts, has to be protected by photoresist covering, then the contacts can be deposited by Chemical solution deposition or Physical vapour deposition. The detailed description of both methods is described below.

A.3.1 Chemical solution deposition

Chemical solution deposition of Au contacts is performed in following steps.

1. Sample was placed to 10% $AuCl$ solution for **1 minute**.
2. Solution was **3 times** cleaned at **destil water**.
3. The **acetone** is used for photoresist ablation.
4. The sample was placed to **acetone** and **isoprophanol** bath and carefully dried by clean air.

A.3.2 Physical vapour deposition

Several elements (Au, Ag, In, Cd, Cu) can be vaporized to sample surface. Physical vapour deposition was provided in following steps:

1. Sample was placed to vaporization chamber and the contacted surface was turned opposite to metal source and its cover by shielding.
2. Vaporization chamber was evaporated by rotary oil pump and consequently by oil molecular pump.
3. Metal source is heated to low temperature using low electric current, which yielded to de-oxidation of metal surface.
4. Sample shielding was removed and the currents were used for Au, Ag, In, Cd, Cu, respectively.
5. The **acetone** is used for photoresist ablation.
6. The sample was placed to **acetone** and **isoprophanol** bath and carefully dried by clean air.

A.4 Coating

The Ag wires were soldered to Au contact by In. Or they were slicked by colloid Ag or C. However, it was investigated, that colloid Ag could diffuse to the sample even at room temperature. The colloid C is stable enough from diffusion point of view, however its mechanical stability is poor during temperature changing due to inhomogeneity of its draying. Yield, the In coating was usually used in case of $CdTe$.

A.5 Contacts welding

The tungsten wires were welded directly to the sample in following steps.

1. The tungsten wire is shaped, connected to the capacitate decades as one electrode and placed to sample surface.
2. Second electrode, with floating Ag is approached to the tungsten wire.
3. Resulted spark weld the tungsten wire to sample.